UC Berkeley
UC Berkeley Electronic Theses and Dissertations

Title
Light-matter Interaction in Deep Sub-wavelength Nano-photonic Structures

Permalink
https://escholarship.org/uc/item/0qp0b1tg

Author
Pholchai, Nitipat

Publication Date
2012

Peer reviewed|Thesis/dissertation

eScholarship.org Powered by the California Digital Library
University of California

Light-matter Interaction in Deep Sub-wavelength Nano-photonic Structures

by

Nitipat Pholchai

A dissertation submitted in partial satisfaction of the
requirements for the degree of
Doctor of Philosophy
in
Applied Science and Technology
and the Designated Emphasis
in
Nanoscale Science and Engineering
in the
Graduate Division
of the
University of California, Berkeley

Committee in charge:

Professor Xiang Zhang, Chair
Professor Ming Wu
Professor Hartmut Haeffner

Fall, 2012

Light-matter Interaction in Deep Sub-wavelength Nano-photonic Structures

© Copyright 2012

by

Nitipat Pholchai

Abstract

Light-matter Interaction in Deep Sub-wavelength Nano-photonic Structures

by

Nitipat Pholchai

Doctor of Philosophy in Applied Science and Technology

and the Designated Emphasis in Nanoscale Science and Engineering

University of California, Berkeley

Professor Xiang Zhang, Chair

This dissertation focuses on the use of deep sub-wavelength(sub-λ) nano-photonic structures to enhance radiation of optical emitters. The deep sub-wavelength designs are based on high permittivity contrast of materials involving either purely dielectric interfaces or metal. The optical properties of metal at infrared and optical frequencies enable optical structures that can confine light to dimension smaller than the wavelength. The building blocks of these nano-photonic system are non-resonant, broadband waveguides with dramatic field confinement in the nano-scale low permittivity region. Strong interaction and enhanced radiation leads to efficient coupling into the primary optical mode of the structures which improves fluorescence brightness, saturation, speed, emission efficiency, single photon fidelity at a single emitter-single photon level and holds promise for solid-state lighting, molecular sensing, and quantum information processing application.

The first part of the dissertation explores deep sub-wavelength waveguiding structures as non-resonant optical component that enhances radiation and collects emitted photon with high fidelity. The last part explores the design of small resonator that is constructed from a subwavelength waveguide for use as addressing optical emitters. The benefits of non-resonant design are highlighted throughout.

To my parents,

Chaiya and Neelawan,

Table of Contents

Abstract..... 1
List of Figures..... iv
List of Tables..... vi
Acknowledgement..... vii

1. Introduction..... 1

2. Theoretical Background..... 3
   2.1. Broadband Purcell enhancement of spontaneous emission..... 4
   2.2. Analytic theory of spontaneous emission in a 2D slab geometry..... 9
   2.3. Hybrid plasmon waveguide, dielectric slot waveguide, and slot-PEC (dielectric half-slot) waveguide..... 13
   2.4. Purcell effect simulation using finite element method..... 16
   2.5. Summary..... 19

3. Hybrid Plasmon Waveguide: an experimental probe of deep sub-wavelength optical interaction by molecular fluorescence..... 21
   3.1. Hybrid Plasmon (HPP) waveguide..... 22
   3.2. Experimental setup..... 22
   3.3. Scaling of deep sub-wavelength mode and Purcell enhancement..... 25
   3.4. Extracting different contributions to decay and the effect of dipole orientations.....26
   3.5. Photon flux enhancement..... 29
   3.6. Summary and Outlook.....32

4. Squeezed Photonic Waveguide: single emitter in a deep sub-wavelength all-dielectric waveguide..... 33
   4.1. Design of deep sub-wavelength all-dielectric waveguide: from all-dielectric coupled-nanowire waveguide to squeezed photonic waveguide..... 33
   4.2. Experimental procedure..... 37
   4.3. Purcell-enhanced optical interaction in the coupled QD-waveguide system..... 38
   4.4. Study of single emitter dynamics..... 40
   4.5. Correspondence with theory of Purcell enhancement..... 43

4.6. Fluorescence intermittence and output photon flux in the coupled system……. 45
4.7. Measurement of propagation loss in squeezed photonic waveguide……... 47
4.8. Estimation of emission coupling factor β…… 48
4.9. Summary and Outlook…… 50

5. Hybrid Plasmon Crossbar Cavity: scaling of deep sub-wavelength dipole resonator…….. 52
5.1. Scattering theory of small metal particle……..53
5.2. Hybrid plasmon (HPP) deep sub-wavelength resonators…….. 57
5.3. Fundamental dipole modes of sub-λ resonators……... 59
5.4. Scattering spectra and scaling of sub-λ dipole resonators…… 60
5.5. Ultra-small mode volume of sub-λ resonators……. 63
5.6. Quality factor and radiation behavior of sub-λ resonators……... 65
5.7. Large Purcell effect in the deep sub-λ resonators…… 66
5.8. Summary and Outlook……. 69

6. Conclusions and Future Prospects…… 70

Bibliography……. 72

A. General recursive formula for the reflectivity of a stacked multilayer by transmission line method…… 78

B. Preparation of Silicon nanowires…….. 80

List of Figures

2.1. Waveguide dispersion relation for a single surface SPP and a metal-dielectric-metal (MDM) 2D waveguide …… 7

2.2. Several contributions of dissipation revealed by angular spectrum density of the decay rate..... 11

2.3. Broadband, non-resonant Purcell effect……..... 12

2.4. Hybrid plasmon polariton (HPP) modes for varying gap size and Si slab thickness…….. 14

2.5. Different modal contributions to the Purcell factor of HPP slab waveguide, including metal quenching (LSW)…… 15

2.6. Comparing related sub-λ 2D waveguide structures…… 16

2.7. Validity of finite-element method simulation……. 18

2.8. An example of simulated radiated field of a vertical electric dipole emitting from midgap of a one-dimensional HPP waveguide…… 19

3.1. Hybrid Plasmon (HPP) waveguide design..... 22

3.2. Experimental setup for molecular emission into HPP waveguide..... 24

3.3. HPP waveguide and control samples with corresponding photoluminescence (PL) decay histograms..... 25

3.4. Calculation of Purcell effect inside the HPP waveguide..... 26

3.5. Measurements of different contributions to spontaneous decay …… 28

3.6. Selective removal of dye molecules not coupled to the HPP waveguide mode……. 28

3.7. Mode coupling factor…….. 29

3.8. Fluorescence intensity enhancement..... 31

4.1. Comparing all-dielectric sub-λ slot waveguide designs for Purcell enhancement……. 34

4.2. Experimental system……... 36

4.3. Images of experimental procedure…….. 38

4.4. The deep sub-wavelength all-dielectric QED system with a nanoscale gap……... 39

4.5. Purcell emission enhancement of a single QD strongly interacting with the squeezed photonic mode…… 42

4.6. Theoretical calculation of Purcell effect in squeezed photonic waveguide……. 44

4.7. A three-level model of the QD describing its fluorescence intermittence……... 45

4.8. Observation of blinking suppression of the QD coupled to the squeezed photonic mode…….. 46

4.9. Propagation length measurement of the squeezed photonic waveguide…….. 48

4.10. Simulated radiation pattern $|S|r^2$ of light scattered out from an end of the waveguide……..... 49

5.1. Normalized scattering spectra of Ag nanoparticle…….. 57

5.2. Deep sub-wavelength dipole resonators studied……. 58

5.3. Fundamental modes of the HPP crossbar…… 59

5.4. Normalized scattering spectra of HPP crossbar and HPP disk resonators…….. 62

5.5. Tunability of deep sub-λ resonators…… 63

5.6. The HPP disk and HPP crossbar as electrically small resonators…… 64

5.7. Effective mode volume of sub-λ resonators…… 64

5.8. Quality factor and Radiation efficiency…….. 65

5.9. Q_{rad} with respect to Chu size parameter ka_{Chu}……. 67

5.10. Radiative efficiency Q/Q_{rad} of sub-λ resonators…….. 68

5.12. Purcell factor inside the HPP disk and HPP crossbar resonators…… 69

List of Tables

5.1. Fraction of out-coupling into the Ag-strip waveguide for HPP crossbars…… 66

Acknowledgements

First of all, I would like to express my gratitude to my academic advisor, professor Xiang Zhang, for his support and guidance throughout my PhD at UC Berkeley. He has created an inspiring environment in which scientific ideas could be explored without financial constraints and I have enjoyed freedom to choose my own research topics. I appreciate his encouragement to ask critically important questions, to value the pursuit of scientific knowledge and the ability to communicate it effectively to an audience. Thanks to Professor Zhang, I have learned invaluable skills in managing research projects, in collaborating with peers and other life skills which go beyond science itself.

The work presented in this dissertation would not have been possible without the great minds that I have collaborated with. Among them is my mentor, Dr. Rupert Oulton, to whom I feel indebted for introducing me to the subject of light-matter interaction. His fairness, valuable insights and sheer enthusiasm is a source of inspiration. On the experimental side, I am grateful to Dr. Pavel Kolchin and Dr. Thomas Zentgraf for sharing their valuable knowledge about optical instrumentation. I feel privileged to have worked closely with them.

I also enjoyed working with Dr. Maiken Mikkelsen, Dr. Renmin Ma, Dr. Ertugrul Cubukcu, and Volker Sorger on the experimental projects. Their experience and commitment have been a source of motivation and have helped me complete the works. Moreover, I am grateful to my colleagues: Sui Yang, Sadao Ota, Jun Suk Rho, Chris Gladden, Rebecca Kramer and Erick Ulin-Avila for sharing their expertise and their willingness to help with chemical synthesis and fabrication. Yongmin Liu and Dr. Alessandro Salandrino have also been particularly helpful in teaching me how to do simulation and giving comments on the theory that I have developed. I also benefited a great deal from lively discussion with other friends in professor Zhang's research group throughout the five years of my PhD.

Lastly, all the friends that I interacted with during my PhD have made my life much more enjoyable and meaningful. Hope we continue to stay in touch.

Chapter 1
Introduction

Understanding the properties of light and how it interacts with matter has been a subject of human curiosity for centuries. The advent of light bulbs, radio transmission, lasers, fiber optics and finally the internet, which are the product of this understanding, has greatly shaped our modern society. With today's growing demands for processing power and communication bandwidth comes the need for bridging the computing unit which is made up of electrons in transistors with light that is used to transmit information over long distance.

In the past twenty years, electronic transistors have shrunk in size leading to exponential growth in packing density on a computer chip to meet the demand for computing power. Research on optoelectronic devices has seen similar trend of miniaturization, as several optical components have been fabricated monolithically on the same semiconductor chip to a sophisticated degree of integration. However, most optical components are required to have at least a wavelength in size in order to be operational. Recent interests in the use of metals to design optical components offers a way to designing optics at the sub-wavelength scale[1], [2]. Optical properties of metals in the near infrared and visible frequencies enable such technology which is based on a coherent oscillation of surface charge density oscillation on a metal surface called surface plasmon polariton.

The burgeoning field of plasmonics not only provides a solution for making compact optical devices, but also addresses the fundamental issue of light-matter interaction. Optical radiation originates from electronic transitions between quantized energy states in materials, but the characteristic length scale of electrons is typically much smaller than the wavelength of light. This size mismatch causes most interactions between light and matter to be inherently weak. An optical emitter is usually considered as a point dipole which is known in microwave antenna theory to be sub-optimal compared to a half-wavelength antenna[3], [4]. Optical components that operate at subwavelength regime provides a method to shrink the optical fields to match that of electronic wavefunction, thereby enhancing optical interaction. Scaling down the size of optical devices to match that of electronics also makes electronics integrates with optics more seamlessly. In other words, device miniaturization strengthens intrinsically weak light-matter interactions towards faster, more efficient and novel optoelectronic functionalities. Miniaturization in optics has led to the development of novel light sources such as low-threshold lasers [5–7]and single photon sources [8], [9], improvement in optoelectronic devices [10], and molecular sensing [11].

Another aspect of miniaturization which is emphasized in this dissertation is planarization of optical components. Planarization allows routing light signal on a chip and integrating different components into a photonic circuit. Recent research on microdisk resonators[12–14] and 2D photonic crystal cavities[15–17] that are integrated with photonic waveguides are examples of the potential for device integration which increases functionalities and information processing capability. In particular, the use of broadband waveguides which interacts strongly with quantum optical emitters provide a promising platform for quantum information processing[18–20] where an emitter in such a system serves as a processing node that maps its quantum state into a photon

that transmits along the waveguides and carries information from one node to another in the network. The research presented in this dissertation involves the design of photonic components towards that capability.

The dissertation begins by introducing the theory of optical interactions between photonic structures and emitted radiation in Chapter 2, with a special focus on non-resonant, broadband wave-guiding structures as opposed to conventional high quality-factor microcavities. This discussion lays out a theoretical framework that will be used repeatedly in later chapters.

Chapter 3 discusses an experimental study of molecular emission efficiently coupled into deep sub-wavelength propagating modes of a hybrid plasmon (HPP) waveguide. A reduction of photoluminescence lifetime of ensemble dye molecules in the HPP waveguide is observed and provides a probe of dramatic field concentration and its resulting enhanced emission[21].

Chapter 4, on the other hand, describes an experiment on strong optical interactions at single photon and single emitter level based on a low-loss all-dielectric deep sub-wavelength waveguide. The method for observing strong interaction and large Purcell enhancement is achieved by placing individual quantum dots in the optimal environment with the help of atomic force microscope(AFM) manipulation. Central to the experiment is the implementation of a particular waveguide design which allows straightforward integration of optical imaging with mechanical manipulation. Measurements of single photon dynamics are conducted comprehensively therein.

Chapter 5 explores theoretically the radiation properties and optical confinement in an extreme case of the first-order longitudinal mode of a hybrid plasmon cavity, obtained by scaling down the lateral dimensions of the hybrid plasmon square cavity to size on the order of the effective hybrid plasmon wavelength. Lastly, we conclude the subject and provide future directions in Chapter 6.

Chapter 2
Theoretical Background

At the heart of nano-optics lies the subject of light-matter interaction. Before Purcell's seminal paper in 1948 [22], spontaneous emission was considered an intrinsic property of atoms or molecules. Since the establishment of the idea that spontaneous emission of an optical emitter can be modified by its optical environment, the field of quantum electrodynamics was born and had historically led to several technological advancements including novel light sources, such as low-threshold lasers[5], [6] and single photon sources[8], [9], [23], improvement in optoelectronic devices[10], and molecular sensing and spectroscopy[11]. Modification of radiation behavior by the Purcell effect allows one to tailor emission properties such as the decay rate, amplification rate, radiation angle, and purity and fidelity of the emitted optical fields. Spontaneous emission is an important fundamental process relevant to many other optical processes such as optical absorption and stimulated emission, as manifest, for example, in the Einstein relation. The scope of this chapter is to discuss optical interactions between photonic nanostructures and emitted radiation and to lay out a theoretical framework that will be used repeatedly in later chapters.

Traditionally, Purcell enhancement effect is achieved by placing an emitter with narrow emission line-width inside an optical resonator with size of the order of the light wavelength, in which the electromagnetic field is confined three-dimensionally[13], [16], [24–27]. As a consequence, the mode spectrum become discretized, and the amplitude of the vacuum field fluctuation, which causes the spontaneous emission, can be significantly modified. The expression for resonant Purcell factor F_P gives an enhancement of emission decay rate in a optical cavity in comparison to the homogeneous medium.

$$F_P = \frac{3}{4\pi^2}\left(\frac{\lambda}{n}\right)^3 \frac{Q}{V_{eff}} \qquad 2.1.$$

where Q is the quality-factor, V_{eff} is the effective mode volume of the cavity, n is refractive index of the embedding medium of the emitter (considered to be an electric dipole transition) and λ is free-space emission wavelength.

The decay rate of the emitter inside the cavity depends on exact spatial position of the emitter relative to electric field maximum, emission wavelength with respect to the cavity resonant wavelength, and the dipole orientation with respect to the field polarization of the optical mode. All of these can affect the measured decay rate γ to deviate from the expression for F_P above. In other words, one could also redefine Purcell effect to depend on emitter position $\vec{r}_0$, polarization $\hat{\epsilon}$, and frequency ω. [28]

$$\frac{\gamma}{\gamma_0} = F_P\left(\frac{\left|\vec{E}(\vec{r}_0)\right|^2}{\left|\vec{E}\right|_{max}^2}\right)\frac{\Delta\lambda_c \cos^2\theta}{4(\lambda_e - \lambda_c)^2 + \Delta\lambda_c^2} \qquad 2.2.$$

where λ_e is emission wavelength, λ_c is resonance wavelength and $\Delta\lambda_c$ is the linewidth of the cavity, $\cos\theta$ is the dipole orientation factor where the angle is subtended between the dipole and the electric field at emitter position.

The two important features that gives rise to Purcell enhancement as contained in the expression for F_P are :

1. Long interaction time between emitter and photon

The quality factor of an optical cavity Q is the ratio of stored electromagnetic energy in the cavity per cycle to dissipated power. Large quality factor which yields the Purcell enhancement results in a photon emitted from the emitter to be reflected at the cavity mirror and to interact with the emitter several times before eventually leaking out of the cavity.

2. Small effective mode volume

A large Purcell enhancement requires effective mode volume V_{eff} at least as small as the cubic wavelength $\left(\frac{\lambda}{n}\right)^3$. Firstly, a small enough cavity ensures that the free spectral range (FSR) between the longitudinal modes are large enough for the emitter to selectively interact with particular optical modes. Further reduction of effective mode to sub-wavelength (sub-λ) size is equivalent to achieving confinement of vacuum field.

These two features in the standard F_P formula intuitively provides the basic ingredients for designing nanophotonic structures, namely slow light and sub-λ field confinement. The rest of this chapter discuss in details the ways in which these two aspects are realized.

One major trend in optoelectronics device is miniaturization. Miniaturization mitigates the trade-off between speed/bandwidth vs. size by relaxing the Q-factor requirement and tuning of the cavity resonance to match that of the active material[29]. Typically one designs a microcavity or a photonic crystal cavity for largest possible Q-factor within the intended bandwidth of operation while keeping the cavity size as close to the cubic wavelength.

In the following sections, we discuss the use of semi-classical theory to derive broadband Purcell factor in a two-dimensional waveguide (confined in one transverse dimension to the propagation axis) and a one-dimensional continuum (confined in two transverse dimensions to the propagation wave-vector). The semi-classical derivation here follows closely that in references [30–32]. The significance of strong optical interaction in a 1D continuum are then highlighted. In section 2.2 exact classical analytic theory of spontaneous emission in 2D structures [33], [34] are explored as a special case and will be used to validate the quantum semi-classical approach in section 2.1. The analytic theory yields a comprehensive picture of several decay channels involved in plasmonic structures that is otherwise not fully captured by semiclassical theory. The peculiarity of surface plasmon polariton and other related photonic modes are also highlighted therein. Finally, section 2.3 describes the use of numerical techniques based on finite-element methods to calculate dipole emission in general geometries.

2.1. Broadband Purcell enhancement of spontaneous emission

According to quantum semi-classical theory, spontaneous emission is caused by fluctuations of vacuum electromagnetic field. The photonic environment can be altered by modifying the density of optical modes, to which the electronic transitions of the emitter can couple, and/or by modifying the amplitude of the vacuum field at the emitter location. The decay rate γ of an electric dipole $\vec{p}$ at a position $\vec{r}_0$ into optical fields with density of state $D(\omega)$ can be described by Fermi's golden rule.

$$\gamma(\vec{r}_0;\omega) = 2\pi|g(\vec{r}_0;\omega)|^2 D(\omega) \qquad 2.3.$$

g is the coupling strength between the electric dipole and the electromagnetic field at the dipole location. Consider an optical mode characterized by a wave-vector and polarization $(\vec{k},\hat{\epsilon})$.

$$\left|g_{\vec{k},\hat{\epsilon}}(\vec{r}_0;\omega)\right|^2 = \left|\frac{\vec{p}.\vec{E}_{vac}(\vec{r}_0)}{\hbar}\right|^2 \cong \frac{\omega\, p^2}{2\hbar\varepsilon_0\varepsilon\, V_{eff}} \qquad 2.4.$$

In the last identity, we ignore the factor due to the orientation of the dipole with respect to the electric field polarization and have defined a effective mode volume V_{eff} by normalizing the electromagnetic energy of the mode to that of the vacuum field.

$$\frac{\hbar\omega}{2} = \varepsilon_0\varepsilon|\vec{E}_{vac}(\vec{r}_0)|^2 V_{eff} = \int w_{em}(\vec{r})\, d^3\vec{r} \qquad 2.5.$$

$w_{em}(\vec{r}) = w_e(\vec{r}) + w_m(\vec{r}) = \frac{1}{2}\varepsilon_0\frac{d(\omega\varepsilon(\vec{r}))}{d\omega}|\vec{E}(\vec{r})|^2 + \frac{1}{2}\mu_0\mu(\vec{r})|\vec{H}(\vec{r})|^2$ is the electromagnetic energy density

From this point, we may further set $|\vec{E}_{vac}(\vec{r}_0)|^2 \to |\vec{E}_{vac}|^2{}_{max}$ for a position-independent value of V_{eff}

Optical density of states of a cavity $D(\omega)$ is obtained by counting the number of modes in the wave-vector space.

For a one-dimensional waveguide, we obtain [30], [32]

$$D_{1D} = \frac{\ell}{\pi v_g} \qquad 2.6.$$

$$F_{1D} = \frac{3}{4\pi}\left(\frac{c/n}{v_g}\right)\frac{\left(\lambda/n\right)^2}{A_{eff}} \qquad 2.7.$$

The effective mode area is now integrated over two-dimensional cross-section of the waveguide, according to $V_{eff} = \ell A_{eff}(\vec{r}_0) = \frac{\ell\int w_{em}(\vec{r})d^2\vec{r}}{\varepsilon_0\varepsilon|\vec{E}(\vec{r}_0)|^2}$

For two-dimensional waveguide [30], [35]

$$D_{2D} = \frac{\ell^2}{4\pi}\left(\frac{\omega}{v_p v_g}\right) \tag{2.8.}$$

$$F_{2D} = \frac{3}{4}\left(\frac{c/n}{v_p}\right)\left(\frac{c/n}{v_g}\right)\left(\frac{\lambda/n}{L_{eff}}\right) \tag{2.9.}$$

The effective mode length is now integrated over one transverse dimension of the slab according to $V_{eff} = \ell^2 L_{eff}(x_0) = \frac{\ell^2 \int w_{em}(x)dx}{\varepsilon_0 \varepsilon |\vec{E}(x_0)|^2}$

These semi-classical expressions for nonresonant Purcell factor in 1D and 2D waveguides prove to be useful to aid intuition for designing guided photonic structure.

Traditionally, the design of optical cavities for enhanced interaction is concerned with reduction of optical loss whether it be due to finite reflectivity at the mirrors, surface roughness scattering or absorption in the materials and the goal was maintain as high Q-factor as possible. However, according to the expressions (2.7) and (2.9) derived semi-classically above, the bandwidth of the optical mode does not appear explicitly in the expressions and we are left with waveguides which are intrinsically broadband. Nevertheless, a similar feature with regard to the time of the optical mode arises as (2.7) and (2.9) reveal that we need a slow guided mode--with group velocity v_g and/or phase velocity v_p slower than the speed of light in the embedding medium c/n. Moreover, the confinement requirement--that the transverse dimension of the mode must be effectively smaller than the wavelength λ/n, i.e. a sub-diffraction-limited optical mode, is ever more important to order to achieve Purcell enhancement.

Dispersion engineering in photonic crystal waveguide can provide slow guided mode [36], [37] in a diffraction-limited mode area, as the periodicity of a photonic crystal unit cell is on the order of the wavelength. On the contrary, it is rather difficult to confine optical field inside a simple dielectric slab waveguide by simply shrinking the slab thickness. Once the thickness approach λ/n a significant fraction of electromagnetic field remains outside the slab as evanescent field so that the mode area is not reduced further.

Surface plasmon polaritons which are coherent electron density waves on a metal-dielectric interface exhibit an area scaling behavior. As demonstrated in its dispersion relation in Figure 2.1, the propagation wave vector is larger than the free-space wave vector and approaches a large value near $\omega_{SPP} = \frac{\omega_p}{\sqrt{2}}$.

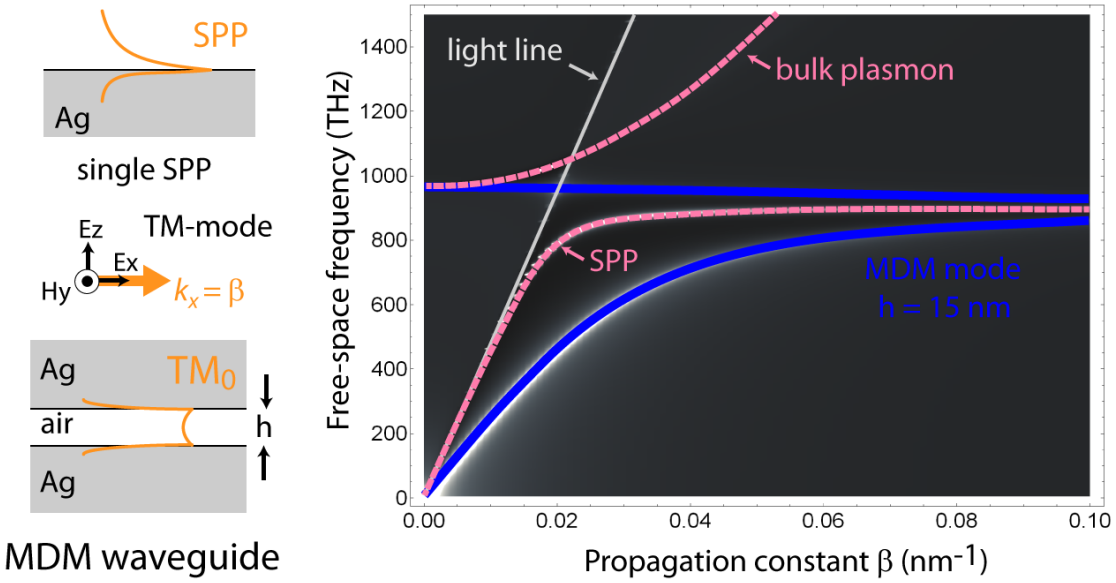

Figure 2.1. Waveguide dispersion relation for a single surface SPP and an MDM 2D waveguide. Schematics of the waveguide structures and their corresponding transverse-magnetic(TM) mode profile H_z are shown in Insets. The dispersion relation for single surface SPP is $\beta_{SPP} = \frac{\omega}{c}\sqrt{\frac{\varepsilon_m(\omega)\varepsilon_b}{\varepsilon_m(\omega)+\varepsilon_b}}$ with $L_{eff} \sim {}^{1}/_{\kappa_z} = \frac{1}{\sqrt{{\beta_{SPP}}^2 - \varepsilon_b({}^{\omega}/_{c})^2}} =$ where ε_b is the dielectric constant of the dielectric half-space (taken to be air, $\varepsilon_b = 1$) and $\varepsilon_m(\omega)$ is the metal dielectric constant, in this case Ag. The dispersion behavior can be separated into a light-like region (characterized by small wave-number β_{SPP} that has similar slope as free-space dispersion (the light line)) and surface-plasmon-like-region (characterized by large wave-vector $\beta_{SPP} \to \infty$). The phase velocity $v_p = \omega/\beta_{SPP}$ and group velocity $v_g = d\omega/d\beta_{SPP}$ is slower than those of free space in the surface-plasmon-like region and asymptotically approach zero at large propagation wave-vector. Moreover, L_{eff} decreases monotonically as the propagation wave-vector gets larger. The range of strong field confinement and slow photon velocity is therefore limited to the frequency bandwidth in the surface-plasmon like regime near the surface plasmon resonance in this case.

Metal-dielectric-metal waveguide considered here has a dielectric gap $h = 15\ nm$. Its dispersion relation (calculated by method given in 2.2) reveals that both v_p and v_g are advantageous over single surface SPP in terms of Purcell enhancement as they are both slower than a single SPP, even in the regime of small propagation wave-vector. More importantly the effective mode length of MDM slab waveguide $L_{eff} \sim h$ (approximately the gap width) regardless of the wavelength. By virtue of the quantum semi-classical approach, non-resonant Purcell enhancement in these structures could be understood intuitively simply from the dispersion relation.

Implication of strong interaction in a 1D continuum.

The one-dimensional waveguide has a special property that its spatial spectrum contains only collinear forward and backward propagating modes so that when the 1D continuum is loaded with emitters along the waveguide, light emitted from one emitter can propagate to and interact with other emitters down the line. The impressive ability to enhance the emission and extraction of photons with high fidelity makes the waveguide an appealing platform for applications in quantum information[18], [19]. Several implementations have been proposed in literatures including an optically addressable photon register which allows storage and retrieval of a photon into and out of a specific quantum emitter loaded down a waveguide that serves as a bus[32], a quantum memory in which the atomic state of the emitter can be efficiently mapped onto the photon state using classical control pulse with high fidelity[19], [32] and single photon switches and transistors[38–41]. Long-range coupling of single emitters along the waveguide can also induce novel entanglement schemes [42].

Classical electrodynamics expression for non-resonant Purcell effect in a waveguide

While the quantum semi-classical expressions discussed above are useful for understanding the role of phase velocity, group velocity and mode confinement in the Purcell factor, we have assumed in the definition of effective mode volume (5.2) that the structure is made wholly of non-dispersive media such that the total electromagnetic energy of the mode is split equally between electric and magnetic energy. For a propagating mode in structures containing dispersive medium such as metal, this assumption is far from accurate and call for a more appropriate formula and re-interpretation of basic results above. Power radiated from an electric dipole in a waveguide could be derived entirely classically by the modal expansion method [43]. Alternatively, we present here the semi-classical argument to arrive at the same result as classical theory. The only difference from the semi-classical approach in previous section is that here we quantize the power flux of the propagating mode instead of the energy density of a stationary field in order to take into account the imbalance between electrical and magnetic energy which is inherent to plasmonic waveguides. The final result of this derivation highlights the importance of energy velocity rather than the group velocity.

The electromagnetic field of the mode is normalized to vacuum fluctuation by a normalizing factor α so that $|\vec{E}_{vac}(\vec{r}_0)|^2 = |\alpha\vec{E}(\vec{r}_0)|^2$

$$\frac{\hbar\omega}{2c} = |\alpha|^2 \int \frac{1}{2c^2} Re\left(\vec{E}(\vec{r}) \times \vec{H}^*(\vec{r})\right) d^3\vec{r} \qquad 2.10.$$
$$= |\alpha|^2 \int \frac{S_z(x,y)}{2c^2} dxdy\, \ell$$

S_z/c^2 is Abraham's pure electromagnetic momentum density [44] of the optical mode. $\mathrm{D_{1D}} = \frac{\ell}{\pi\, \mathrm{c}}$ is the one-dimensional density of states of pure photonic field and ℓ is arbitrary quantization length along the waveguide. The effective mode area and effective mode volume may therefore be defined as $\mathrm{V_{eff}}(\vec{r}_0) = \ell\, \mathrm{A_{eff}}(x_0, y_0)$.

We obtain the final expression for the Purcell factor in a one-dimensional continuum

$$F_{1D}(x_0, y_0) = \frac{3\lambda^2}{8\pi} \frac{c\varepsilon_0 \left|\vec{E}(x_0, y_0)\right|^2}{\int S_z \, dA} = \frac{3}{4\pi} \frac{c/n}{v_E} \frac{\lambda^2}{A_{eff}(x_0, y_0)} \quad 2.11.$$

where the coupling rate to the guided mode γ is normalized to the emission rate γ_n in an embedding host medium of index $n = \sqrt{\epsilon}$. S_z is obtained from modal Poynting vector along the propagation direction.

In the final equality of (2.11) we have written the Purcell factor in terms of energy density w_{em} and energy velocity v_E defined using the relationship

$$\int S_z(\vec{r}) \, dA = v_E \int w_{em}(\vec{r}) \, dA$$

We also have defined the effective mode area $A^c_{eff}(x_0, y_0) = \frac{\int w_{em} \, dA}{\frac{\varepsilon_0}{2}\left|\vec{E}(x_0, y_0)\right|^2}$, where superscript c denotes a classical formula.

We interpret the Purcell effect for a waveguide mode as arising from mode area reduction due to a combined effect of strong electrical energy concentration (the denominator of equation 2.11) and a slowdown of the energy transfer (power flux) in the HPP waveguide mode (the numerator of equation 2.11).

2.2. Analytic theory of spontaneous emission in a 2D slab geometry

The general expression for the spontaneous emission of a dipole in a slab junction (geometry shown in diagram below) can be obtained by considering the work done on the electric dipole p (represented by ED in diagram) at position d_t from the top interface and d_b from the bottom interface, by its own reflected field [33].

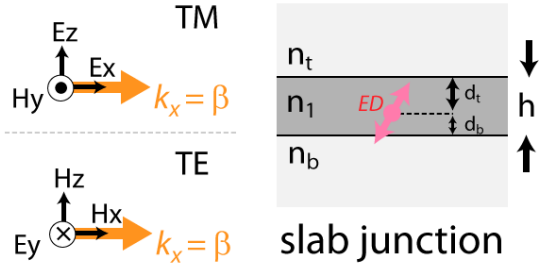

$$F_P = P/P_0 = \frac{3}{2}Re\int_0^\infty du\left\{\frac{u^3}{q_1}(p_\perp/p)^2\left[\frac{\left(1+r_t^p e^{2iq_1d_t}\right)\left(1+r_b^p e^{2iq_1d_b}\right)}{\left(1-r_t^p r_b^p e^{2iq_1h}\right)}\right]\right.$$
$$+\frac{1}{2}\frac{u}{q_1}\varepsilon_1(p_\parallel/p)^2\left[\frac{\left(1+r_t^s e^{2iq_1d_t}\right)\left(1+r_b^s e^{2iq_1d_b}\right)}{\left(1-r_t^s r_b^s e^{2iq_1h}\right)}\right]$$
$$\left.+\frac{1}{2}uq_1(p_\parallel/p)^2\left[\frac{\left(1-r_t^p e^{2iq_1d_t}\right)\left(1-r_b^p e^{2iq_1d_b}\right)}{\left(1-r_t^p r_b^p e^{2iq_1h}\right)}\right]\right\} \qquad 2.12.$$

The expression is written in the form of an integral over the parallel wave vector along the slab junction (i.e. propagation wave vector β). We have normalized the parallel wave-vector component k_x which is continuous across the multilayers as $u = \frac{k_x}{k} = \frac{\beta}{k}$ to the free space wave vector k. The transverse wave vector k_z in each medium j of permittivity ϵ_j are given by $q_j = \frac{k_{z,j}}{k} = \varepsilon_j - u^2$. The top interface has reflectivity r_t^s and r_t^p obtained from Fresnel reflection formula, where the superscript (s,p) signifies (TE,TM) polarization respectively (see Appendix A). Likewise for bottom interface. The electric dipole (ED) has a dipole moment p with in-plane component $p_\parallel$ and perpendicular component $p_\parallel$.

The first and third terms in (2.12) contain poles, written in the form $\beta = k_x = k_0 u$, which are TM-modes of the slab juntion, whereas the poles of the second term are TE-modes. This expression for radiated power shows that the vertical component of the dipole only interacts with the TM-modes (the first term) whereas the parallel component interacts with both TE and TM modes.

The usefulness of the expression above comes from the fact that:

1. The form of the expression $P = \int \frac{dP}{dk_x} dk_x$ resolves dissipated power of the dipole into an angular spectrum (or parallel wave vector) which easily translates into contributions of the optical modes inside the slab junction that interact with the dipole.

2. The details of the cladding media are represented as the reflectivity response r_t and r_p which can easily be generalized to any 2D stacked multilayer system using Fresnel reflection formula and transmission line theory (Appendix A). The formula is general enough to be used for infinitely long 2D waveguide structures under consideration in section 2.3. The residue function of the form $\left|\frac{1}{1-r_t r_b\, e^{2iq_1h}}\right|$ has maxima at its poles and can be used to study modal structures, as in Figure 2.1 for example.

For the deep sub-λ confined modes considered so far in Fig. 2.1 (single SPP and MDM waveguide), the electric field inside the gap is primarily directed normal to the metal surfaces, we expect therefore that only a dipole oscillating normal to the metal surfaces will strongly couple to these transverse magnetic(TM) modes.

$$F_P = P/P_0 = \frac{3}{2}Re\int_0^\infty du\left\{\frac{u^3}{q_1}\left[\frac{\left(1+r_t^p e^{2iq_1d_t}\right)\left(1+r_b^p e^{2iq_1d_b}\right)}{\left(1-r_t^p r_b^p e^{2iq_1h}\right)}\right]\right\} \qquad 2.13.$$

For vertical dipole above a single metal surface. The above expression can be reduced, simply by setting $r_t = 0$, to

$$\frac{P}{P_0} = \frac{3}{2} Re \int_0^\infty du \left\{ \frac{u^3}{q_1} (1 + r^p) e^{2iq_1 d} \right\} \qquad 2.14.$$

where r^p is the TM-wave reflectivity of the metal surface, and d is distance to the metal surface

To illustrate the effect of metal on dipole radiation, Figure 2.2 plots the angular spectrum density of the decay rate for a vertical dipole at a distance $d = \frac{h}{2}$ =7.5 nm over a silver surface at $\lambda =$ 640 nm. The component from u = 0 to u = 1 represents emission into free-space. The narrow peak at $u(\omega) = \frac{k_{spp}}{k} = \sqrt{\frac{\varepsilon_m(\omega)\varepsilon_b}{\varepsilon_m(\omega)+\varepsilon_b}}$ represents coupling of emission to single SPP. The contribution of single SPP to the total decay rate (Purcell factor) may be calculated by expansion of r^p in the vicinity of this pole: $r^p(u \approx u_{SPP}) = 2\frac{\varepsilon_m \varepsilon_b}{\varepsilon_b^2 - \varepsilon_m^2}\left(\frac{u_{SPP}}{u - u_{SPP}}\right)$ [33] and using Cauchy's residue theorem to evaluate the integral. Note that no loss in the metal is required for this process to occur and powered dissipated through this channel propagates as surface wave on the metal surface. In addition, when the dipole is very close to the metal surface ($d < 12$ nm) , a broad peak at large wave-vector region appears which we attribute to lossy surface waves(LSW) Ford-1984, Chance-1978]. These are evanescent waves in metal which are excited by the near-field of the dipole emitter and is estimated to be proprotional to $\frac{1}{d^3}$ using quasistatic approximation $q = iu$ and local dielectric model $r^p = \frac{(\varepsilon_b - \varepsilon_m)}{(\varepsilon_m + \varepsilon_b)}$. Due to its extremely large bandwidth and strong dependence on Ohmic loss of the metal, dissipation through this channel is considered as quenching of dipole radiation [33].

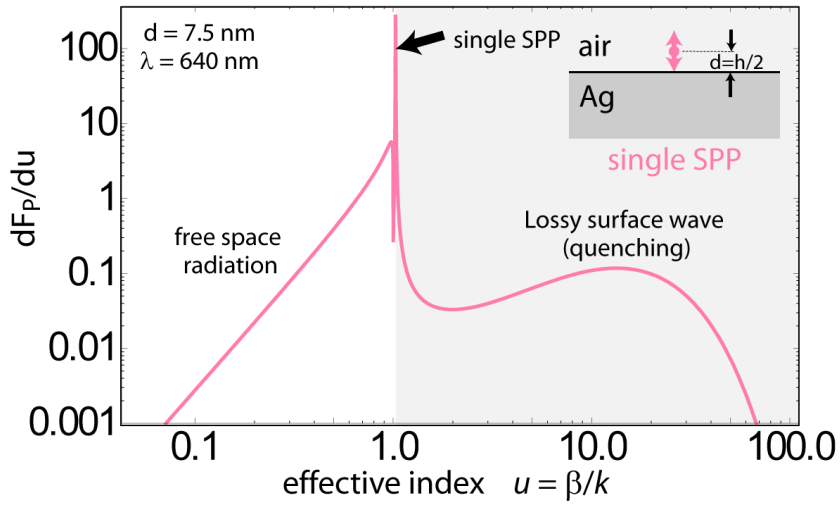

Figure 2.2. Several contributions of dissipation revealed by angular spectrum density of the decay rate. A vertical dipole is at a distance $d = \frac{h}{2} = 7.5$ nm over a silver surface and emitting at $\lambda = 640$ nm. The component from u = 0 to u = 1 represents

emission into free-space. The narrow peak at $u(\omega) = \frac{k_{spp}}{k} = \sqrt{\frac{\varepsilon_m(\omega)\varepsilon_b}{\varepsilon_m(\omega)+\varepsilon_b}}$ represents coupling of dipole emission to single SPP which is a propagating surface wave. The contribution of single SPP to the total decay rate (Purcell factor) may be done by expansion of r^p in the vicinity of this pole: $r^p(u \approx u_{SPP}) = 2\frac{\varepsilon_m\varepsilon_b}{\varepsilon_b^2-\varepsilon_m^2}\left(\frac{u_{SPP}}{u-u_{SPP}}\right)$ [33] and using Cauchy's residue theorem to evaluate the integral. Note that no loss in the metal is required for this process to occur. In addition, when the dipole is near the metal surface, a broad spectrum at large wave-vector region appears which we attribute to lossy surface waves(LSW). These are evanescent waves in metal which are excited by the near-field of the dipole emitter and then dissipate as heat. The decay rate due to LSW is estimated to be proprotional to $\frac{1}{d^3}$ [33] using quasistatic approximation $q = iu$ and local dielectric model $r^p = \frac{(\varepsilon_b-\varepsilon_m)}{(\varepsilon_m+\varepsilon_b)}$.

Now, we are interested in the bandwidth property of Purcell enhancement effect. Figure 2.3 shows the dependence of F_P with the emission wavelength for vertical dipole over a metal surface and inside a metal-dielectric-metal (MDM) slab junction waveguide. Schematics of the waveguide structures are shown in the inset of Fig. 2.3. Consistent with earlier discussion about the dispersion relation of single SPP and MDM waveguide in Figure 2.1, large Purcell enhancement on single metal surface arises as the vertical dipole interacts strongly with the SPP mode in a narrow bandwidth near the SPP resonance where the mode is most localized and has the lowest group velocity. The MDM waveguide, on the other hand, exhibits large Purcell factor even at low frequency (long wavelength) due to strong mode confinement at the order of the gap size which is much smaller than the free space wavelength. The Purcell effect in this regime can therefore be said to be non-resonant. The graph also has similar resonant peak near SPP resonance as that of single SPP. Moreover, at frequencies well below the SPP resonance, the guided MDM mode has lower propagation loss so that strong optical interaction which excites the mode at these frequencies can be guided over long distances.

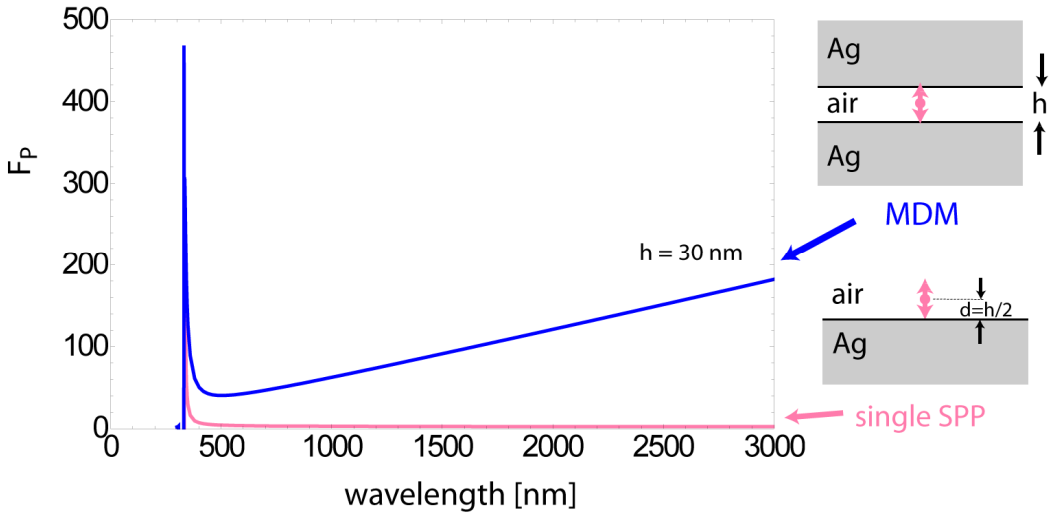

Figure 2.3. Broadband, non-resonant Purcell effect. Purcell effect of a vertical dipole emitter at a distance $h/2$ over metallic half-space, at midgap inside a MDM junction waveguide h =15 nm as a function of free-space wavelength. Schematics of the setup are shown in the Insets (metallic half-space and MDM junction waveguide). The metal is assumed to be Ag with Drude model dielectric function that is fitted to data from literature [45]. Consistent with earlier discussion about the dispersion relation of single SPP and MDM waveguide in Figure 2.1, large Purcell enhancement on single metal surface arises as the verticle dipole interacts well the SPP mode in a narrow bandwidth near the SPP resonance where the mode is most localized and has the lowest group velocity. The MDM waveguide, on the other hand exhibits large Purcell factor even at low frequency (long wavelength) due to strong mode confinement at the order of the gap size compared to the free space wavelength. It also has similar resonant peak near SPP resonance as that of single SPP. Moreover, at frequencies well below the SPP resonance, the guided MDM mode has lower propagation loss so that strong optical interaction which excites the mode at these frequencies can be guided over long distances.

2.3. Hybrid plasmon waveguide, Dielectric slot waveguide, and Slot-PEC (dielectric half-slot) waveguide

The Purcell factor formula for the junction waveguide (2.13) is used to study the optical interaction of an electric dipole transition in three related sub-λ waveguide structures. A hybrid plasmon polariton waveguide (HPP) is made of a slab of high refractive index dielectric material of thickness d, placed at a small distance above a plasmonic metal half-space with a gap region of thickness h. The photonic mode in the dielectric slab hybridizes with the surface plasmon to form a highly confined guided mode with long propagation length [46–48]. High index contrast across the narrow gap region ensures that dielectric discontinuity produces a large normal electric field in the low index gap region, much like electric fields inside a capacitor. The HPP mode is transverse-magnetic (TM) and is dominated by vertical electric field component so it will interact mainly with a vertical electric dipole.

The calculated residue function from the angular spectrum of radiated power from the dipole shows modal structure of hybrid plasmon waveguide as in Figure 2.4. For most gap sizes, the effective index of the hybrid plasmon mode lies between the refractive index of the dielectric and the single SPP (air/Ag interface). As the gap size decreases the mode shifts away from the dielectric slab mode to higher values of effective index as a result of the increasing degree of hybridization with the surface plasmon and subsequent shrinking of the effective cross-section of the mode. For extremely small gap size h < 2 nm, the HPP effective index shifts entirely to a value above the index of the dielectric (n_{Si}) and approaches that of single SPP on Si/Ag interface and becomes significantly more lossy as evident in the linewidth broadening.

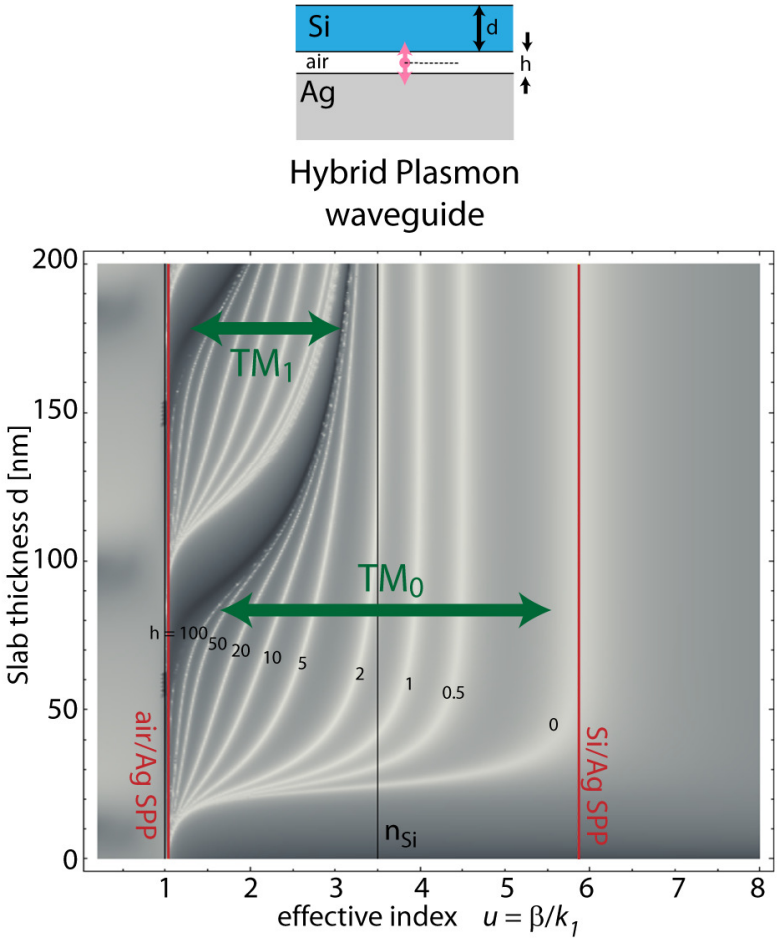

Figure 2.4. HPP modes for varying gap thickness h and Si slab thickness d. The horizontal axis is the effective index of the mode. In this calculation, the wavelength is assumed to be $\lambda = 620$ nm, so that the permittivity of Ag, $\varepsilon_m = -19 + 0.5\mathrm{i}$ [45]. This density plot is calculated from the residue function. For most gap size, the effective index of the hybrid plasmon mode lies between the refractive index of the dielectric n_{si} and the effective index of single SPP (air/Ag interface). As the gap size decreases the mode shifts to higher value of effective index as a result of the increasing degree of hybridization with the surface plasmon and subsequent shrinking of the effective cross-section of the mode. For extremely small gap size h < 2 nm, the HPP effective index shifts entirely to a value above the index of the dielectric (n_{si}) and approaches that of single SPP on Si/Ag interface.

A typical angular spectrum density of the decay rate for HPP waveguide possesses multiple decay channels, characteristic to plasmonic-based waveguides similar to single SPP in the previous section. In this case, there appears poles corresponding to coupling to hybrid plasmon modes and lossy surface wave. At large enough slab thickness $d > 100\ nm$, the waveguide supports higher order transverse modes and more than one hybrid plasmon mode appears. The contribution of free-space radiation, single SPP, lossy surface waves and different hybrid plasmon (HPP) modes are separated in wave vector space u in similar way. The result is shown in Figure 2.5

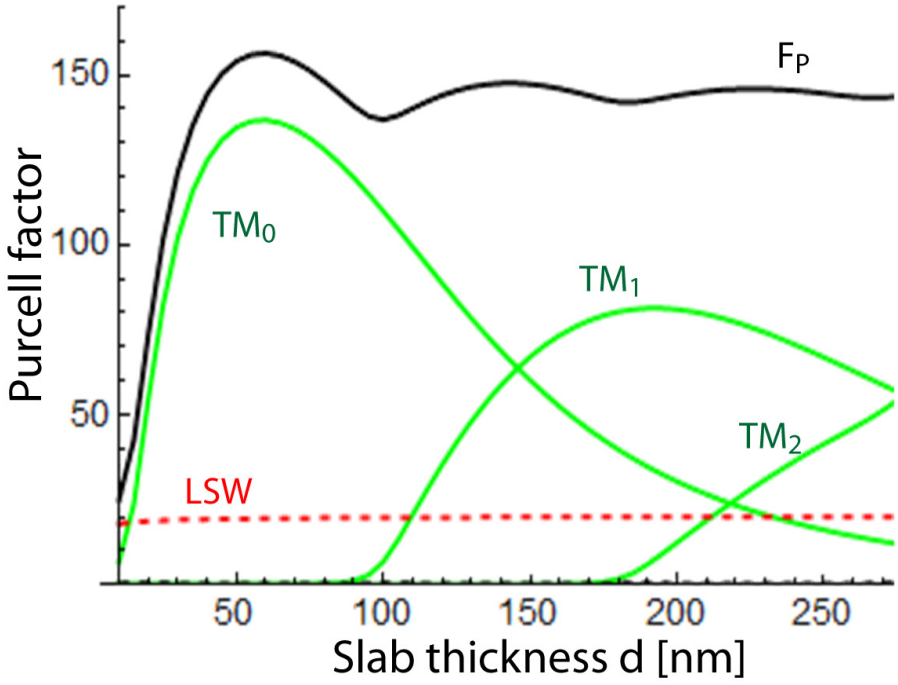

Figure 2.5. Different modal contributions to the Purcell factor of HPP slab waveguide, including metal quenching (LSW). First-order HPP mode (TM_0) and higher order HPP modes (TM_1 and TM_2), which appear as slab thickness d increases, are shown as green solid line. The gap thickness h is fixed at 10 nm in this calculation. Nonradiative metal quenching or lossy surface wave (LSW) is a constant red, dashed line since it depends on the distance of the emitter to the metal surface only. Free space emission is not plotted in the graph. The sum of all contributions gives the total Purcell factor (black solid line) which approaches a constant value even at large slab thickness where the dipole emitter interacts with multiple transverse HPP modes.

Non-radiative decay into LSW or quenching by metal is merely a function of distance from the emitter to the metal. At larger Si slab thickness d where the waveguide also supports higher-order transverse HPP modes (TM_1 and TM_2), the modal Purcell effect for these higher order modes are quite considerable due to the fact that the field is still concentrated inside the gap region. More interestingly, total Purcell factor does not drop as one scales up the slab thickness d, as each higher-order transverse guided mode takes part in coupling radiation from the dipole in place of the lower-order one. The total Purcell factor remains high even in the limit of infinite dielectric medium above the air gap, in which case no discrete guided mode exists but a continuum of leaky modes with evanescent field confinement in the gap region.

We investigate related waveguide structures, namely dielectric slot waveguide [30], [49] made of two identical slabs of high refractive index dielectric material separated by a small gap $2h$. Field enhancement in the gap occurs due to high refractive index contrast in much the same way as the hybrid plasmon waveguide. As another model system, we replace the plasmonic metal with a perfect electric conductor (PEC) mirror with $\varepsilon_m = -\infty$ so that reflectivity of the air-PEC interface is unity. This waveguide is equivalent to a half-slot where the mode profile is the same as that of the symmetric mode of the slot waveguide but the region in which the electromagnetic

field exist is only half of the gap thickness of the slot. The resulting Purcell factor calculated in this half-slot configuration consistently doubles from the value of the dielectric slot waveguide previously, as a result of halving the effective modal cross-section. However, it is still much less than in hybrid plasmon waveguide despite having the very similar structure. An explanation lies in an imbalance of electric and magnetic energy in the hybrid waveguide as compared to the half-slot waveguide. The dispersion of metal near the visible wavelength region which supports surface plasmon polariton slows down the propagating wave because the energy is stored preferentially in the oscillation of electric charge. Moreover, when the propagating wave contains more electric energy than magnetic energy, the vacuum electric field is also enhanced greatly and interacts with the dipole emitter much more strongly than a pure dielectric guided mode of equivalent geometry.

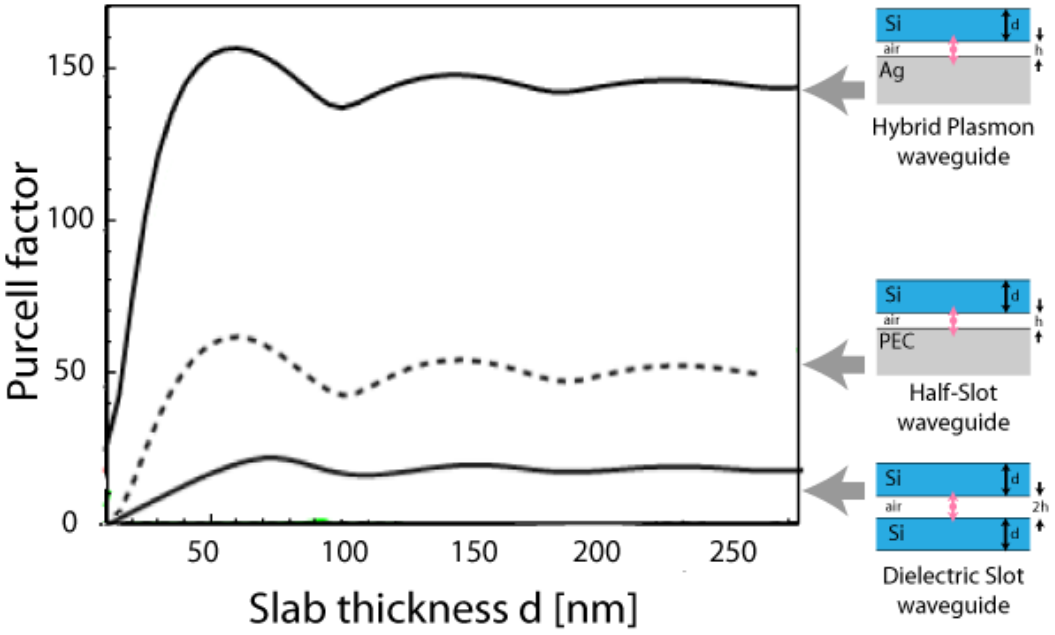

Figure 2.6. Comparison among related sub-λ 2D waveguide structures.

2.4. Purcell effect simulation using finite element method

The analytical method was useful in describing the multiple decay channels and understanding the basic features of spontaneous emission in plasmonic waveguides. For more general geometry, numerical electromagnetic simulation based on finite-element method (FEM) can be used to study optical interaction. In the following, the two methods used in this dissertation are introduced.

1. Eigenmode simulation for modal Purcell effect. The expression for Purcell factor in 1D and 2D waveguide obtained in section 2.1. can be related to the field distribution solved by an eigenmode solver. The dependence of dipole location and orientation could be studied in simple terms. In a configuration that supports highly confined modes and the dipole is placed near the

field maximum and aligned with the mode polarization, the modal Purcell factor calculated in this way have a large contribution in the total Purcell factor.

When calculated F_P is less than unity, the dipole does not interact strongly with the waveguide mode and may couple to other decay channels available in the system, for example, free-space radiation, single surface SPP, and lossy surface wave. This suggests the limitation of the eigenmode solution method that it does not necessarily capture all the possible decay channels that occur in an experiment.

2. Steady-state harmonic propagation formulation where one models the emitter as a small nanometric-size dipole with finite current or a point electric dipole with a finite dipole moment located in an electromagnetic environment of interest. The total Purcell factor which includes all possible decay channels are obtained by comparing the power dissipated by the dipole in the structure to that in free-space $F_P = \frac{P}{P_0}$.

An infinite structure such as a waveguide without termination can be implemented by creating a perfectly matched layer (PML) around the simulation domain, with the end of the waveguide impinging into the PML to minimize backward reflection. The Purcell factor found in this way is highly consistent with that obtained with eigenmode solution. The radiated field follows the mode profile of the waveguide when the dipole emits strongly into the waveguide mode. The added benefit in the full-field finite-element method simulation is that the effect of sub-optimal dipole orientation and its coupling to parasitic decay channels can be studied.

The power dissipated as Ohmic loss in lossy materials and excitation of lossy surface wave can be calculated directly from the results of simulations by integrating resistive heating over the domain of the lossy material $P_{loss} = \int \left(\frac{1}{2}\omega\, Im[\mathcal{E}(\vec{r})]\left|\vec{E}\right|^2\right) dV$. However, this formula also includes the modal propagation loss which should be treated separately, rather as radiative coupling into the waveguide mode. This means radiative dissipation into propagating waves $P_{rad} = P_{mode} + P_{SPP} + P_{free}$ tends to be underestimated, depending on the length of waveguide domain, whereas P_{loss} is overestimated. Nevertheless, the total Purcell factor $F_P = \frac{P_{loss}+P_{rad}}{P_0}$ is unaffected and is rather accurate.

Validity of the finite-element method simulation of the Purcell effect is checked against the analytical method described in section 2.2 for a vertical dipole situated at a distance d over an Ag surface. Comparison between FEM and analytical results reveal excellent agreement as shown in Figure 2.7. The emission wavelength is assumed to be $\lambda = 640$ nm with the value of Ag permittivity according to Ref.[45] It appears that the contribution of lossy surface wave (LSW) are captured well in the finite-element harmonic propagation simulation, even if, according to analytic theory described in section 2.2, the very large and broad bandwidth wave vector associated with this dissipation process involves nanometric length scale (mode index of order 100-1000). The reason for this agreement is that LSW are excited and is restricted right in the vicinity of the dipole emitter where the finite-element mesh size remains of the order of the dipole size itself and has yet to grow (typical mesh size is ~ 1 nm). The simulation method is therefore quite efficient and sufficient to accurately capture LSW or metal quenching.

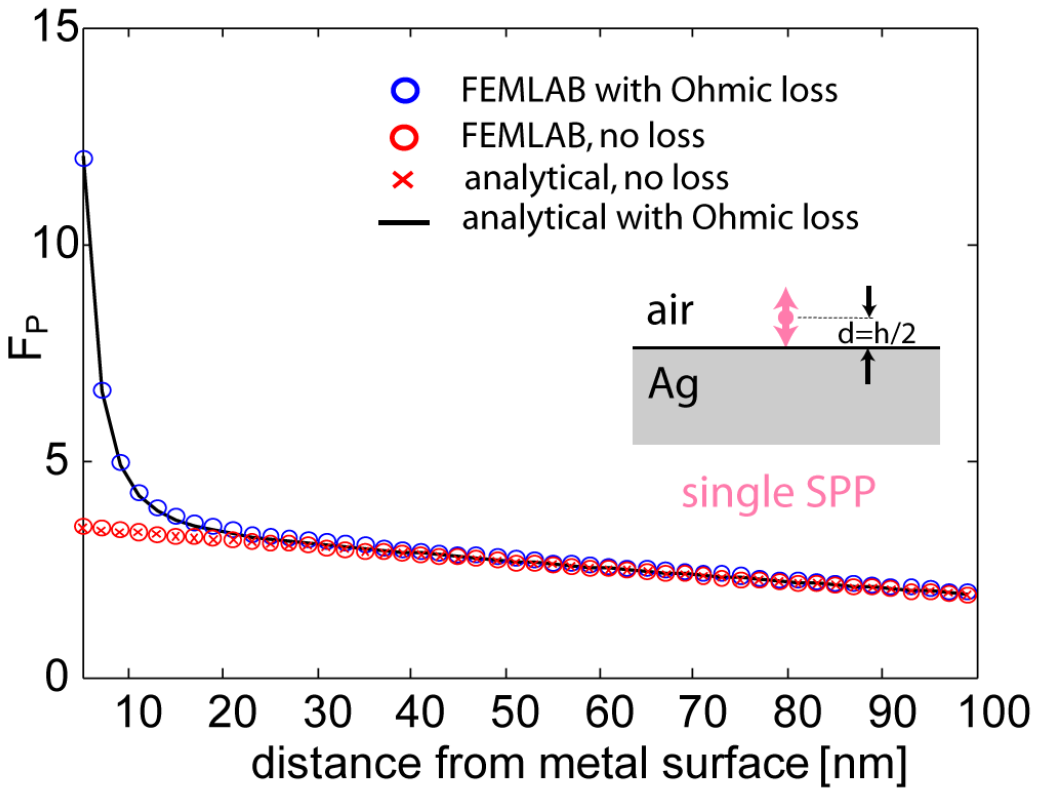

Figure 2.7. Validity of finite-element method simulation. The plot shows Purcell effect of a vertical dipole situated at a distance d over an Ag surface. Comparison between the result of FEM (blue and red circles) and analytical method (black line, red cross) described in section 2.2 reveals excellent agreement. The emission wavelength is assumed to be $\lambda = 640$ nm with the value of Ag permittivity according to Ref.[45].

As for the problem of distinguishing the contributions of non-radiative (loss) and radiative dissipation in the finite-element method simulation described above, a solution is found by doing a separate simulation where Ohmic loss in absorptive materials in the system is neglected. The calculated total Purcell factor F_P in this lossless configuration yields purely radiative contribution $F_{rad} = P_{rad}/P_0$. Radiative Purcell factor from FEM simulation obtained in this manner (red empty circles) is also shown in Figure 2.7 and agrees well with that obtained by singling out loss from the angular spectrum of the analytical formula in section 2.2 (red cross).

Purcell factor simulation with FEM can be combined with modal Purcell factor to obtain waveguide coupling factor $\beta = \frac{F_{mode}}{F_P}$. It is also useful for simulating general three-dimensional structures including terminated waveguides and cavity. Moreover, it yields further information about emitted near-fields, and far-field radiation pattern which can be obtained via the built-in Stratton-Chu transformation formula, provided that the structure is enclosed in a uniform homogeneous medium. This could be used to study where the radiation goes and to estimate the photon extraction efficiency. The method is used to validate experimental results in Chapter 3 and 4.

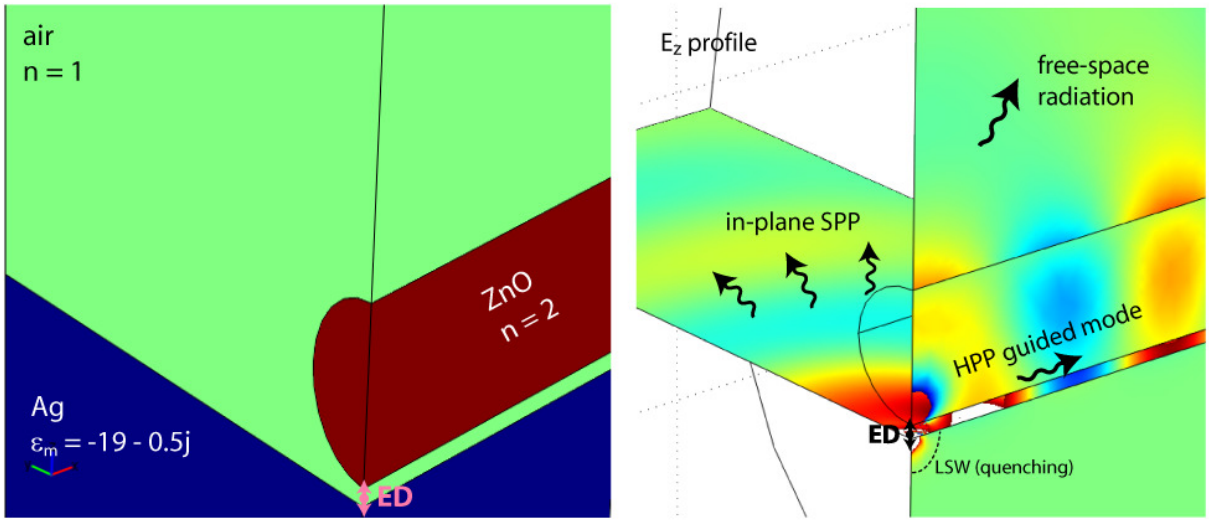

Figure 2.8. An example of simulated radiated field of a vertical electric dipole emitting from midgap of a one-dimensional HPP waveguide. The geometrical and material configuration shown in Left panel. (nanowire diameter = 200 nm, gap = 20 nm, $\lambda = 640$ nm, and electric dipole at mid-gap marked as ED) By symmetry of the problem, the cut planes shown here are set as perfect magnetic conductor (PMC) which reduces the simulation domain to a quarter of the full domain. (Right panel) Electric field profile of the vertical field component (E_z) showing field characteristics reminiscent of different decay channels expected in this geometry. Free-space radiation, single SPP on metal surface, HPP guided mode and quenching are marked in the figure.

2.5. Summary

In this chapter, we have derived semi-classically the conditions for an optical 1D and 2D continuum to enhance dipole radiation, namely slow guided wave and sub-wavelength field confinement. We analyzed the way in which a electric dipole emitter near a metal surface can emits rapidly into a surface guided mode (surface plasmon polariton) but strong effect only occurs at frequency near the surface plasmon resonance of the metal-dielectric interface. We focused on the hybrid plasmon (HPP) geometry which non-resonantly enhances dipole radiation by virtue of confinement in its low permittivity gap region that is geometrically tunable. Hybridization of a dielectric slab mode with the surface plasmon allows such degree of tunable confinement. In addition, the multimodal nature of dissipation of the dipole emitter in HPP geometry is discussed, including the role of non-radiative quenching due to Ohmic loss in the metal. Related designs using high-permittivity-contrast dielectrics (dielectric slot waveguide) are also presented as an alternative. The 2D hybrid plasmon and dielectric slot waveguide geometries provide the basis for the 1D waveguides and resonators which are studied in details in chapter 3, 4 and 5.

On the theoretical side, exact analytical theory provides a basic understanding of several mechanisms for spontaneous emission in the presence of dielectric metallic interface: free space radiation, specific optical modes, surface plasmon mode, and metal quenching. On the other hand, the simplicity of semi-classical theory allows one to relate a calculated optical mode to its

modal Purcell factor which is useful for designing a deep sub-wavelength waveguide. Numerical methods for calculating Purcell effect in a general 3D structure (whether it be a true one-dimensional waveguide or a cavity) are also developed. This information, in combination with modal Purcell factor and basic knowledge of different decay channels, provides a comprehensive theoretical picture for understanding emission in deep sub-wavelength nanophotonic structure and aids in device design.

Chapter 3
Hybrid Plasmon Waveguide: an experimental probe of deep sub-wavelength optical interaction by molecular fluorescence

Enhancement of spontaneous emission rate [22] has enabled efficient light-emitting devices and single photon sources [8], [9], [23], reductions in laser thresholds [5]and high sensitivity resonator sensors [50]. Device miniaturization also strengthens intrinsically weak light-matter interactions towards faster, more efficient and novel optoelectronic functionalities. The analysis in chapter 2 suggests that a class of deep sub-λ guided optical modes including surface plasmon and/or high refractive-index contrast system can enhance optical interaction up to several order of magnitude without the stringent bandwidth limitation of a cavity. In addition, they contain strongly confined region which can scale down to the electronic length scale.

To implement such a scheme experimentally is, however, quite challenging since scaling down the optical mode makes it more difficult to overlap the optical emitters to the optical mode perfectly. Probing confined optical mode in the low index gap region of these waveguides require nanometric scale emitters embedded in low permittivity medium, with high homogeneity of their intrinsic emission lifetime to isolate the dependence of emitter's position and orientation in the measurement. Dye molecules at controllable concentration in a low index polymer film turned out to be a good choice for an ensemble measurement in a solid state device. Other emitters such as colloidal quantum dots and NV^- centers in nanodiamonds have rather high index, occupy too large a volume (diameter of at least 10-35 nm) for the confined mode to scale down, and have too wide variation between emitters so that they tend to produce inconclusive results in an ensemble measurement. Furthermore, while metal-based waveguides are capable of providing deep sub-wavelength modes, the emitter-to-waveguide coupling is limited due to parasitic metallic quenching effects leading to an unwanted reduction in the emitter luminescence efficiency [51–53]. Furthermore, fundamental questions persist regarding the effect of quenching and propagation loss in plasmonic waveguides on the luminescence intensity, and how to distinguish different contributions of decay channels in the experiment and to address the issue of heterogeneity of the emitters inside a waveguide configuration.

This chapter discusses an experimental study of molecular emission efficiently coupled into deep sub-wavelength propagating modes[21] of a hybrid plasmon (HPP) waveguide[46–48]. We measured a reduction of PL lifetime of dye molecules, distributed inside the field-concentrated nano-scale region of the hybrid plasmon mode, up to 60 times as compared to their intrinsic lifetime, and over a broad (>70 nm) spectral bandwidth of the emission. We quantitatively verify the contribution of non-radiative energy transfer to metal as a competing mechanism to emission coupling into the guided mode by a careful design of control measurements and compare them with theory developed in section 2.5. Emission analysis reveals

a 15-20 times lifetime reduction due to strong coupling to the HPP waveguide, in correspondence with a highly-confined modal area of $\lambda^2/80$. Furthermore, we integrate the measured photon flux and observed a six-fold brightness enhancement of the dye molecules in the waveguide structure as compared to flat metal surface. This brightness enhancement is a direct result of high beta-factor of up to 0.75 and good photon extraction efficiency due to low propagation loss in the waveguide. The potential as well as limitations of optical emitter coupling to plasmonic waveguides are demonstrated therein.

3.1. Hybrid Plasmon (HPP) waveguide

The hybrid plasmon (HPP) waveguide structure deployed in this study consists of a high-permittivity dielectric nanowire separated from a metal surface by a nanoscale low-permittivity dielectric gap. The coupling between the plasmonic and waveguide modes across the gap enables capacitor-like electric energy storage that allows effective sub-λ transmission in non-metallic regions with low propagation loss compared to many other plasmonic waveguides [46], [54]. Figures 3.1 shows the electromagnetic power flux profile of the fundamental sub-wavelength guided optical mode in the HPP waveguide design which is made of ZnO nanowire separated from Ag surface by a nanometric thin low index dielectric layer. This quasi-(TM)-transverse magnetic highly-confined mode arises from the continuity requirement of the vertical component of electric displacement (D_y) at the high-index contrast interfaces between the high-index nanowire, the low-index gap region and the metal.

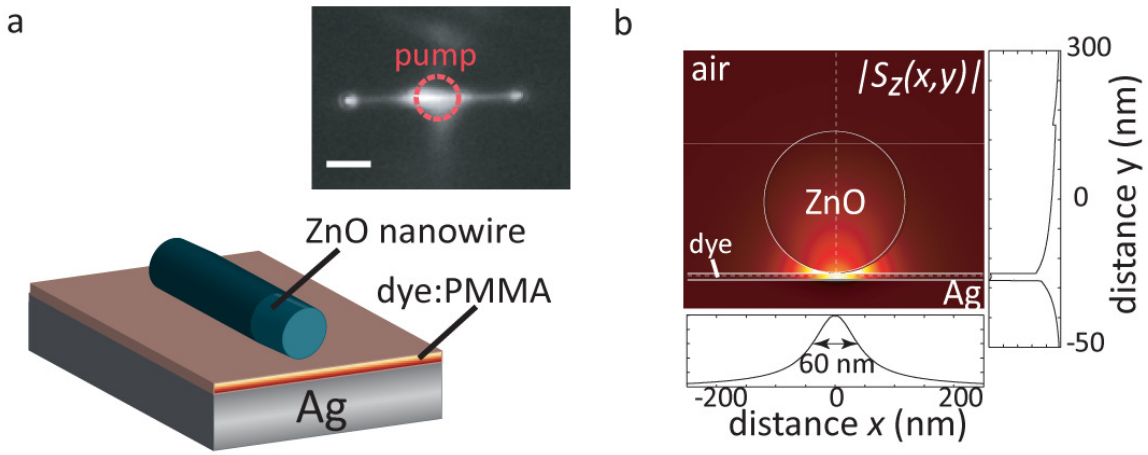

Figure 3.1. Hybrid Plasmon (HPP) waveguide design (a) Schematic of the hybrid plasmon (HPP) waveguide (ZnO nanowire diameter = 80 – 160 nm, length 8 – 10 μm, dye-doped PMMA thickness = 5 – 40 nm). Insets: PL image of emission from dye molecules excited at the center of the nanowire (red dashed circle) coupling to the hybrid-plasmon waveguide and scattering to far field at the ends of the wire, scale bar = 2 μm, (b) The geometry supports a deep sub-wavelength ($\lambda^2/80$) propagating optical mode for gap thickness g = 5 nm. Varying g tunes the optical confinement.

3.2. Experimental method

In our experiment, we fabricate hybrid plasmon polariton (HPP) waveguides consisting of a high refractive index semiconductor nanowire (ZnO, n = 2 at ~ 600 nm) separated by a controllable nanometer-thin, low-index dielectric gap (PMMA, n =1.49 at ~ 600 nm) from a flat silver substrate (Fig 3.1a). Key to this design is the placement of dye molecules (Oxazine 750 perchlorate, Sigma-Aldrich) inside the low-index gap consisting of a PMMA (A495) layer where the electric field of the hybrid plasmon mode is strongest (Fig. 3.1b). Tuning the optical confinement can be conveniently achieved by changing PMMA-to-solvent weight fraction of the PMMA/dye mixture. The solution was spun on a 300-nm-thick silver film with a quartz wafer as substrate. The obtained PMMA thickness was monitored by atomic-force-microscopy (AFM). This method reproducibly yields uniform dye-doped PMMA films with thickness in the range of 5 nm - 40 nm. In all of the samples, the fraction of dye in PMMA is kept constant at 0.06 wt%. In a final step, we complete the hybrid plasmon waveguide by spin-casting ZnO nanowires that were previously grown by vapor transport using the vapour-liquid-solid mechanism [55] and transferred into an ethanol solution via light sonication. A first evidence of efficient coupling of molecular emission into the guided mode is manifest in the epi-fluorescence image where emission from the molecules that were optically pumped at the middle of a waveguide propagated and then scattered at the two ends (Inset Fig.3.1a).

For the emitting dye molecules we chose a strong emitting molecule Oxazine (O1 perchlorate 750, Inset Fig 3.2a) which absorbs in the visible green spectrum and emits in the visible red (Fig.3.2a). To demonstrate strongly coupled dye molecule emission into the deep sub-wavelength guided HPP mode, we choose to utilize a time-resolved spontaneous emission spectroscopy (Fig.3.2c). We measured the spontaneous emission lifetime using time-correlated single photon counting (TCSPC system PicoQuant), where the dye molecules were excited by femtosecond laser pulses (Ti:Sapphire fs-pulse laser, λ = 620 nm, spot radius ~ 1 μm, fs-pulse length ~ 100 fs) focused to a spot of about 2 μm diameter onto the center of each waveguide (objective lens 63x, NA = 0.95). Spontaneous emission of the dyes was collected by the same objective, filtered within the spectrum bandwidth of 633 - 700 nm and registered by an avalanche photodiode. Note, the detector's (APD, MicroPhotonicDevices, PDM-series) dark count rate is one tenth of the photon collection rate from samples with dye molecules, thus no instrument response artefacts are expected in the single photon counting data. The dye emission at the detector of the setup is shown in Fig.3.2b, whereas the absorption was taken from Ref [56]. The emission is relatively broadband with a spectral width of about 70 nm (FWHM).

From the collected emission at the nanowire ends, time delayed histograms were build up using the delay between laser pulses and detected photons (Fig. 3.3). Spontaneous emission lifetimes were extracted by fitting the time response histogram to a bi-exponential lifetime model, which was sufficient to describe the spatial and dipole orientation heterogeneity between the optical mode and background dye emission.

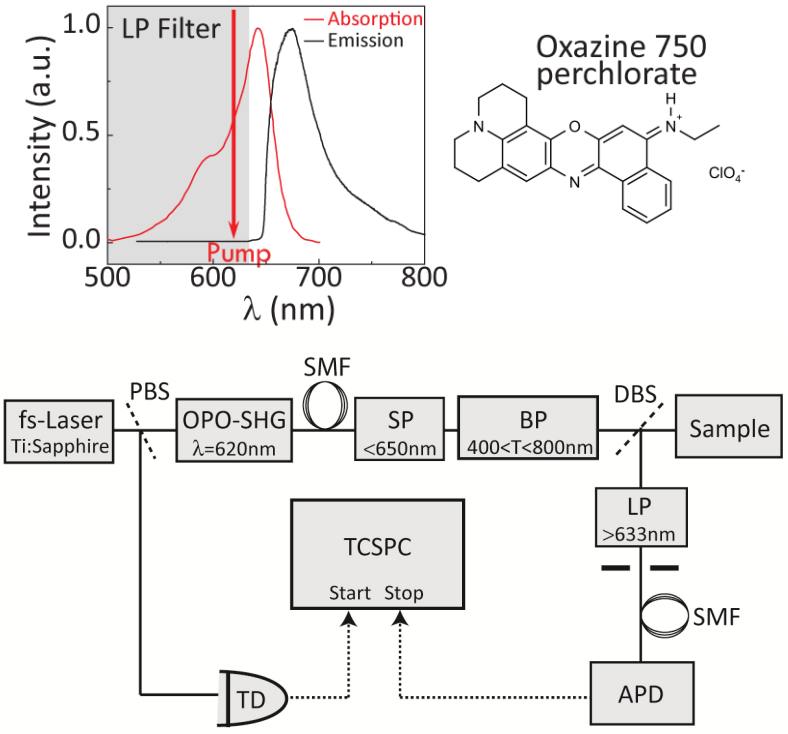

Figure 3.2. Experimental Setup (Top) Absorption spectrum of Oxazine 750 perchlorate dye molecule from Ref. [56] and measured broadband emission spectrum of the oxazine dyes in a waveguide (after LP 633 nm). Inset: molecular structure of the oxazine dye (Bottom) Schematic of the time-resolved microphotoluminescence setup--Ti:sapphire fs-pulse laser, pulse width ~ 100 fs), OPO: Optical Parametric Amplifier, SHG: second harmonic generation, TD: trigger diode, PBS: polarizing beam splitter, SMF: single mode fiber for spatial filtering, SP/BP/LP: shortpass/bandpass/longpass filters, DBS: dichroic beamsplitter (long pass edge at 625 nm).

To gain an insight into emission coupling to the different decay channels, we fabricated two other control samples: (i) dye-doped PMMA thin film (thickness g) on quartz substrate and (ii) dye-doped PMMA thin film of the same thickness g on Ag substrate (Ag 300 nm on quartz wafer). The first control sample (i) serves as the lifetime reference for the dye emission (τ_0 = 2 ns) (Fig 3.3a). This is in sharp contrast to dye emission resulting from the HPP mode yielding short lifetimes of 48±12 ps due to the sub-wavelength optical fields enhancing the emission rate (Fig.3.3b). The control (ii) shows shorter lifetime than control sample (i) because the PL decay rate is enhanced by metal quenching and emission into surface plasmon polariton on the metal film (Fig.3.3c). Yet, the control (ii) shows longer lifetime than HPP sample (Fig. 3.3b) due to the lack of HPP optical mode. Note that the PL decay histograms from both control cases (Fig. 3.3a,c) display single exponential decays implying that there is little dependence on the dipole orientation of the dye molecules. In all measurements, we also ensured that PL of the large-bandgap ZnO nanowire materials is negligible compared with emission of the dyes within our detected spectral bandwidth.

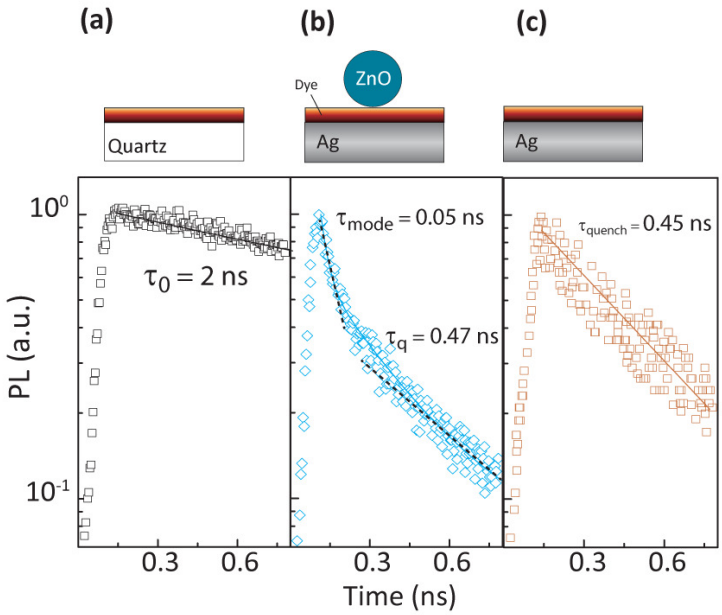

Figure 3.3. Sample structures with corresponding PL decay histograms. (a) First control sample (i) is reference oxazine:PMMA film on quartz (τ_0 = 2 ns). (b) HPP waveguide structure with g = 10 nm shows shorter lifetime component due to waveguide coupling and longer lifetime background due to uncoupled molecules (c) Second control sample (ii) shows shorter lifetime than control (i) due mostly to metal quenching at small distance less than 10 nm.

3.3. Scaling of deep sub-λ mode and Purcell enhancement

Figure 3.4 shows the results from Purcell effect calculation $F_P(g) = F_{mode}(g) + F_q(g) + F_{free} + F_{SPP} \approx F_{mode}(g) + F_q(g) + 4$, as a function of modal confinement or gap width g. We simulate the molecular emitter as a vertical dipole situated at the midgap of the HPP waveguide (Inset: nanowire diameter d_{NW} = 120 nm, at emission wavelength λ_{em} = 670 nm) to obtain the modal Purcell factor F_{mode} (green solid line in Fig 3.4.) from the eigenmode solution in Fig. 3.1b according to the formula.

$$F_{mode}(x_0, y_0) = \frac{3\lambda^2}{8\pi} \frac{c\varepsilon_0 \left|\vec{E}(x_0, y_0)\right|^2}{\int S_z \, dA} = \frac{3}{4\pi} \frac{c/n}{v_E} \frac{\lambda^2}{A_{eff}(x_0, y_0)} \qquad 3.1.$$

where we evaluate $\vec{E}(x_0, y_0)$ and $\int S_z(x, y) \, dA$ in (3.1) using the field from the eigenmode solution.

The quenching contribution F_q, and emission to single SPP, $F_{SPP} \approx 3$, on the other hand, can be estimated by an analytical method for planar structures according to Ref. [33], [34], described earlier in Chapter 2. F_{free} is the contribution of radiation to free space.

In addition, we performed a 3D full vector-field finite-element method (FEM) simulation in steady-state harmonic propagation formulation to confirm the validity of the analytical method (within less than 3% error for small electric dipole of finite size 2 nm), giving the quenching

contribution F_q (red dashed line in Fig 3.4) to the total decay rate enhancement F_P (black line in Fig 3.4) expected in real measurements. The quenching contribution is calculated with the help of a separate simulation where Ohmic loss in metal is neglected. Calculated total Purcell factor F_P in this lossless configuration yields purely radiative contribution $F_{rad} = \frac{P_{rad}}{P_0} = F_{mode} + F_{free} + F_{SPP}$ which we then subtract from the main simulation with Ohmic loss to obtain F_q (dashed line) in Figure 3.4.

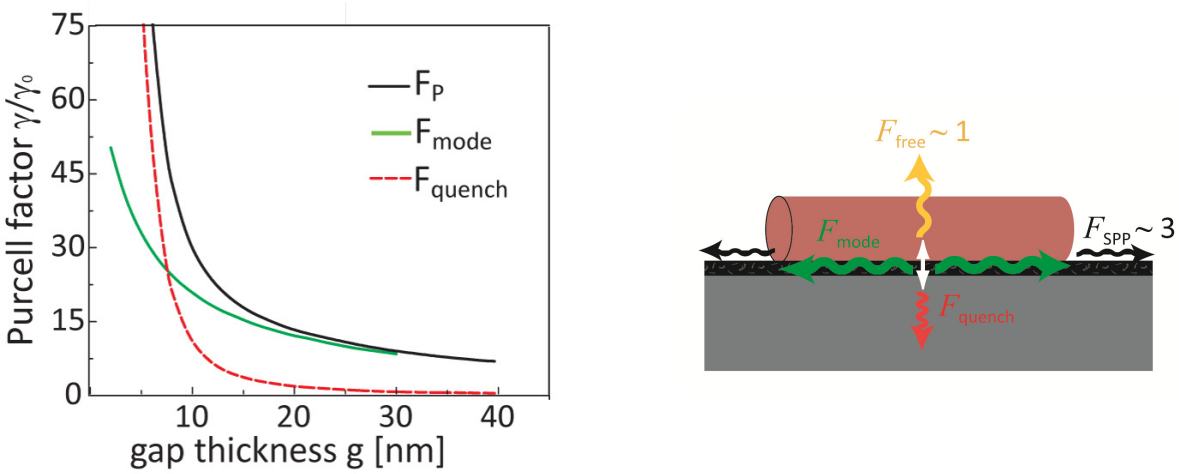

Figure 3.4. Calculation of Purcell effect inside the HPP waveguide. Calculated spontaneous decay rate enhancement due to propagating HPP mode (green line), metal quenching (red line), and total Purcell factor(black line). Purcell enhancement factor of the HPP mode increases as one improves optical confinement by shrinking the nanoscale gap of the waveguide. However, metal quenching similarly increases and becomes dominant for gap size below 7 nm. In the calculations, the emitting dipole (white vertical arrow) is positioned at midgap ($g/2$) and nanowire diameter, d_{NW} = 120 nm.
Inset: Arrows show different decay channels including emission into the HPP guided mode, free space emission, surface plasmon, and metal quenching. The white arrow indicates the position and vertical orientation of the molecular dipole emitter.

3.4. Extracting different contributions to spontaneous emission and the effect of dipole orientations

The measured PL decay rates when normalized to the reference sample (i) agree well with the predicted enhancement rates. Fig. 3.5a plots measured normalized decay rates for different gap sizes, each averaged over several waveguide samples. The error bars represent variation in measured values among samples of the same geometry. For a vertical dipole molecule, the modal Purcell factor F_m is significant for g < 25 nm and goes up as the gap width scales down. On the other hand, metal quenching F_q becomes strong and dominates over modal Purcell factor F_m when g is less than 10 nm. Horizontal dipoles on the other hand do not couple well to the hybrid plasmon mode due to the quasi-TM behaviour of the mode not aligning with the dipole orientation.

In an ensemble PL lifetime measurement, dye molecules which undergo faster decay and/or have higher fluorescence yield and extraction efficiency contribute more to the signal in the decay histogram. We attribute the appearance of bi-exponential decay in our data for HPP waveguide structure to the different decay rates of horizontal and vertical dipole due to their different coupling strength to the HPP waveguide. Besides, the slower decay component in the histogram partially comes from the molecules which are situated laterally away from the optical mode area, considering that our detectable volume is determined by a 1 $\boldsymbol{\mu m}$ diameter spot times the thickness of the PMMA layer g.

In the strong confinement regime (g < 20 nm), we achieve good light coupling from the vertical dipoles among the dye ensemble which can be extracted at the waveguide ends and thus raise the signal of the fast decay channel (enhanced by the modal Purcell factor) so that our data matches theory quite well for the very thin film samples. However, for lower confinement (g > 20 nm) regime, there is not enough difference in the Purcell factor between vertical and horizontal dipoles or the background molecules laterally away from the waveguide, such that within our detection volume, the molecules with small or no Purcell enhancement dominates the PL decay curve. We argue that the dominance of this background signal in the PL decay curve explains the slight discrepancy of our data from the vertical dipole calculation in the range $g > 20\ nm$. In addition, this background signal also leads to an increase in statistical variation in samples having smaller gap size (Fig. 3.5a) since the number of coupled molecules that overlap with the waveguide mode decreases with small gap size that variation among different samples of the same geometry is introduced according to Poisson statistics.

Unlike the HPP waveguide sample, the data from control (ii) (Fig.3. 5b) match the theory excellently since the measurement does not suffer from ensemble averaging due to lateral uniformity, and the weak dependence of emission rate on dipole orientations. Furthermore, it reveals information about metal quenching in comparison to the hybrid plasmon waveguide structure. In very thin dye-doped PMMA on silver, the overall fluorescence intensity drops dramatically due to metal quenching. Slight increase in statistical variation across several samples(error bar) at smaller gap size is attributed to smaller PL signal due to metal quenching.

We try removing background dye molecules that are not coupled to the waveguide, since their emission mask the signal from the HPP mode for large gaps. The origin of this masking-effect comes mainly from the size discrepancy between the collection area (~ 1 μm) and the nanowire diameter (~ 100 nm) and subsequent dye emission collection efficiencies. This is effectively done by deploying a mild oxygen plasma treatment removing the uncoupled dye molecules, where the nanowires themselves act as an etch mask (Fig. 3.6). Lifetime measurements of samples before and after etching showed single exponential decay histogram with τ_{before} = 1.0 ns and τ_{after} = 0.4 ns, respectively, e.g. for g = 20 nm. Eliminating the overshadowing background signal contribution for large g, we are able to recover the total Purcell factor which match the prediction better (gray square with dark edges in Fig.3.5a). In contrast, repeating the etch process step for small gap sizes still maintain a bi-exponential decay both before and after etching, showing the contributions of the vertical dipole and quenching. The reason behind these two different displays is the very strong Purcell factor at low gap sizes which confirms the proper operation of the HPP mode.

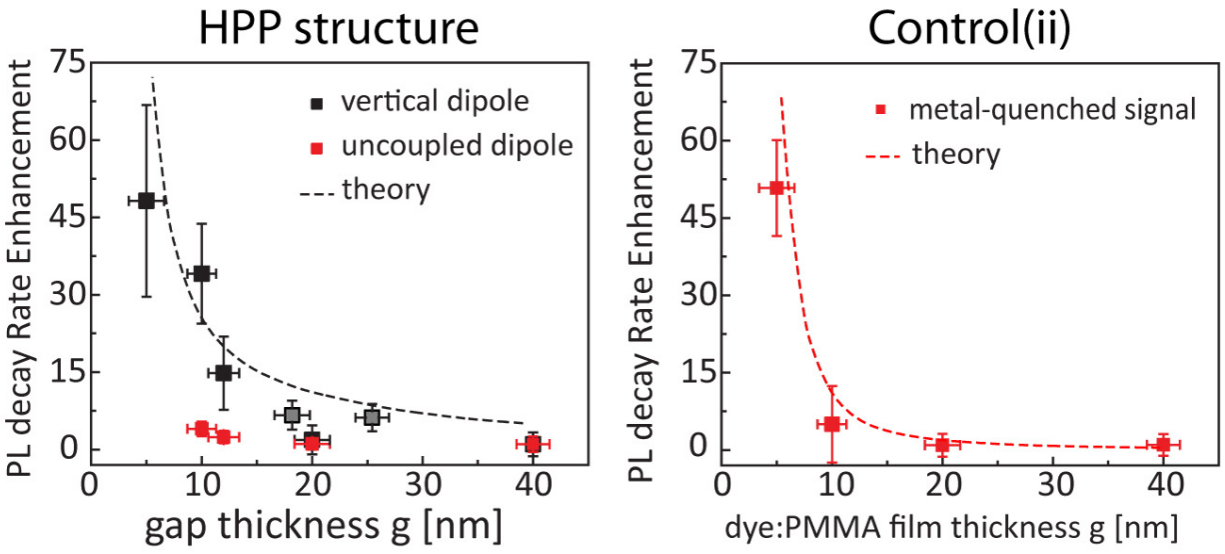

Figure 3.5. Measurements of different contributions to spontaneous decay
(Left) Averaged measured total spontaneous decay rate of dye molecules (filled black square) in HPP waveguides versus optical mode confinement g compared with theory of vertical dipole (black dashed). Error bars represent the range of measured values among several samples of the same geometry. Also shown is the measured decay rate of uncoupled molecules (red square). An average (highest) enhancement of 48 (65) is observed at g = 5 nm. The gray squares with dark edge represent HPP sample described in Figure 3.6.
(Right) The effect of non-radiative transfer (metal quenching) measured from the emission of dye molecules atop a flat silver film (control sample (ii)) was found to be significant at proximal distance g < 8 nm. Lateral uniformity and weak dependence on dipole orientations yields excellent agreement with theory (black dashed). Purcell factor of the background uncoupled dipoles measured on HPP structure in (a), also agree well with the value measured on control (ii) and from theory.

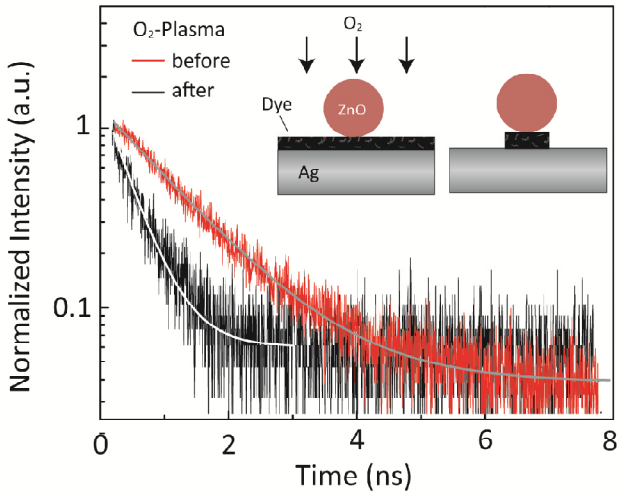

Figure 3.6. Selective removal of dye molecules not coupled to the HPP waveguide mode. For large g the theoretically predicted trend of F_P is recovered by reducing the

molecular background emission signal via O_2-plasma etching using the nanowire as a mask (shown as insets). The nanowire is used as a shadow mask to etch the dye layer via a mild O_2-plasma treatment (Inset). For large gap sizes, the decay histograms show a single exponential decay before and after etching, however, with long (short) lifetimes before (after) etching. The long lifetime response before etching stems from uncoupled molecular emission creating a background signal overshadowing the HPP mode channel.

Furthermore, we are interested in investigating where the emission ends up; a question that is guided by an analysis of the rate enhancement factor, F. While the enhancement factor for control (ii), $F_{(ii)}(g) = F_{free}(g) + F_{SPP}(g) + F_q(g)$, includes the contributions from emission into radiation waves F_{free}, surface plasmons F_{SPP}, and non-radiative quenching $F_q(g)$, the enhancement factor for the nanowire sample, $F_P(g)$, also additionally includes the contribution of the waveguide mode, i.e. $F_{mode}(g) \approx F_P(g) - F_{(ii)}(g)$. This provides an estimate of the waveguide mode coupling factor, $\beta(g) \approx 1 - F_{(ii)}(g)/F_P(g)$ (Fig.3.7), suggesting that emission into the hybrid plasmon mode dominates over all the other emission channels for a large range gap sizes, g with β-factors as high as 85%. However, for gaps smaller than about 5 nm, non-radiative quenching starts to dominate over emission into the waveguide mode (red squares) and the β-factor approaches zero (Fig.3.7). Note that horizontal dipole components display no modal Purcell effect ($F_{mode} < 1$) anywhere underneath the waveguide and as a result their decay is dominated by non-radiative quenching at small gap such that their mode coupling factor and intensity is nearly undetectable, thereby allowing us to distinguish clearly the coupling effect on vertical dipoles.

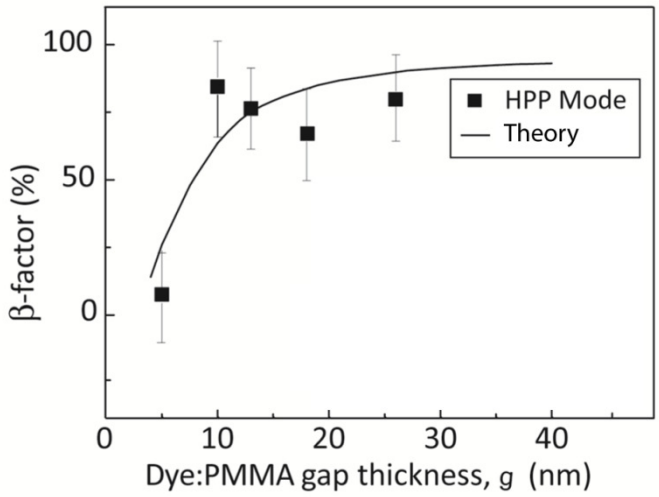

Figure 3.7. Mode coupling factor. The β-factor of the waveguide mode increases with gap thickness, g, over the range shown and dominates other emission channels for g > 8 nm.

3.5. Photon flux enhancement

In addition to the enhancement of the spontaneous emission lifetime, the PL brightness, or photon flux, at the detector is important from a practical device consideration, e.g. light emitting or detecting device [36], [57]. We benchmarked the total photon flux from the HPP waveguide design (pump on nanowire) against a pure plasmonic case (pump on metal = control-ii). By varying the gap thickness we observed a 5-fold PL enhancement around g = 10 nm (Fig.3.8b). This enhancement ratio of PL extraction is related to the product of the spontaneous emission rate enhancement F_P and the spontaneous emission factor β of the deep sub-wavelength waveguide mode. Measured PL enhancement appears to peak near g = 10 nm.

To further clarify the effect of quenching in the plasmonic waveguide, we model the fluorescence rate $\gamma_{em} = \gamma_{exc}\eta = \gamma_{exc}.\beta\, e^{-2\,Im(k_z)L}\,\eta_{edge}$ as depending on the excitation rate γ_{exc} and photon extraction efficiency η. When compared to molecules atop a flat metal film, the fluorescence enhancement arises from strong coupling to the waveguide mode alone and not from local field enhancement in excitation, since the polarization of the hybrid plasmon mode, which is in the propagation direction of the incident field, is always perpendicular to the polarization of the incident field. With negligible excitation enhancement, the fluorescence intensity of a dye molecule in the HPP waveguide is proportional to the photon extraction efficiency η which depends on the coupling efficiency (β-factor) into the waveguide mode $\beta = F_{mode}/F_P$, propagation efficiency along the waveguide $e^{-2\,Im(k_z)L}$, where L is the distance from pumping position of the dyes to the nanowire ends, and the scattering efficiency η_{edge} at the extremities of the waveguide into free space modes, that can be collected by the objective lens. Assuming same edge scattering efficiency η_{edge} for all waveguides with similar nanowire diameter, the photon extraction efficiency by the waveguide $\eta_{wg} = \beta e^{-2Im(k_z)L}$ depends largely on mode coupling factor and propagation loss of the mode. Note, that even though it is known that emitters with low intrinsic quantum efficiency can have large intensity enhancement by the use of lossy optical antenna [51], [52], we consider in our experiment only the radiative efficiency of the waveguide itself, assuming near-ideal intrinsic quantum efficiency of the dye molecules, which is realistic for laser dye such as oxazine. From theory and the PL lifetime data, we can empirically describe the Purcell factor of the optical mode as increasing monotonically with the reduction of gap width g as a power law $F_{mode} \sim g^{-0.7}$. However, the Purcell factor for the quenching F_q follows $F_q \sim g^{-3}$ [34], so that the mode coupling fraction for the HPP waveguide is larger than that of the flat metal surface, where only free space coupling contributes to the fluorescence intensity of the dyes (Fig. 3.8a). Combining this estimate with rather small propagation loss along the waveguide (a realistic nominal value of $L = 5\,\mu m$), we therefore expect a fluorescence intensity enhancement in a waveguide configuration to scale up with modal confinement g compared to that of a quenched thin film of dyes on metal surface (projected with the black solid line in Fig. 3.8b.). However, we observe the fluorescence enhancement to reach a maximum of about 4-5 times around $g \sim 10\,nm$ and drop to around twice at $g \sim 5\,nm$. This result implies a competing fluorescence quenching mechanism for $g < 10\,nm$.

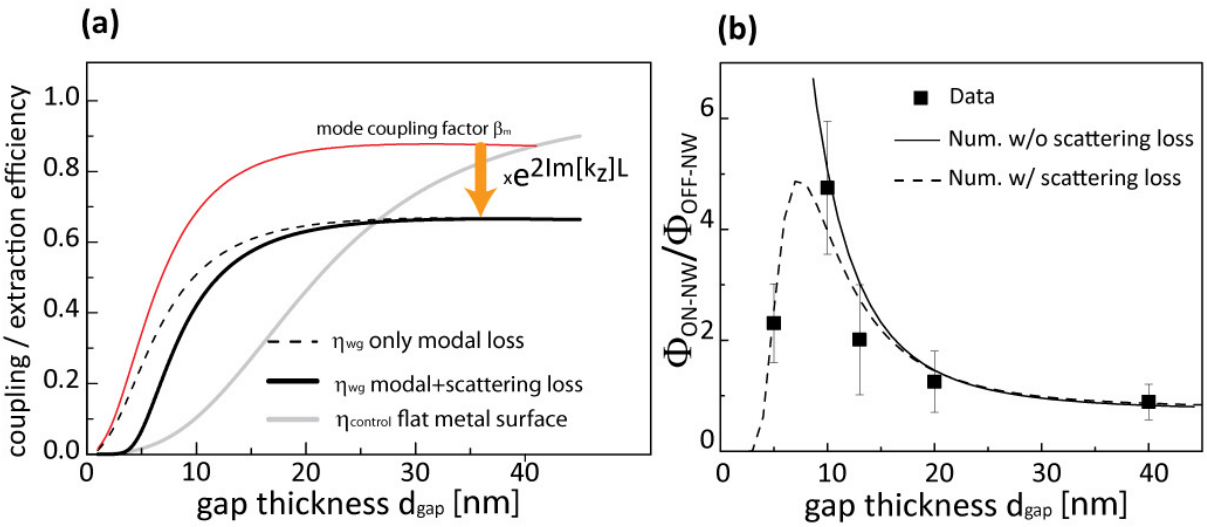

Figure 3.8. Fluorescence intensity enhancement (a) Estimates of photon extraction efficiency by the waveguide η_{wg} from mode coupling factor β (red solid) and propagation efficiency $e^{-2Im[k_z]L}$ (black dashed) show improvement over flat silver surface $\eta_{control}$ (grey solid). ($L = 5\ \mu m$ was assumed.) In addition, strong reduction in extraction efficiency at small g is modeled by enhanced scattering loss into non-radiative channel in metal (black solid line) in order to reproduce measured intensity data in (b). (b) Measured relative enhancement in fluorescence intensity (black square) $\Phi_{ON-NW}/\Phi_{OFF-NW} = \frac{\eta_{wg}}{\eta_{control}}$ comparing photon flux from HPP mode vs. control-(ii) showing the successful competition of the nanoscale mode over other emission channels resulting in an average of 5-fold increase in intensity. A propagation efficiency model which includes Purcell-enhanced scattering and absorption in metal (dashed line) describes our data better than the pure modal loss model (black line) due to its strong dependence on g.

Two possibilities for strong quenching at small g are i) a tradeoff between propagation length with optical mode reduction leading to lower collection efficiency at the scattering ends of the waveguide ii) large sensitivity to surface roughness scattering when the optical mode is extremely small. To test the first hypothesis, we compare our simulation for the propagation with the data and found that the dependence of the propagation loss $2Im(k_m)$ of the guided mode (with modal wavevector k_m) on g is not strong enough to significantly reduce the collection efficiency at the ends of waveguide for the range of measured nanowire lengths.(dashed line in Fig. 3.8a) Even when assuming larger loss value for the waveguide mode, the weak dependence of propagation length on the gap width is unable to reproduce the quenching effect at small gap g < 10 nm (solid line in Fig.3.8b). On the other hand, if we follow the second hypothesis, we may assume that a sub-wavelength roughness defect in the waveguide acts as a dipole scatterer which can either scatter guided light into forward or backward propagating modes and free space or transfer energy non-radiatively to metal (quenching) [58]. The intensity loss channels are then metal quenching and amplified propagation loss due to multiple scattering inside the waveguide which lengthens the effective optical path and thus absorption in the metal. We employ a simple power law model for the quenching loss channel (solid line in Figure 3.8a) by the same scaling

law as F_q i.e. using a fitting function $\frac{Im(k_{z,scattering})}{k_0} = \sigma\left(\frac{10\ nm}{g\ [in\ nm]}\right)^3$ such that $Im[k_z] = Im[k_m] + Im[k_{z,scattering}]$. This model reproduces the trend in the fluorescence intensity data (dashed line in Fig.3.8b) with a single fitting parameter (σ = 0.004) representing the scattering cross section and density of scattering defects. We argue that at small gap size ~ 5 nm, a single dipole scattering event is dominated, in similar way to dipole emission coupling, by non-radiative transfer to the metal such that propagation effect such as multiple scattering is much less significant.

3.6. Conclusions and Outlook

To summarize, the decay rate enhancement and fluorescence intensity enhancement of dye molecules which samples the mode area in the gap region of a hybrid plasmon waveguide are measured quantitatively. The results agree well with theory. This experiment shows that almost 75% of the molecular emission can be coupled to an optical waveguide with deep sub-wavelength confinement. In addition, the metal quenching contribution in the PL decay data are verified by comparing with theory and fluorescence intensity data. Furthermore, we find a brightness enhancement up to 6-fold for an optimum gap height of about 10 nm, implying that good photon extraction efficiency can be achieved due to low propagation loss over at least 5 μm along the length of the waveguide. These results are important for the understanding and control of emission coupling into nano-plasmonic waveguide structures which may be useful for improving on-chip molecular sensing and spectroscopy, LED, single photon source and quantum information processing.

Chapter 4
Squeezed Photonic Waveguide: single emitter in a deep sub-wavelength all-dielectric waveguide

Strong and controllable light-matter interactions at the single emitter-photon level are of fundamental importance for quantum information science, which leads to important applications such as quantum memories, switches and gates [19], [32], [38–41], long range coupling of single emitters and novel entanglement schemes [20], [42]. Plasmonic nano-structures have been recently introduced to improve emission directivity and coupling to and from free space by reducing optical mode sizes, circumventing the speed and bandwidth limitation of high quality factor resonators [59], [60]. Nevertheless, localization of individual quantum emitters in nanometric-scale region of low-permittivity, while at the same time trying to avoiding metal-intrinsic absorption, quenching and propagation loss in the metal remain a technical challenge in observing strong interaction and significant emission enhancement. Despite tremendous progress made in plasmonics, practical realization of on-chip optical devices with single emitters for quantum information processing requires, in addition to strong confinement, lower intrinsic loss, higher coupling efficiency, and upward scalability to long-range optical interactions of multiple emitters. Alternative approaches to plasmonics has been suggested in Ref. [32], [49], [61–63] using purely high-index contrast between dielectric interfaces to overcome the diffraction limit.

We describe in this chapter an experiment on strong optical interactions at single photon and single emitter level using an all-dielectric nanoscale waveguide that allows a deep sub-wavelength field confinement down to $\lambda^2/50$. The method for observing strong interaction and large Purcell enhancement in this work is achieved by placing single quantum dots in its optimal environment with the help of atomic force microscope(AFM) manipulation, facilitated by implementation of a particular waveguide design, called here squeezed photonic waveguide. Drastically enhanced interaction between the quantum emitters and the localized fields suppresses blinking of the quantum dots and substantially increase the emission rate dynamics of the quantum emitter by a 31 times. The very large coupling factor redirects up to 80% of emission from an individual emitter into a waveguide mode and single photon emission is observed with high fidelity and at much reduced emission saturation.

4.1. Design of deep sub-wavelength all-dielectric waveguide: from all-dielectric coupled-nanowire waveguide to squeezed photonic waveguide

Approaches using high-index contrast between dielectric interfaces to overcome the diffraction limit has been suggested in an all-dielectric coupled silicon waveguides [32], [49], [61], [62] and

telecom wavelength light concentration at 100 nm scale was demonstrated [59] in this dielectric structure. However, incorporating single quantum emitters into such a waveguide while squeezing the active region, in order to achieve strong interaction regime, remains a challenge [61], [64].

Figure 4.1 shows several all-dielectric slot waveguide designs for Purcell enhancement. The all-dielectric waveguide design employed in this experimental work consists of a high-refractive index dielectric nanowire separated from another infinite high-index dielectric slab by a nanometric scale gap. As the quasi-TM (transverse magnetic) guided mode (photonic mode) of the nanowire hybridizes with the dielectric slab, the electric energy is squeezed in the small gap region due to the large discontinuity in permittivity. We call the optical mode concentrated electric field in the nanometer scale gap region along the nanowire in this architecture a squeezed photonic mode.

As shown in Figure 4.1, the squeezed photonic waveguide has the largest mode index but a trade-off of modal Purcell factor in comparison to other related dielectric slot waveguides, as a result of the infinite slab that supports a larger angular spread of in-plane wave-vectors. The squeezed photonic waveguide, however, has a significant practical advantage--it requires no alignment of the nanowire to the bottom structure so that a highly-confined guided mode can be formed by placing a nanowire simply anywhere on the substrate. This advantage is extremely useful in coupling the nanowire on and off the position of a single emitter that sits on the slab. Moreover, the geometry implies a practical way of integrating multiple emitters on the same bus waveguide to realize a network architecture.

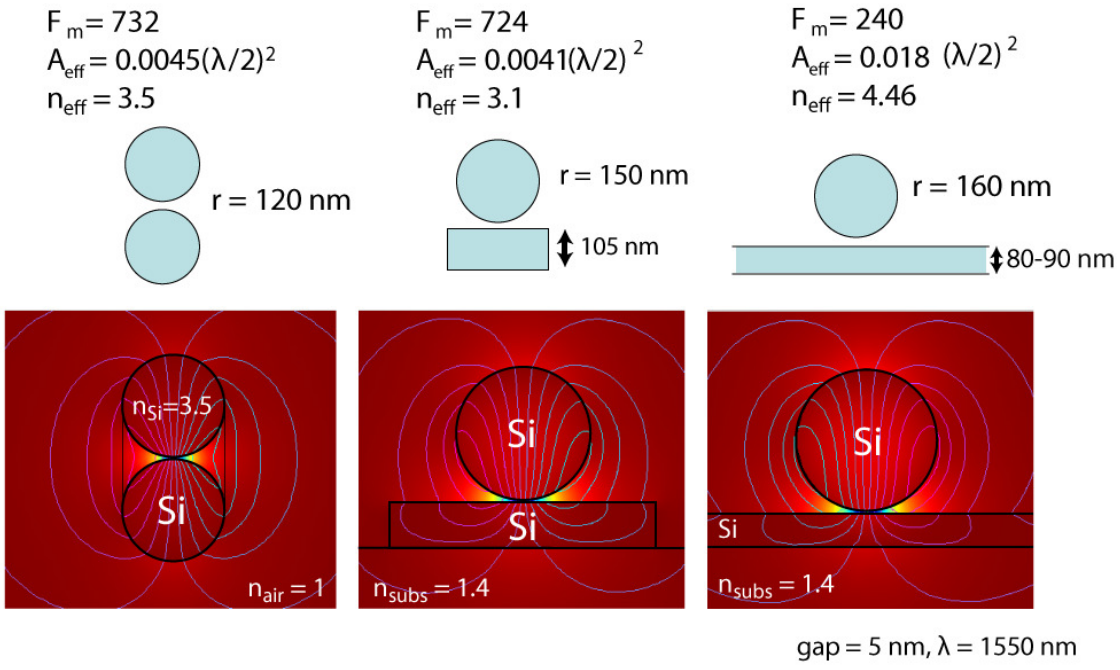

Figure 4.1. Comparing all-dielectric sub-λ slot waveguide designs for Purcell enhancement. (a) coupled nanowires waveguide (b) nanowire-strip slot waveguide and (c) nanowire- slab slot waveguide or squeezed photonic waveguide. The density plot

shows |*E*|-field mode profile of optimized geometry for electric field confinement. The corresponding modal Purcell factor, effective mode volume, and effective index of the mode are shown. The gap is assumed to be 5 nm and emission wavelength $\lambda = 1550$ nm. The squeezed photonic waveguide, which we focus on in the experiment described in this chapter, consists of a high permittivity dielectric nanowire separated from another infinite high-permittivity dielectric slab by a nanometric scale gap. As the quasi-TM (transverse magnetic) guided mode (photonic mode) of the nanowire hybridizes with the dielectric slab, the electric energy is squeezed in the small gap region. Compared to other related dielectric slot waveguide structures, the squeezed photonic waveguide has the largest mode index but a trade-off of Purcell factor, as a result of infinite slab structure which supports a larger spread of in-plane wave-vectors. The squeezed photonic waveguide, however, has a significant practical advantage--it requires no alignment of the nanowire to the bottom structure so a highly-confined guided mode can be formed by placing a nanowire anywhere on the substrate. This advantage is extremely useful in coupling the nanowire on and off the position of a single emitter that sits on the slab. Moreover, the geometry implies a practical way of integrating multiple emitters on the same bus waveguide to realize a network architecture.

Another practical advantage of an all-dielectric waveguide over hybrid plasmonic waveguide from Chapter 3 is its dual accessibility due to excellent optical transmission of the sample. High photon collection efficiency can be achieved by imaging the structure from the substrate side using oil immersion objectives, meanwhile mechanical manipulation with AFM from the top side and also be imaged simultaneously. In other words, the squeezed photonic waveguide platform offers a practical design for aligning the optical mode to the position of the single emitters.

Visualization of the all-dielectric nano-QED system that consists of the nanowire-slab waveguide and a single QD strongly coupled to the waveguide mode is shown in Figure 5.2 (Top Panel). In the experiment, the dielectric waveguide is formed by a high-index Si nanowire (refractive index $n = 3.7120 + 0.0085i$, 260-280 nm in diameter) on top of a 90 nm ZnS film (refractive index of 2.3). Colloidal CdSe/ZnS core-shell QDs (800 nm peak emission) are spin-coated on the sample to form a disperse monolayer prior to nanowire transfer. The AFM is used for selection and positioning of the nanowires such that a QD is precisely placed right underneath the nanowire. Given the physical size of ~ 8 nm of the QDs along with ZnS surface roughness of 1 nm (FWHM), one creates a nanometer-sized air gap between the nanowires and the ZnS film (inset of Fig. 4.1a). Such a narrow nano-scale air gap region along the nanowire supports a deeply confined one-dimensional guided mode, which we call squeezed photonic mode.

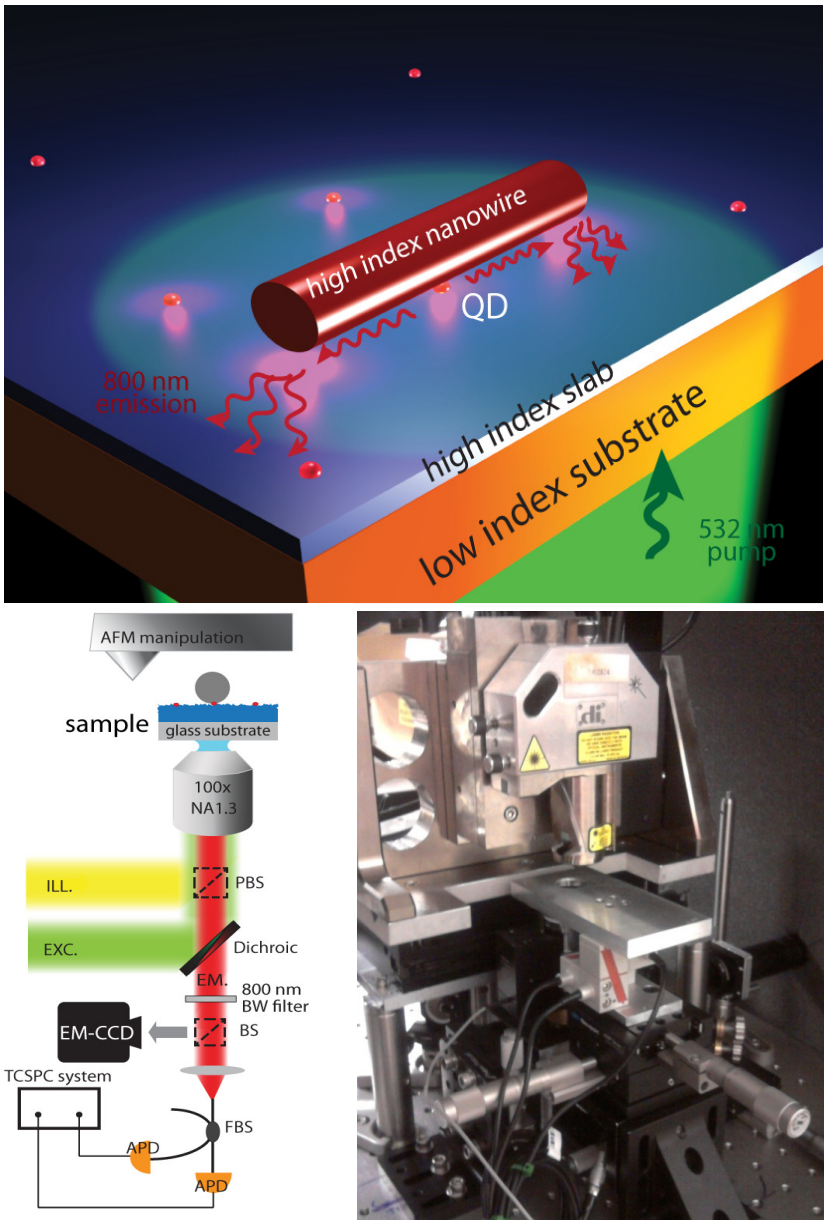

Figure 4.2. Experimental system (Top panel) Visualization of the coupled emitter-waveguide system. The QDs (red particles) are excited by a 532 nm continuous wave (*cw*) laser illuminated over a large area from the substrate side below the waveguide system. The waveguide and the QD are assembled by an AFM manipulator from the top. When the QD is placed at the position of optimal interaction with the waveguide, its emission scatters directionally into the waveguide mode and propagates along the waveguide before it scatters out at the ends, indicating the strong interaction between the confined mode and the emitter. the nanowire is repeatedly repositioned until spatially-optimal coupling is observed. (Bottom panel) Schematics of the experimental setup in which the atomic force microscope(AFM) is integrated with the fluorescence imaging and single photon counting systems. ILL. = illumination path, EXC. = excitation path, EM. = emission collection patch, PBS = polarizing beam splitter, BS = non-polarizing beam splitter. EM-CCD = CDD camera for imaging, TCSPC = Time-correlated single-

photon-counting system, APD= avalanched photodiode, FBS = fiber beam splitter. Dashed line on the beam splitters indicate flipping mount. QD emission is filtered and focused into a single mode fiber which in turn spatially images a small diffraction-limited spot on the sample onto the photon counters.

4.2. Experimental procedure

The experimental setup consists of the fluorescence imaging and single photon counting systems with an integrated AFM, as shown in Fig 4.2(Bottom Panel),which allows precision control over the position of individual QDs and nanowires, a major practical advantage over conventional lithographic approaches with limited lateral resolution. The AFM is used for selection and positioning of the nanowires such that a QD is precisely placed inside the squeezed photonic mode. However, the dipole orientation of the colloidal QDs is still random which may cause the coupling efficiency to be reduced from the optimal configuration. The QDs are excited from the substrate side using a 532 nm continuous wave laser and an oil immersion objective (Zeiss, EC Plan-Neofluar 100x/1.3 NA). Fluorescence is collected in reflection through the same objective and imaged on a CCD camera (Hamamatsu EM-CCD, C9100) and white light imaging is used to locate nearby Si nanowires. Next, the dimension of a selected nanowire is measured by scanning the AFM tip in tapping mode, and then in contact mode the nanowire is repositioned on top of the desired QD. When the QD is placed in the region of large field enhancement, its emission scatters directionally into the waveguide mode and propagates along the nanowire before it scatters out at the ends of the waveguide. The coupling is first imaged on the CCD camera, where glowing at the ends of the nanowire shows a first sign of coupling. If necessary, the nanowire is repeatedly repositioned until spatially-optimal coupling is observed. When strong emission coupling from the QD to the nanowire is observed, we locally measure intensity auto-correlations using SPCMs (Perkin Elmer APQ14-FC).

CdSe/ ZnS core/shell carboxylated QDs with a polymer coating (Invitrogen, Qdot 800 ITK) are spin-coated on sample substrates to a concentration of ~ 3 particles per 10 μm^2 allowing for well-isolated QDs to be studied. A 5 nm MgF_2 wetting layer is deposited on a plasma-cleaned glass cover slip, followed by electron beam evaporation of 90 nm of ZnS thin film (*Edward EB3*). Deposition of the ZnS slab layer are characterized by an AFM (Veeco Dimension 3000) to ensure uniform thickness across the sample and minimal peak-to-valley surface roughness of ~6.6 nm. Finally, Si nanowires with diameter in the range of 260-280 nm are drop-cast on the sample. Preparation of Si nanowires is described in Appendix B. Given the physical size of ~ 8 nm of the QDs along with ZnS surface roughness, one creates a nanometer-sized air gap between the nanowires and the ZnS film (inset of Fig. 4.4a) where the field of the squeezed photonic mode is concentrated.

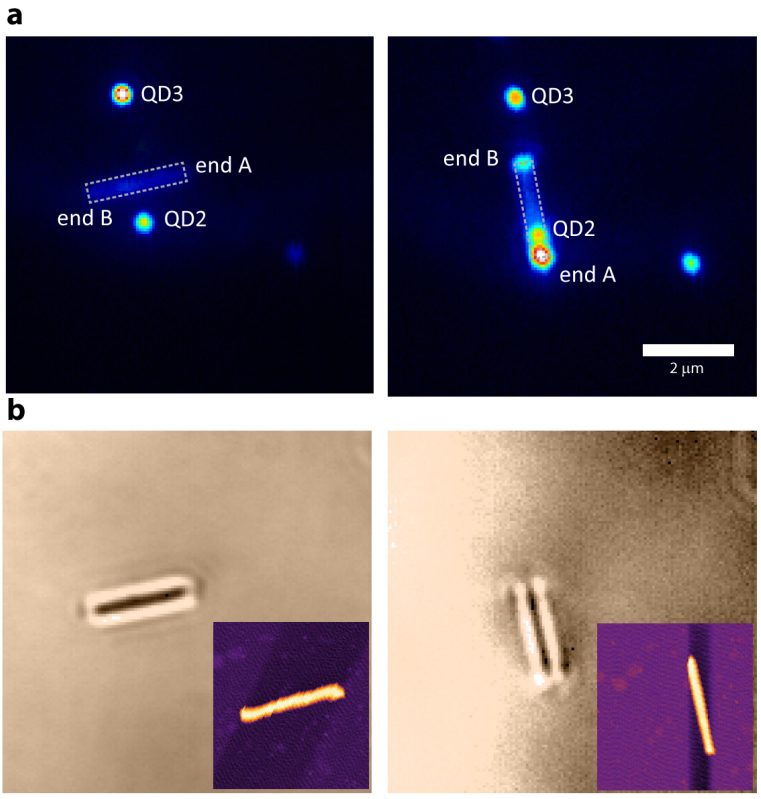

:

Figure 4.3. Images of experimental procedure whereby white-light illumination optical images (b) combined with corresponding fluorescence images (a) are used to locate the nanowire and quantum dots in the field of view. An AFM tip is used to move the nanowire to different positions as shown in left (uncoupled) and right panel (coupled). Insets: corresponding AFM scanned images.

4.3. Purcell-enhanced optical interaction in the coupled QD-waveguide system

Fig. 4.4b shows the fluorescence image of a single QD that is strongly coupled to the waveguide averaged over 200 s duration. The quantum dot (QD1) is placed underneath the nanowire and the bright glowing ends of the waveguide signify the strong interaction. The intensity time traces from the two ends and from the QD position reveals fluorescence blinking that is characteristic to a colloidal QD, as shown in Fig. 4.4c. The blinking signal in these three traces (shaded) are simultaneous (with correlation values higher than 0.9), indicating that the light scattered out at the ends of the waveguide is coming from the same coupled quantum dot (QD1). For comparison, any isolated QD nearby blinks independently (correlation < 0.1) from one another and from the coupled QD1.

Strong interaction of the QD with the squeezed photonic mode is evident as the emission from each end of the nanowire is about twice as strong as that at the position of QD1. The ratio of the fluorescence signals from the two ends of the nanowire to the sum of all the three spots yields an

apparent emission coupling factor of about 80 %, in good agreement with theoretical prediction of 82% for a Si nanowire on ZnS slab structure (see Fig. 4.6b) and outperform previously reported plasmonic waveguides [65–67]. In the mean time, as shown in the final trace (not shaded) in Fig. 4.4c, the strong confinement at the nanoscale significantly enhances the total photon flux and more than 4 times more photon are collected from the strongly coupled QD1 than that of the uncoupled scenario. Moreover, the deep sub-wavelength confinement is strong enough to achieve near unity [36], [68–72] emission coupling factor despite the fact that the colloidal quantum dots are two-dimensional isotropic emitters with random orientation of its crystalline axis [73].

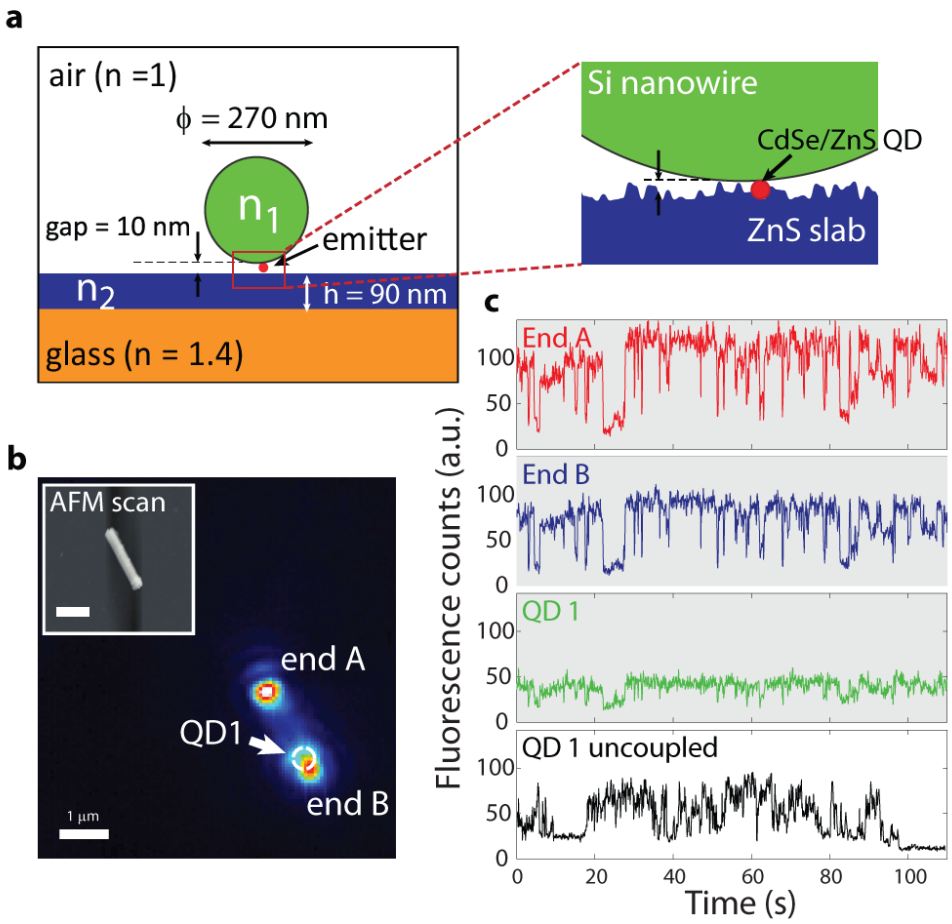

Figure 4.4. The deep sub-wavelength all-dielectric QED system with a nanoscale gap. (a) The dielectric nano-QED system consists of the nanowire-slab waveguide and a single quantum emitter strongly coupled to the waveguide mode. The waveguide is formed by a high index (n_1) nanowire, an air gap region and a high index (n_2) slab on a glass substrate. Light is confined in the gap region due to the high index contrast for optical modes with dominant electric field components normal to the interfaces. Insets: A zoom-in experimental schematic (drawn to scale) of the air gap (~ 8-10 nm) formed by top surface roughness of a ZnS slab (thickness = 90 nm) with a CdSe/ZnS QD between the slab-air interface and a Si nanowire (diameter = 270 nm). (b) The averaged fluorescence image of a single QD coupled to a nanowire-slab waveguide. The inset shows the AFM scan image of the nanowire. (c) Fluorescence time traces detected at the two ends of the nanowire

and at position of the coupled QD (QD1) on the same time axis (shaded). Simultaneous blinking of the ends of nanowire and coupled QD1 indicates that light from the three spots comes from the same coupled QD (QD1). The strong emission from the ends of the nanowire indicates the strong interaction of quantum dot and the squeezed photonic waveguide mode. Time trace of the same QD1 when uncoupled at a different time is included (unshaded) for comparison.

4.4. Study of single emitter dynamics

Characterization of a single photon source using intensity auto-correlation

In order to verify that the emission originates from a single QD emitter, we perform two-photon intensity autocorrelation measurements [74]. When illuminated by a continuous wave laser, the emission from a single quantum dot is split into two channels through a fiber beam-splitter and then detected by two identical avalanche photodiodes where we record time delay between a two successive photon events across the detectors to generate an intensity autocorrelation signal $g^{(2)}(t) = \langle I(t')I(t'-t)\rangle$. Since a single photon source does not emit two photons at the same time, we observe a dip in the two-photon coincidence at zero time delay. Fig 2b shows normalized two-photon intensity correlation $g^{(2)}(\tau)$ of the quantum dot QD2 for both coupled and uncoupled cases. When the emission of the QD is strongly coupled to the waveguide mode, as shown in Fig. 4.5c, the autocorrelations show identical narrow dips measured at the QD position (red curve) and nanowire end (green curve). When uncoupled from the nanowire, a wider dip is measured from the same QD (blue curve). In all three cases $g^{(2)}(0) < 0.5$ verifies that the emission is indeed from a single QD and its single photon state purity is excellently preserved after coupling. Slightly higher value of $g^{(2)}(0)$ for the coupled case is due to spurious uncorrelated fluorescence from the nanowire.

Using this anti-bunching feature of the signal, the rise time τ of the emitter can be extracted with a fitting function $g^{(2)}(t) = (1-\exp(-|t|/\tau))+d)$. Here fitting parameter d accounts for the background noise. The measured rise time τ depends on the excitation intensity, I, according to the relation $1/\tau = k_{12} + k_{21}$, where k_{12} is the intrinsic decay rate and $k_{21} = \alpha I$ is the excitation rate. Here, α is a proportionality constant that depends on the coupling strength to the excitation field [74]. To extract the intrinsic decay rate, the second-order correlation signal were measured at various excitation intensities, and the rate, $1/\tau$, is shown as a function of excitation power $P = I*area$ as in Fig 4.5d. We found intrinsic lifetime by extrapolating a linear fit of the data to zero power.

Measurements of emission lifetime

Since the emission lifetime varies among different QDs, measurements on the same QD before and after coupling provides unambiguous determination of the Purcell enhancement factor. The pulsed excitation measurements reveal a multi-exponential decay curve, characteristic of colloidal QDs (Fig 4.5b), with a longer time constant corresponding to the radiative

recombination lifetime of the bright state [75]. The inset shows the fluorescence image of the strongly coupled QD that is studied here. A long lifetime of about 120-180 ns is typically observed for uncoupled CdSe/ZnS QDs [76]. Extracted from Fig. 2a, the recombination lifetimes are 5.4±0.1 ns for the coupled and 170±2 ns for the uncoupled QD, resulting in a strong Purcell enhancement factor of 31 due to the strong field confinement in the squeezed photonic mode, much greater than observed in plasmonic waveguides and nanoparticles [65–67], [77], [78].

Intrinsic decay rate obtained by extrapolating rise time in the anti-bunching dip

The width of the anti-bunching dip in intensity autocorrelations (Fig. 4.5c) is determined by the overall emission rates — the sum of the intrinsic decay rate and the excitation rate, the latter of which is proportional to the pump power. As shown in Fig. 4.5d, extrapolation of the measured emission rates to zero pump power yields the intrinsic lifetimes of about 5.2±0.4 ns and 160±22 ns for the coupled and uncoupled cases, in good agreement with the values of the lifetimes directly measured under pulsed excitation. Importantly, as shown in the inset of Fig. 4.5d, we observe that strong Purcell enhancement tremendously reduces the saturation of the QD bright state emission which is favorable for implementation of high brightness single photon sources.

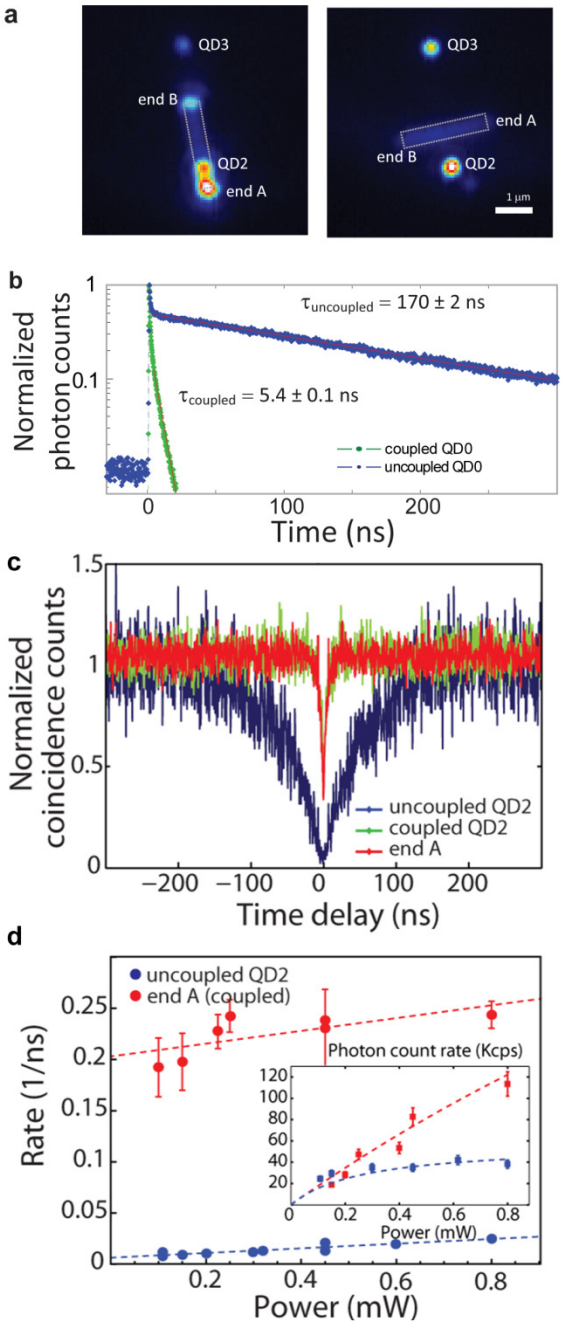

Figure 4.5. Purcell emission enhancement of a single QD strongly interacting with the squeezed photonic mode. (a) Direct lifetime measurements of another QD-nanowire system (Inset) under pulsed laser excitation shows drastic 31-fold difference from the same QD2 decoupled from the nanowire. Extracted recombination lifetimes are equal to 5.4±0.1 ns for the coupled and 170±2 ns for the uncoupled QD. (b) Two photon intensity autocorrelation measurements (at pump power 0.45 mW) show anti-bunching dips confirming single photon emission from the individual quantum emitter. A striking difference in the width of the dip is observed between the coupled and uncoupled QD, showing a strongly reduced recombination lifetime of the coupled QD. (c) A plot of photon de-excitation rate, which is reciprocal to the width of the anti-bunching dip,

corresponds to the sum of the intrinsic decay rate and the excitation rate and is linearly dependent on the pump power. Extrapolation to zero pump value yields the intrinsic lifetime of about 5.2± 0.4 ns and 160±22 ns respectively for the coupled and uncoupled cases, in good agreement with the lifetime directly measured under pulsed excitation.

Suppression of intensity saturation in the coupled quantum dot-waveguide system

We observe that strong emission enhancement tremendously reduces the saturation of the quantum dot bright state emission. The inset of Fig. 4.5d shows intensity saturation curves for coupled and uncoupled quantum dot. According to two-level model, the overall emission rate from the quantum dot under cw excitation is is $\gamma * k_{12} /(k_{12}+ k_{21}) Q$, where γ is the emission out-coupling efficiency into the single mode fiber, Q is the quantum efficiency of the emitter $Q = k_r / k_{21,}$ k_r is the radiative emission rate, k_{nr} is non-radiative component of the total rate ($k_{21} = k_{nr} + k_r$) from the upper state. We define the saturation factor as $S_F=k_{21} /(k_{12}+ k_{21})$, The intensity saturation occurs if the excitation rate is higher than the spontaneous emission rate $k_{12} > k_{21}$ (S_F <1), which occurs under typical excitation conditions for uncoupled QDs. However, when QD is coupled to the nanowire, the radiative decay rate k_r is significantly enhanced. As a result, the intensity curve shows almost linear dependence on the pump power, indicating the absence of saturation ($k_{12} < k_{21}$, S_F ≈1). For example, under the excitation power of 45mW, the saturation factors for the coupled and uncoupled QD are equal to 0.95 and 0.35 respectively.

Indirectly, the saturation suppression is implied from the autocorrelation measurements: the relative slope steepness of the rate ($k_{12} + k_{21}$) in Fig. 4.5d indicates the degree of the intensity saturation of the quantum dot. Relatively flat curve ($k_{12} < k_{21}$) for the coupled QD indicates that the saturation is tremendously suppressed due to strong enhancement of spontaneous emission rate.

4.5. Correspondence with theory of Purcell enhancement

Both lifetime measurements with pulsed excitation and intensity autocorrelation measurement under *cw* excitation reveal a striking difference in the recombination lifetimes measured for the coupled and uncoupled QD. Unambiguous measurements of the Purcell factor of value 31, performed on the same QDs before and after interacting with the squeezed photonic mode quantitatively confirm the dramatic optical confinement in this all-dielectric waveguide QED system. Theoretical calculation in Fig. 4.6a shows how the electric field of the squeezed photonic mode — particularly the normal component to the slab — is highly concentrated in the gap region with a lateral confinement (FWHM) of 75 nm, corresponding to an effective mode area of $\lambda^2/50$ at 10 nm gap. The theoretical Purcell factor F_P and the corresponding coupling factor β for a Si nanowire with 270 nm diameter are shown in Fig. 4.6b with respect to gap size, where an optimally-placed linear vertical dipole at the center of the gap region is assumed in the calculation. A tiny gap (below 40 nm) is crucial for observing the emission enhancement effect. Simulation of Purcell effect with varying diameter (Fig. 4.6c) at a fixed gap = 10 nm shows modal structure of the squeezed photonic modes and confirms that interaction with the 2nd order mode is dominant in our experimental configuration. In particular, since the dipole moment of a

colloidal QD is randomly oriented in the plane perpendicular to its crystalline *c*-axis [73], [75], we expect to observe experimentally a Purcell enhancement of at most $F_P/2$, under an optimal condition where the *c*-axis of the QD is horizontal. The measured large Purcell factor of 31 for QD2 in Fig. 4.5 therefore can correspond to a theoretical value of 62 or higher, at the gap of 9±1 nm consistent with actual geometry of the structure. Moreover, the experimentally measured emission coupling efficiency of 80% agrees well with the value of 82% from theory and is hardly affected by 2D orientation averaging.

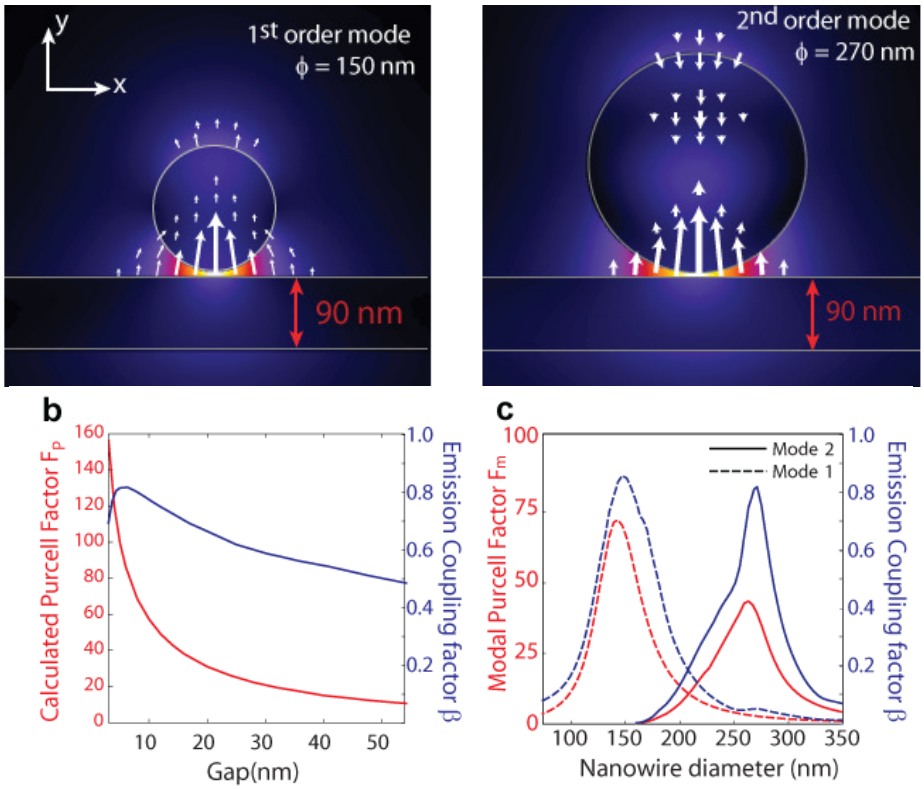

Figure 4.6. Theoretical calculation of Purcell effect in squeezed photonic waveguide (a) The simulated distribution of the |***E***|-field of the 1st and 2nd eigenmode, at nanowire diameter 150 nm and 270 nm respectively, show strong light confinement in the air gap region between the nanowire made of Si and slab made of ZnS. Arrows indicate ***E***-field vectors of the cross-sectional components (E_x and E_y). The slab thickness is optimized to 90 nm for strongest field confinement. Large Purcell factor and near unity coupling factor persist over a rather broad range of nanowire radius and optical wavelength. (b) Theoretical value of the total Purcell emission enhancement factor F_P and corresponding emission coupling factor β as a function of gap size. The simulations are performed under the experimental conditions: slab material ZnS ($n_2 = 2.3$), nanowire material Si at 800 nm ($n_1 = 3.712 + 0.0085i$), the nanowire diameter is 270 nm. The vertically aligned dipole is assumed at the middle of the gap. Strong dependence on the gap size is evident, meaning a tiny gap is crucial for observing the emission enhancement effect. (c) Modal Purcell factor F_m at varying nanowire diameter for a fixed gap of 10 nm, together with its corresponding coupling factor, reveals the modal structure and prominent interaction with the 2nd guided squeezed photonic mode at the operational diameter (270 nm) in our experiment.

4.6. Fluorescence intermittence and output photon flux in the coupled system

The experimentally demonstrated all-dielectric sub-wavelength-confined waveguide also substantially improves the emission dynamics of the emitter. Strongly suppressed blinking behavior and enhanced brightness of the QD is observed when coupled to the waveguide. Fig. 4.8 shows fluorescence time traces of the QD measured at SPCMs with 100 ms resolution. Fluorescence blinking of QDs is associated with carrier trapping at surface defects of the QD shell [79], [80]. When coupled, the QD is in the bright state 90% of the time, whereas only 63% of the time when uncoupled. The strongly confined waveguide mode accelerates the radiative decay of QD which then competes effectively against the non-radiative transition into the dark state, thereby suppressing the blinking. This blinking suppression, along with the reduction of intensity saturation results in an increase in total fluorescence.

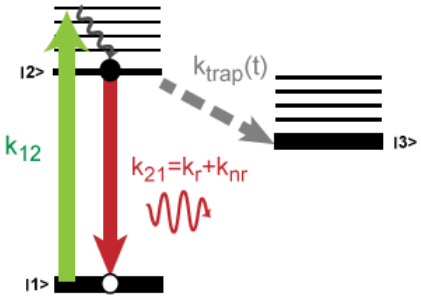

Figure 4.7. A three-level model of the QD describing its fluorescence intermittence. The blinking can be explained as a result of competition between two processes: radiative transition from exciton state |2> to ground state |1> and another diffusion-controlled transition from the exciton state |2> to a charge-trapped state |3> whereby radiative emission from the exciton become quenched by Auger recombination due to the presence of the trapped carrier at the surface defects. During the period of bright state emission the emission dynamics of the QD can be explained by a simple two-level model.

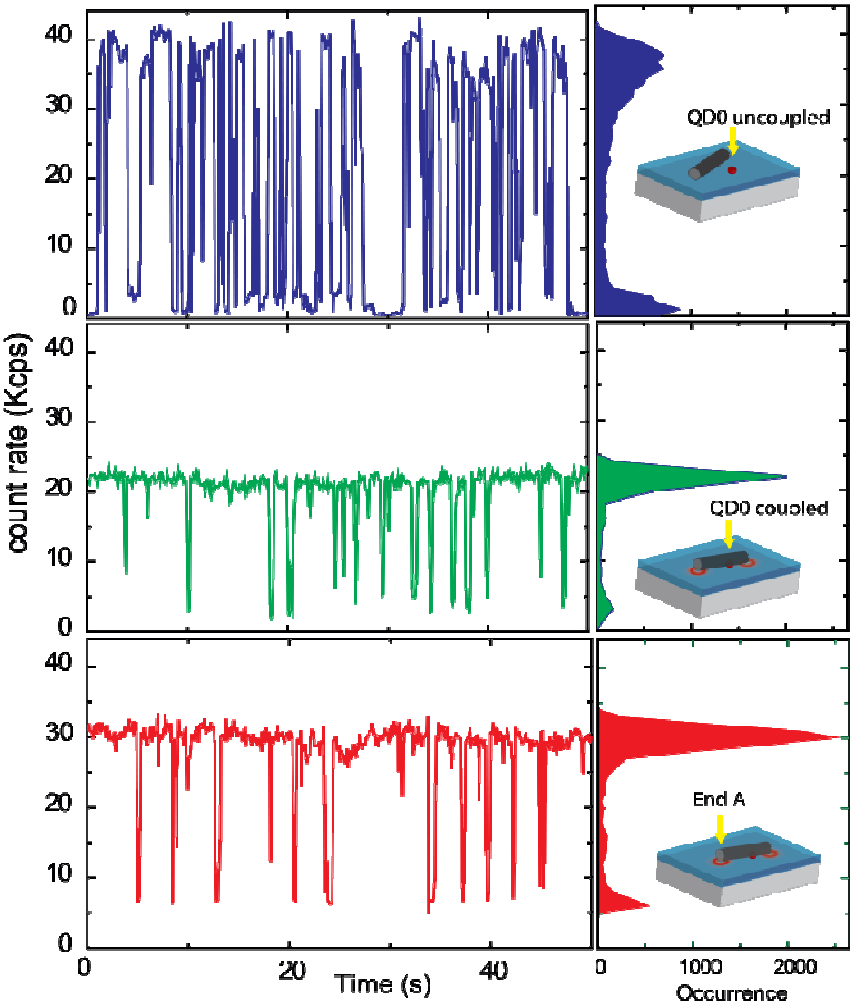

Figure 4.8. Observation of blinking suppression of the QD coupled to the squeezed photonic mode. Fluorescence time traces of the QD (left panel) measured at the single photon counters with 100 ms resolution with their corresponding histograms of count rate (right panel). The blinking behavior of coupled QD1 (bottom and middle panel) is strongly suppressed compared to the same QD1 when uncoupled (top panel). The QD is in the bright state 90% of the time when coupled whereas only 63% of the time when uncoupled. This is manifested in a sharp increase in the fraction of bright state emission to the dark state emission in the middle and bottom histogram.

Estimation of emission quenching factor from the quantum dot bright state emission

The quantum dot can be approximated as a simple two-level system during its on-time or bright state emission [74], [79]. Overall emission rate of the quantum dot in the bright state is equal to $k_{12} * k_r/(k_{12}+k_{21})$, where k_r is the radiative decay rate of the upper state, k_{12} is the excitation rate from state 1 to 2, k_{21} is the transition rate from state 2 to 1 that includes radiative (k_r) and non-radiative (k_{nr}) parts. The overall emission rate can be written as a product of

excitation rate k_{12}, emission saturation factor of the bright state $k_{21}/(k_{12}+k_{21})$ and radiative emission factor $F_r/(F_r+F_{nr})$. Here F_r is the radiative Purcell emission enhancement factor, F_{nr} is the non-radiative contribution of the Purcell emission enhancement factor $F_P = F_r+F_{nr}$. This non-radiative quenching rate is a result of absorption loss of the Si material when the emitter is placed in the vicinity of the Si nanowire..

We analyze the blinking behavior of QD from its intensity time trace where we determine the emission rate at the bright state which accounts for the highest 80% of the intensity distribution. When uncoupled, in the bright state the quantum dot emits on average 35 photons per ms into the single mode fiber. When coupled, the quantum dot emits about 77 photons per ms. This number corresponds to the emission rate from three spots: the quantum dot position and nanowire ends, compensated for the propagation loss. Next, under the same excitation power of 45mW, the saturation factor for the coupled and uncoupled QD are equal to 1.05 and 2.8 respectively.

Assuming that the excitation rate is not changed after coupling which is reasonable under the condition of large-area illumination in our experiment, we obtain the radiative emission factor of about 85%. This corresponds to the non-radiative Purcell emission quenching enhancement factor of 5 which agrees well with a theoretical estimation of the quenching emission rate for the dipole located 4 nm away from the Si surface (n = 3.712 + 0.0085i).

4.7. Measurement of propagation loss in squeezed photonic waveguide

We characterize propagation characteristics of the waveguide by focusing a linearly-polarized 800 nm laser to a diffraction-limited spot of 1 um in diameter on one end of the waveguide while monitoring transmission along the waveguide about out-coupling at the other end. Optical insertion are optimized by scanning the position and polarization orientation of the laser spot until maximal output at the other end is achieved. Following this same procedure on several waveguide samples of different length, we statistically collect attenuation $log(P_{out}/P_{in})$ in dB vs. length of the waveguides L across the same batch of growth process. Assuming insertion and out-coupling factor α, and propagation length L_P are similar across the waveguides, this data forms approximately linear relationship $log(P_{out}/P_{in}) = log(\alpha) - L/L_P$ which are fitted to obtain the propagation length of 1.5 ± 0.2 μm and insertion and out-coupling efficiency $\alpha = 0.28 \pm 0.09$.

Similar measurement done on the same batch of Si nanowires spin-cast directly on a glass coverslip reveal only marginally longer propagation length of 1.7 μm. This finding implies that most of the loss likely arise from the nanowire material but not from the ZnS slab. Improvement in nanowire material and growth method, e.g. reduction of defects which acts as non-radiative recombination centers and longer wavelength operation within the band gap of the material are expected to eliminate propagation loss.

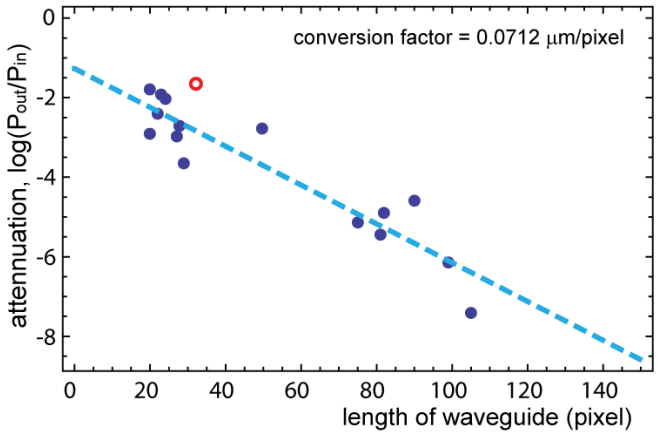

Figure 4.9. Propagation length measurement of the squeezed photonic waveguide

For the specific nanowire that exhibits strong coupling from a single quantum dot in Fig 4.5, the attenuation is found to be -7.2 dB across its 2.3 μm length(Fig 4.9, red empty circle), slightly less than fitted-average shown in Fig 4.9 above.

4.8. Estimation of emission coupling factor β

The apparent radiative coupling factor, η, as presented in section 4.3. is defined as $\eta = (I_A + I_B)/(I_{QD} + I_A + I_B)$, where I_A and I_B is the emission intensity at the ends of the waveguide and I_{QD} is the emission intensity collected at the quantum dot position (i.e. free space emission not coupled to the waveguide mode). For the quantum dot (QD2) coupled to the waveguide mode shown in Fig. 4.5 an apparent coupling factor of 73% is found. However, the nanowires used have a propagation distance of L_P= 1.5 μm, as estimated from measurements in section 4.7, and there is a difference in the collection efficiency of the emission at the end of the waveguide and at the quantum dot position due to different radiation patterns (Fig. 4.10). When these two aspects are taken into account, the coupling factor, β, of the quantum dot to the waveguide mode is given by:

$$\beta = \frac{\gamma_A^{-1} I_A e^{\left(\frac{l_A}{L_P}\right)} + \gamma_B^{-1} I_B e^{\left(\frac{l_B}{L_P}\right)}}{\gamma_{QD}^{-1} I_{QD} + \gamma_A^{-1} I_A e^{\left(\frac{l_A}{L_P}\right)} + \gamma_B^{-1} I_B e^{\left(\frac{l_B}{L_P}\right)}} \qquad 4.1.$$

Where l_A and l_B are the distances from the quantum dot to end A and B of the waveguide, and γ is the collection efficiency depending on the radiation pattern with respect to collection optics, with subscripts denoting the positions (end A, end B and QD position). For the scattering at the end of the nanowire, $\gamma_A = \gamma_B = 31\%$, and for free space emission of the coupled quantum dot $\gamma_{QD} =$ 15%. The effect of loss in the waveguide and the higher collection efficiency at the end of the waveguide tend to cancel out and the final coupling factor is found according to (4.1) to be 75%. (Fig. 4.10)

Simulation based on exact experimental configuration yields an estimate of objective's collection efficiency of 31% from out-coupled radiation at an end of the waveguide, an improvement in

contrast with merely 15% of free-space radiation from the QD into the substrate side (Fig 4.10). While simulation reveals that exact radiation pattern from the ends of the waveguide depends precisely on the length of the waveguide and the position of the emitter, the fraction of power collected by the objective stays in the range of 28%-36% of total out-coupled radiation over the full solid angle.

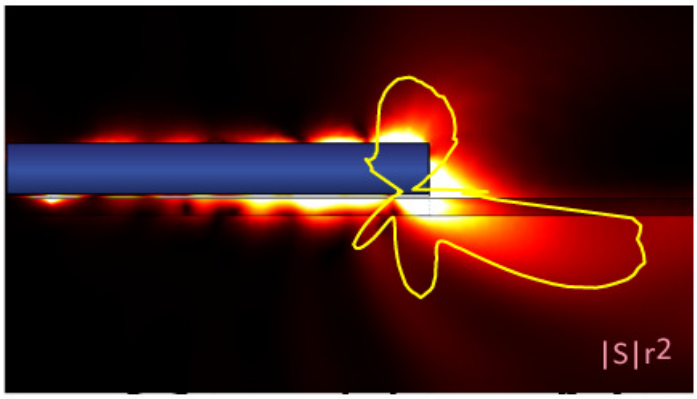

Figure 4.10. Simulated radiation pattern $|S|r^2$ of light scattered out from an end of the waveguide after emission from the QD is coupled to the squeezed photonic mode and propagated along the waveguide. The geometry is in correspondence with experimental configuration (lossy Si nanowire 2.3 μm long, ϕ = 270 nm and ZnS 90 nm thick slab). A contour line showing the lobes of radiation is a guide for the eyes. In comparison with uncoupled configuration (no nanowire) where the QD radiates into the substrate around a grazing angle of about 13º, the coupled QD radiates into substrate from its physical position at the same grazing angle but with almost order of magnitude less power than the multi-lobe radiation from the ends of the waveguides which points more toward the optical axis. Combining this finding with experimental collection angle of the NA1.3 oil-immersion objective ($\theta_{collect}$ = 60º from optical axis), we obtain an increase in collection efficiency of 31% at the end of the waveguide compared to 15% at the QD position.

Effect of dipole orientation on photon collection efficiency

Optical structures that can accomplish high photon collection efficiency [9] typically involve control of radiation pattern so as to match the acceptance angle of the collection optics. In addition, Purcell effect of radiation into the dominant mode of collection can boost the collection efficiency value although itself is not a pre-requisite for high collection efficiency. However, in configurations without Purcell effect such as photonic nanowires[68], [71] and planar dielectric antenna[69], an alignment of a linear dipole orientation with respect to the optical structure is critical in achieving high collection efficiency such that they are limited to emitters such as diamond NV-centers and self-aligned organic dyes inside a crystalline organic matrix. On the other hand, certain quantum emitters of technological importance such as colloidal quantum dots--having 2D degenerate dipole, and single atoms or ions--having 3D isotropic radiation, will allow respectively the collection efficiency of at most 1/2 or 1/3 of the optimal collection efficiency in structures without Purcell effect. For optical structures that

incorporate large Purcell enhancement effect F_m into the collected optical mode, averaging of dipole orientation yields a more favorable coupling efficiency as the following analysis reveals.

Suppose the z-dipole orientation has the highest coupling efficiency $\beta_z = \beta_{max} \sim 1$ but no Purcell effect (β_x , $\beta_y << 1$ typically), the orientation-averaged coupling efficiency $< \beta >$ is reduced by the averaging dimensionality:

$$\langle\beta\rangle = (\beta_x + \beta_y + \beta_z)/3 \approx \frac{\beta_{max}}{3}$$

On the other hand, if we assume Purcell effect $F_m \gg 1$ for z-dipole, averaged coupling efficiency becomes

$$\langle\beta\rangle = \frac{(\gamma_x + \gamma_y + \gamma_z)/3}{(\gamma_{total,x} + \gamma_{total,y} + \gamma_{total,z})/3}$$

where γ_x γ_y and γ_z represents decay rates into the relevant optical mode of a linear dipole oriented along the corresponding axes, whereas $\gamma_{total,x}$ ($\gamma_{total,y}$ and $\gamma_{total,z}$) represents total decay rate of the x-(y and z) dipole.

Since we have assumed the optical mode has dominant z-polarization $\gamma_z = F_m \gamma_0$ and $\gamma_{total,z} \sim F_m \gamma_0 + \gamma_{free}$ whereas $\gamma_{total,x}$, $\gamma_{total,y} \sim \gamma_0$, and γ_x , $\gamma_y < \gamma_0$

Using $\beta_{max} = \frac{F_m \gamma_0}{F_m \gamma_0 + \gamma_{free}}$

then

$$\langle\beta\rangle \approx \frac{F_m + 2}{F_m/\beta_{max} + 2} = \beta_{max} + (\beta_{max} - \beta_{max}^2)\frac{2}{F_m} + O[\frac{2}{F_m}]^2 \qquad 4.2.$$

up to the first leading order in the small number $\frac{2}{F_m}$

(4.2) means that for large enough Purcell effect ($F_m \gg 2$), the coupling efficiency of a freely rotating dipole to the desired optical mode approaches that of an optimally-aligned linear dipole β_{max}. The large value of averaged coupling efficiency approaching that of a vertical dipole (~77%) is also observed in our experiment despite the two-dimensional averaging effect in colloidal quantum dots, i.e. measured $F_P = \langle F_P \rangle = \frac{F_{P,vertical}}{2} \approx 31$.

4.9. Summary and outlook

In conclusion, we demonstrated that high-index-contrast dielectrics can be used to achieve deep sub-wavelength field confinement, implementing an all-dielectric waveguide QED system with a mode area of 10 nm by 75 nm. The strongly enhanced interaction between the single QD and the squeezed photonic mode and its effect on the emission dynamics has been observed experimentally with a record high Purcell enhancement factor of 31. The small footprint and

broad-band nature of this simple but efficient system suggests a broader use for efficient on-chip optical components and networks both at classical and quantum level.

Chapter 5
Hybrid Plasmon Crossbar Cavity: scaling of deep sub-wavelength dipole resonator

Analysis in Chapter 2 and experimental verification in Chapter 3 and 4 have demonstrated that deep sub-wavelength confinement in guided photonic structures can enhance optical interactions significantly under a broad bandwidth, away from the surface plasmon resonance in metal and even in all-dielectric waveguides which have no resonance at all. While strong interaction in a one-dimensional continuum possesses several useful implications in quantum optics [19], [39], study of two-dimensional slab waveguide geometries in Chapter 2 have also indicated that a large degree of enhancement comes mainly from confinement in one gap dimension alone. In particular, Fig. 2.5. reminds us that even in a thick slab structure, the total Purcell effect which encompasses multiple higher-order transverse modes remain large and that a dipole emitter can interact strongly with several modes at the same time.

For use of these guided structures for gain enhancement in a low-threshold laser, further confinement in the other dimensions, namely termination along the length of a one-dimensional hybrid plasmon waveguide [47] to form a hybrid plasmon nanowire cavity and termination of the two-dimensional plane of a hybrid plasmon slab [81] to create a rectangular hybrid plasmon cavity, has been introduced to limit the number of optical modes and provide sufficient feedback for optical amplification. While optical gain in the lasing mode is enhanced by the Purcell effect, high reflectivity at the nanowire ends in the former case or total internal reflection at the edge of the square cavity in the latter case, large free-spectral range (FSR) caused by the small size of the device, and large propagation wave-vector, corroborate to allow selection of a few longitudinal modes via mode competition while sustaining their ultrafast laser dynamics[47], [81]. The threshold of these lasers is therefore lowered [7], [47]. From the point of view of laser applications, these lasers are compact and efficient enough even if they are operated at a high-order longitudinal mode number.

The interest of this chapter, however, lies in radiation properties and optical confinement in an extreme case of the first-order longitudinal mode of a hybrid plasmon cavity, obtained by scaling down the lateral size of the hybrid plasmon square cavity to dimension on the order of the effective hybrid plasmon wavelength. This resonator, sub-wavelength in all three dimension, has a dipole-like mode profile akin to a $\lambda/2$-antenna[3] and particle plasmon. Nevertheless, in the similar vein as our investigation in the earlier chapters that optical confinement in the gap dimension are achieved in a non-resonant way, we explore the benefits of this resonator design based on deep sub-wavelength guided modes.

This chapter begins with discussion on the localized surface plasmon (LSP) excitation in a metallic sphere (i.e.particle plasmon) and its radiation behavior, as point of comparison. Scattering theory which provides information about localized optical modes and its dissipative behavior is explained therein and is used as a framework for analysis of other photonic structures. Later, two designs of deep sub-wavelength HPP resonators are explored by theoretical

simulation. The results show that these resonators offer a wide tunability of resonant wavelengths, possess low absorption cross-section as they operate away from the intrinsic surface plasmon resonance and have unprecedentedly small mode volume. In the second design where the materials are extended into long strips, radiation from the resonator is out-coupled efficiently via the integrated strip waveguide to improve radiative efficiency and peak scattering cross-section while still maintaining ultrasmall mode-volume. The final resonator design demonstrates versatility as a 3-port device for efficient optical addressing of emitters inside the ultra-small cavity region via free-space coupling and transmission along the waveguide.

5.1. Scattering theory of small metal particle

5.1.1. Localized surface plasmon mode in the scattering spectrum

The scattering cross-section of a particle defined as scattered power normalized by the incident field intensity is given by

$$C_{sc} = \frac{P_{out}}{I_{inc}} = \frac{k^4}{6\,\pi}|\alpha|^2 \tag{5.1.}$$

For a particle much smaller than the wavelength, we obtain the Rayleigh scattering limit with the quasistatic polarizability of a sphere α induced by an incident electric field $\vec{E}_i$ given as

$$\alpha = \alpha_{quasi-static} = \frac{1}{\frac{1}{3}\frac{\varepsilon+2}{\varepsilon-1}} V = 4\,\pi a^3 \frac{\varepsilon-1}{\varepsilon+2} \tag{5.2.}$$

where a is the radius of the sphere and $V = \frac{4\pi}{3}a^3$ is the volume of the sphere.

For metallic particles whose permittivity can be negative, the electrostatic polarizability has a pole at $\varepsilon = -2$. This corresponds to a resonance in the scattering cross-section C_{sc} whereby a localized optical mode of the nanoparticle is excited by the plane wave. Since we are also interested in the radiative property, we can simply add a correction term due to radiative damping to the above quasi-static approximation.

The quasi-static electric dipole induced in the small sphere $\vec{p} = \varepsilon_0 \alpha \vec{E}_i$ radiates an electric field $\vec{E}_{rad} = i\,\frac{2}{3}\frac{k^3}{4\pi\varepsilon_0}\vec{p}$ so that the dipole becomes $\vec{p} \to \vec{p} = \varepsilon_0\alpha(\vec{E}_i + i\,\frac{2}{3}\frac{k^3}{4\pi\varepsilon_0}\vec{p})$. Therefore we may replace the polarizability α in Equation (5.1) by the effective polarizability α_{eff} from $\vec{p} = \varepsilon_0\alpha_{eff}\vec{E}_i$ which includes radiative damping

$$\alpha_{eff} = \frac{\alpha}{1 - i\frac{\alpha}{4\pi}\frac{2k^3}{3}} \tag{5.3.}$$

From this simple quasi-static limit, we may conclude the following

1. The location of the resonance is at the angular frequency $\omega_{LSP}$where $\varepsilon(\omega_{LSP}) = -2$, which follows the relationship $\omega_{LSP} = \frac{\omega_P}{\sqrt{3}}$ if one assume the Drude dielectric model of metal: $\varepsilon(\omega) = 1 - \frac{{\omega_P}^2}{\omega^2 + i\,\omega\gamma_e}$ (with harmonics $e^{-i\omega t}$ of the Physics convention), where ω_P is the plasma frequency of the metal, γ_e is the electron damping constant of the metal, and ω is angular frequency, all in radian/sec
2. The shape of the Rayleigh scattering cross-section spectra is related to the imaginary part of the pole which comes from two features
   a) Material dispersion or Ohmic loss of the metallic material in the imaginary part of $\varepsilon(\omega)$
   b) Radiative damping, which is the pure imaginary term in the pole of α_{eff}

From these aspects, we can deduce that a localized optical mode of the particle appear as a resonance in the scattering cross section and one can therefore use this information to study the dissipative processes of this mode whether they be via radiative damping or Ohmic loss. On the other hand, extinction cross section $C_{ext} = k\, Im(\alpha)$ and absorption cross section $C_{abs} = C_{ext} - C_{sc}$, while being important measurables in an experiment, are less direct in interpretation of a localized optical mode. The rest of this chapter therefore focuses on simulation and analysis of scattering cross section of some novel deep sub-wavelength resonators. The width of the resonance in the scattering cross-section yields the total quality-factor Q of the mode including loss due to radiation and material absorption. When the material loss in excluded ($Im(\varepsilon) = 0$), one simply isolates radiation quality factor of the mode Q_{rad} from the resulting scattering spectrum. Absorption quality-factor Q_{abs}can be recovered through the relationship

$$\frac{1}{Q} = \frac{1}{Q_{rad}} + \frac{1}{Q_{abs}} \tag{5.4.}$$

For a larger particle, retardation effects have to be taken into account and this could be done by expansion of the first TM mode in Mie theory to obtain a general expression [82], [83]

$$\alpha_{Mie} = \frac{1 - \frac{1}{10}(\varepsilon + 1)x^2 + O[x^4]}{\frac{1}{3}\frac{\varepsilon + 2}{\varepsilon - 1} - \frac{1}{30}(\varepsilon + 10)x^2 - i\,\frac{2x^3}{9} + O[x^4]} V \tag{5.5.}$$

$x = ka$ is size parameter, a is the radius of the sphere, k is the free space wave vector, and $V = \frac{4\pi}{3}a^3$ is the volume of the sphere. Correction to the quasi-static limit appears in the second term in the denominator as the energy shift, while the third term is radiative damping which is pure imaginary.

5.1.2. Radiation behavior of a small metallic sphere and bandwidth limitation of a small antenna.

Writing out explicitly the expression for the scattering cross-section (5.1 and 5.4) while assuming the Drude metal is lossless ($\gamma = 0$ and $\varepsilon(\omega) = 1 - \frac{{\omega_P}^2}{\omega^2}$) , one obtains

$$C_{sc} = \frac{8\pi}{3} k^4 a^6 \frac{{\omega_{LSP}}^4}{(\omega^2 - {\omega_{LSP}}^2)^2 + ({\omega_{LSP}}^2 \frac{2\,k^3 a^3}{3})^2} \tag{5.6.}$$

This is approximately Lorentzian for frequency $\omega + \omega_{LSP} \approx 2\omega_{LSP}$ around the resonance $\omega_{LSP} = \frac{\omega_P}{\sqrt{3}}$

$$C_{sc} \approx \frac{8\pi}{3} k^4 a^6 \frac{{\omega_{LSP}}^2}{(\omega - \omega_{LSP})^2 + (\omega_{LSP} \frac{k^3 a^3}{3})^2} \tag{5.7.}$$

with the second term in the denominator equal to the half-width-half-max $\frac{\Gamma}{2} = \omega_{LSP} \frac{k^3 a^3}{3} = \frac{\omega_{res}}{2Q}$, which simply yields a radiation Q-factor Q_{rad} in the limit of small metallic sphere.

$$Q_{rad} = \frac{3/2}{(ka)^3} \tag{5.8.}$$

As a result, it is apparent that a small metal nanosphere does not radiate well, and that the dissipation of the localized surface plasmon in the quasistatic limit is dominated by Ohmic loss in the metal rather than radiation into free space.

Similarly in microwave antenna theory, it is well-known from the study of electrically small antenna ($ka \ll 1$) that the radiation Q-factor of the small resonator has a lower limit [84], [85] called the Chu limit which fundamentally restricts the antenna bandwidth.

$$Q_{rad} \geq \frac{1}{(ka)^3} + \frac{1}{ka} = Q_{Chu} \tag{5.9.}$$

$k = 2\pi/\lambda$ is free space wave vector

a is the radius of smallest sphere enclosing antenna, namely "Chu radius"

The principal challenge of designing small antenna (in the regime $ka < 0.5$ or $a < \frac{\lambda}{12}$) is, therefore, to approach this limit as closely as possible. We may then assign the figure of merit of the antenna bandwidth compared to this theoretical limit as Chu factor : $Q_{rad}/Q_{Chu} \geq 1$.

The metallic nanosphere with negative permittivity studied above has a Chu factor of 1.5, quite close to the Chu limit.

5.1.3. Effective mode volume of particle plasmon in the quasi-static limit.

The quasi-static potential of a metallic sphere can be written explicitly by multipole expansion into spherical harmonics[4], [86].

$$\Phi_1 = \begin{cases} \frac{a}{l+1} E_{max,l} \left(\frac{r}{a}\right)^l P_l(\cos\theta), & r > a \\ \frac{a}{l+1} E_{max,l} \left(\frac{a}{r}\right)^l P_l(\cos\theta), & r \leq a \end{cases} \quad 5.10.$$

$P_l(\cos\theta)$ is Legendre polynomial, where l denotes lth localized surface plasmon mode and $E_{max,l}$ is the maximal electric field just outside the sphere at $r = a$ and $\theta = 0$. The surface charge density related to the normal component of electric field is then $\sigma_l(\theta) = (2l+1)(l+1)\varepsilon_0 E_{max,l} P_l(\cos\theta)$. The dipole mode is marked by $l = 1$. The effective mode volume is found through the energy of the mode as an integral over the surface of the sphere.

$$U_l = \frac{1}{2} \oiint \Phi_1 \sigma_l \, d^2r = \frac{1}{2} \varepsilon_0 E_{max,l}^2 V_{eff,l} \quad 5.11.$$

This eventually gives the effective mode volume of particle plasmon in the quasi-static limit[86]

$$V_{eff,l} = \frac{4\pi a^3}{(l+1)^2} \quad 5.12.$$

For the electric dipole mode $l = 1$, the mode volume is $3/4$ of the physical volume of the sphere.

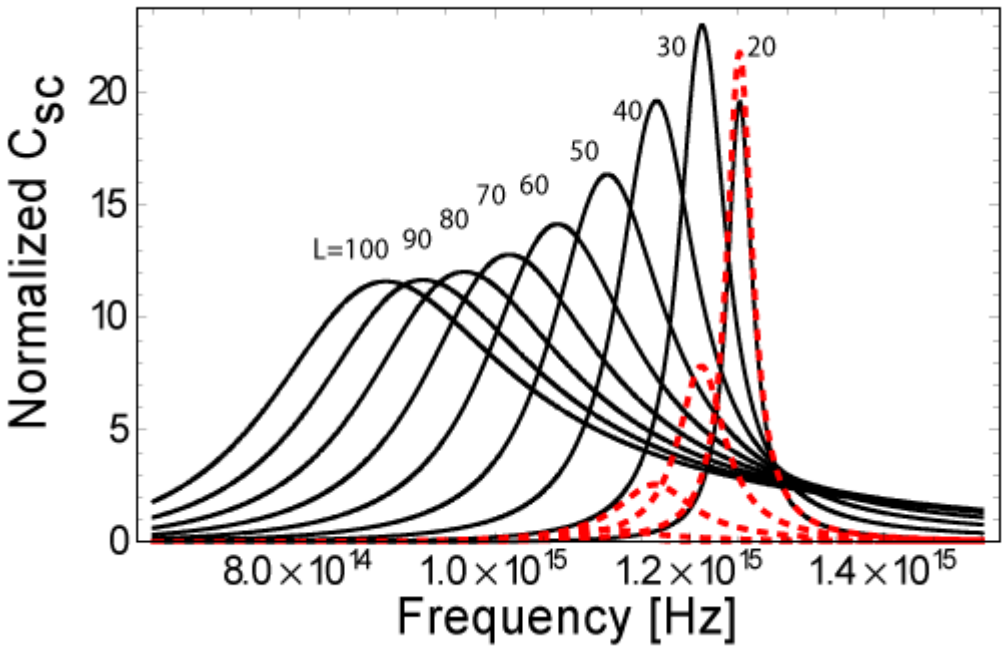

Figure 5.1. Normalized scattering spectra of Ag nanoparticle of radius $a = L/2$ =10-50 nm , calculated from Mie theory. (Dielectric permittivity of Ag are assumed to be according to the Drude model $\varepsilon(\omega) = 1 - \frac{{\omega_P}^2}{\omega^2 + i\,\omega\gamma_e}$ with $\omega_p = 1.4 \times 10^{16}\ rad/s$ and $\gamma_e = 1.2 \times 10^{14}\ rad/s$). The scattering cross-section $C_{sc}/\frac{\pi L^2}{4}$ (thick black line) and the absorption cross-section $C_{abs}/\frac{\pi L^2}{4}$ (red, dashed), all normalized to the physical cross-section are shown together with respect to free-space frequency. Each spectrum displays a resonance peak characteristic of the particle plasmon which asymtotically approaches the quasi-static value of $\omega_{LSP} = \frac{\omega_P}{\sqrt{3}} = 1286\ THz$ as the nanosphere shrinks in size. The resonance of larger nanoparticles are red-shifted from the quasi-static limit due to the retardation effect. The value of normalized peak scattering cross-section, which is larger than unity suggesting efficient scattering by the nanosphere, decreases with smaller particle size just about the same point as absorption cross-section begins to dominate in the extinction spectrum (at $L = 30\ nm$) This is a result of particle plasmon resonance moving closer to plasma frequency where the Ohmic loss of metal is high.

5.2. Hybrid plasmon polariton (HPP) deep sub-wavelength resonators

The advantage of a hybrid plasmon mode in terms of its long propagation length together with extreme confinement have been explored in recent works to make nanolasers and 2D square lasers[47], [81]. Together with the extreme concentration which enhance the gain and optical interaction with active materials in the these laser cavities, these studies focus on efficient feedback mechanism of the higher-order longitudinal modes for efficient reflection lasing action. Also more recent studies began to look at extending the metallic and dielectric material to form a

strip waveguide architecture (a crossbar) which still supports cavity mode, thanks to high reflection at the end facets due to sufficient impedance mismatch of the HPP guided mode to free space[47], [81], but with significant out-coupling into the waveguides.

An interesting question arises as one tries to scale the other two dimensions of the cavity further down to a single mode regime where quantum electrodynamics (QED) play an important role and the behavior of interactions is governed dominantly by the extreme deep-subwavelength mode volume which may enable QED effects to occur in the presence of an active material.

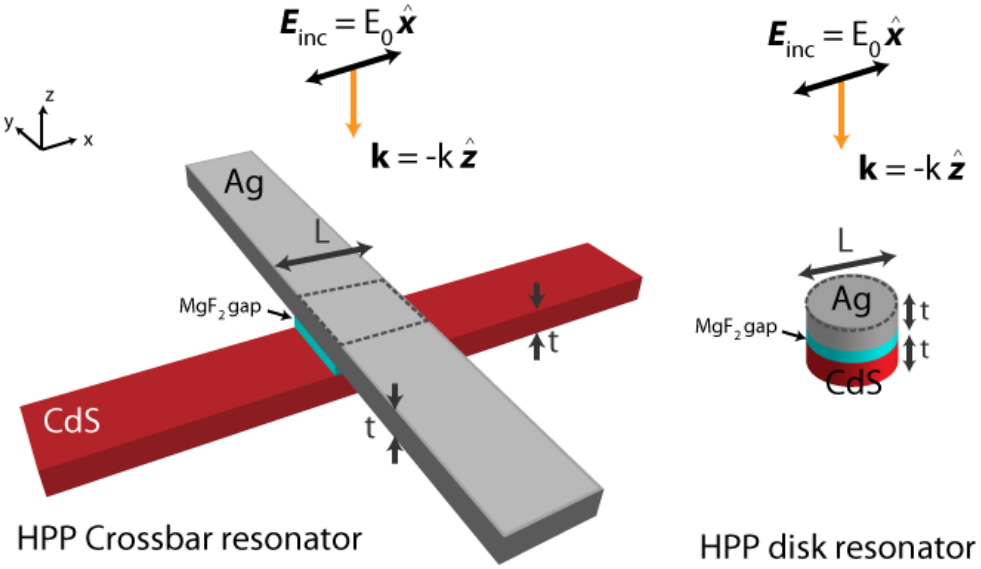

Figure 5.2. Deep sub-wavelength dipole resonators studied. (Left) A hybrid plasmon crossbar is made of a long plasmonic metal strip, in this case silver (Ag), and another long strip of high index dielectric material CdS (index = 2.3), both of thickness t = 7.5 - 15 nm, separated by a low refractive index gap made of MgF_2 (index = 1.38) of gap thickness g = 5 nm. In a scattering simulation, an x-polarized plane wave of wave vector $k = \frac{\omega}{c}$ is incident from the top which specifically excites the fundamental dipole mode of the crossbar to be explained in next figure. The physical cross-section in this scattering configuration is marked by the dotted square of area $L \times L$, where L is the width of the strips in the range of 20-100 nm. While the field of the fundamental mode is localized in the overlapping gap region, significant amount of propagation is supported by the waveguided mode along the Ag strip. **(Right)** A hybrid plasmon disk is the closed cavity version of a two-dimensional hybrid plasmon guided mode. An equivalent HPP disk structure has a similar geometry and scattering configuration as the corresponding crossbar. However, the physical cross-section (shown as dashed circle) occupies an area of $\frac{\pi L^2}{4}$.

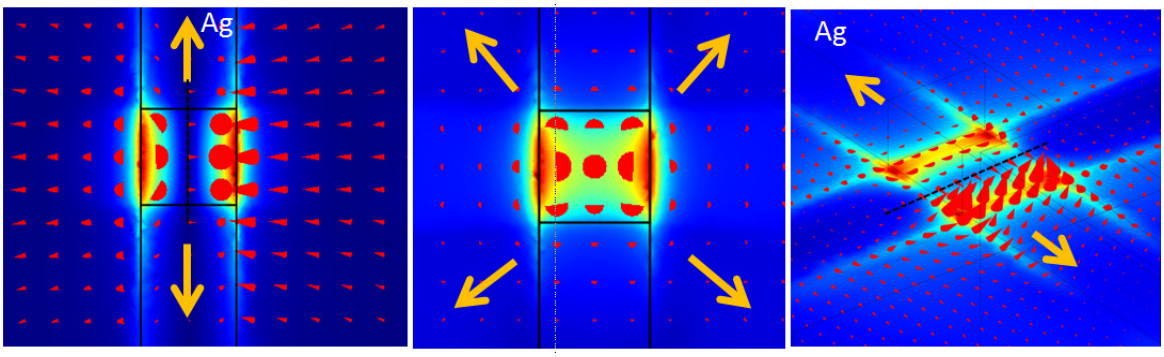

Figure 5.3. Fundamental modes of the HPP crossbar from lowest to highest resonant energy (left to right). Since the hybrid plasmon (HPP) two-dimensional guided mode confined in the gap region has dominant E-field polarization along vertical direction, the fundamental dipole modes possess similar feature and can be distinguished from each other by the node in the E_z-field profile. $|E_z|$-field distribution (as density plot) and E-field vector (red arrows) are shown in the plot. The lowest dipole mode which is of utmost interest has a node in E_z (represented by dashed line) along the y-axis (midline of Ag strip) with non-zero E_x along the node, maximal electric field near the edge of Ag strip in the gap region, and more propagated power along the Ag-strip than along CdS-strip. From the E-field distribution, this mode is reminiscent of a metallic dipole antenna along the width of the Ag strip (x-direction) but with field confinement in the gap due to HPP mode. The second dipole mode has no node in E_z and most of electric field along the z-direction so that the field distribution is reminiscent of a patch antenna which has a magnetic-dipole-like radiation pattern. Due to polarization mismatch to the possible guided optical mode in the strips, the field radiates mostly spherically into free space instead of propagating along the waveguides. The third mode has a node in E_z along the x-axis (midline of CdS strip) with non-zero E_y along the node, but the |E|-field is concentrated near the 4 corners of the overlapping gap region.

5.3. Fundamental dipole modes of sub-λ resonators

Since the hybrid plasmon polariton (HPP) two-dimensional guided mode confined in the gap region has dominant E-field polarization along vertical z-axis, the fundamental dipole modes possess a similar feature and can be distinguished from each other by the node in the E_z-field profile. Termination of the HPP slab waveguide in two dimension to form an HPP disk results in two fundamental dipole modes. a) the dipole mode polarized along vertical z-axis with more or less uniform E_z in the gap region. b) doubly degenerate dipole modes polarized in the horizontal xy-plane with a line of node in E_z. The first mode is reminiscent of a micropatch antenna in the microwave/RF frequencies[87], [88]. The second mode is doubly degenerate with maximal electric field at the edge of the disk. This mode radiates better to free-space.
On the other hand, extending CdS and Ag materials to form long overlapping strips as in an HPP crossbar breaks the radial symmetry of the disk and of the z-polarized dipole mode. Symmetry breaking also splits the degeneracy of the in-plane electric dipole mode. Eigenmode solutions based on finite-element method yields the mode profiles as shown in Figure 5.3. The lowest dipole mode (Figure 5.3a) which is of utmost interest has a node in E_z along the y-axis (midline of Ag strip) with non-zero E_x along the node, maximal electric field near the edge of Ag strip in the gap region, and more propagated power along the Ag-strip than along CdS-strip. From the

electric field distribution, this mode is reminiscent of a metallic dipole antenna along the width of the Ag strip (x-direction) but with field confinement pulled into the gap due to HPP mode. The second dipole mode (Fig 5.3b) has no node in E_z and most of electric field along the z-direction so that the field distribution is reminiscent of a patch antenna which has a magnetic-dipole-like radiation pattern. Due to polarization mismatch to the possible guided optical mode in the strips, the field radiates mostly spherically into free space instead of propagating along the waveguides. The third mode (Fig 5.3c) has a node in E_z along the x-axis (midline of CdS strip) with non-zero E_y along the node, but the |E|-field is concentrated near the 4 corners of the overlapping gap region.

5.4. Scattering spectra and scaling of sub-λ dipole resonators

To study the radiation behavior and effective volume of the dipole modes. Scattering spectra of these deep-subwavelength resonators are simulated using scattered field formulation in the finite-element method simulation package COMSOL. In the simulation, an x-polarized plane wave is incident of the HPP crossbar and HPP disk from the top and traveling in -z direction. By symmetry, this plane wave can only exclusively excite the first dipole mode polarized along x-axis (along the width of the Ag-strip) as the other modes does not contain electric field along x. Moreover, the x-polarized dipole mode radiate to free-space better than the other dipoles. Considering this symmetry, the simulation domain is further reduced to one quarter of the full domain by setting the yz-plane as perfect electric conducting boundary and xz-plane as perfect magnetic conducting boundary to reduce memory usage and speed up the computation. A perfectly matched layer (PML) was used in the outermost domain of simulation to eliminate reflection of scattered wave by the outer boundary. Very fine mesh of 1 nm maximum size in the gap and a growth rate of 1.05 is used to ensure accuracy of the simulation. The FEM simulation is tested with Ag nanosphere against the analytical Mie theory and is found to produce accurate results.

The scattering simulation is employed for geometrical parameters: $g = 5$ nm, $t = 10$ nm, and $L = 20$, 25, 30, 35, 40, 45, 50, and 55 nm together with the Drude model permittivity of Ag where $\omega_p = 1.4 \times 10^{16}\ rad/s$ and $\gamma_e = 1.2 \times 10^{14}\ rad/s$, to produce electromagnetic near-fields scattered by the resonators. The scattered near-field reproduces the x-polarized dipole mode. The scattering cross-section is calculated by integrating the power flux of the scattered field $\frac{1}{2} Re\left(\vec{E}_{sc}(\vec{r}) \times \vec{H}^*_{sc}(\vec{r})\right)$ normal to the outer boundary. Absorption cross-section is also calculated directly by integrating the resistive heating power in the metallic medium. The scattering spectra of HPP crossbar (blue thick line) and HPP disk (brown, thin line) of varying lateral dimension but same thickness t = 10 nm are shown in Fig. 5.4a. The case where Ohmic loss in Ag is excluded is also shown in Figure 5.4b.

In comparison to the scattering spectra of Ag nanospheres of small radius $a = L/2$ in Figure 5.1, the resonances of the HPP disks and HPP crossbars are red-shifted away from the localized surface plasmon resonance $\frac{\omega_P}{\sqrt{3}}$, and therefore allow tuning of the resonance so that they are spaced evenly with varying lateral size (Figure 5.5). Small Ag nanospheres on the other hand, have resonances that asymptotically approach the quasi-static limit of particle plasmon and the

wavelength tuning available is by introducing retardation effect via larger particle or changing the shape of the particle.

Another consequence of the overall red-shift in sub-wavelength resonators is that as these resonators operate far below the plasma frequency, the absorption cross-section becomes relatively small and tends to be less than the scattering cross-section. This effect is particularly dramatic in HPP crossbar resonator. What this means is that the antenna scattering efficiency, as defined by $\eta_{scatt} = \frac{C_{sc}}{(C_{sc}+C_{abs})}$ improves. In small Ag-nanospheres, on the other hand, the extinction spectra are dominated by absorption.

Tunability of the first-order dipole mode arises from gradual modal dispersion. Resonance of the resonator may be described approximately by the resonance condition $\beta_{HPP}L + \phi = m\pi$ where $m = 1$ signifies the first dipole mode, and $\beta_{HPP}(g, t; \omega)$ are propagation wave vector of the hybrid plasmon mode and $\phi(g, t; \omega)$ is the positive phase pickup ($0 \leq \phi \leq \pi$) upon reflection at the edge of the cavity[89], [90]. These two are dependent on cross-section geometry of the waveguide (in this case, thickness t and gap g), and ϕ also depends on the specific nature of the termination and eventually on the lateral size L as well, as a result of radiative damping [91]. As in our simulation we fix the cross-section while vary the lateral size. The resonance condition may therefore be rewritten as $\left(\frac{1}{2} - \frac{\phi(\lambda)}{2\pi}\right)\left(\frac{1}{n_{mode}(\lambda)}\right)\lambda \approx L$. The mode index $n_{mode} = \frac{\beta_{HPP}}{k}$ increases at shorter wavelength and according to Ref. [90], the reflection phase ϕ tends to grow at shorter wavelength as well, as a result of the increasing ratio of stored electric energy to magnetic energy and its subsequent excitation of evanescent modes in the free-space region at higher frequency. These two effects work in opposite directions to keep the first two brackets approximate constant, and therefore allows the resonant wavelength to scale with lateral size.

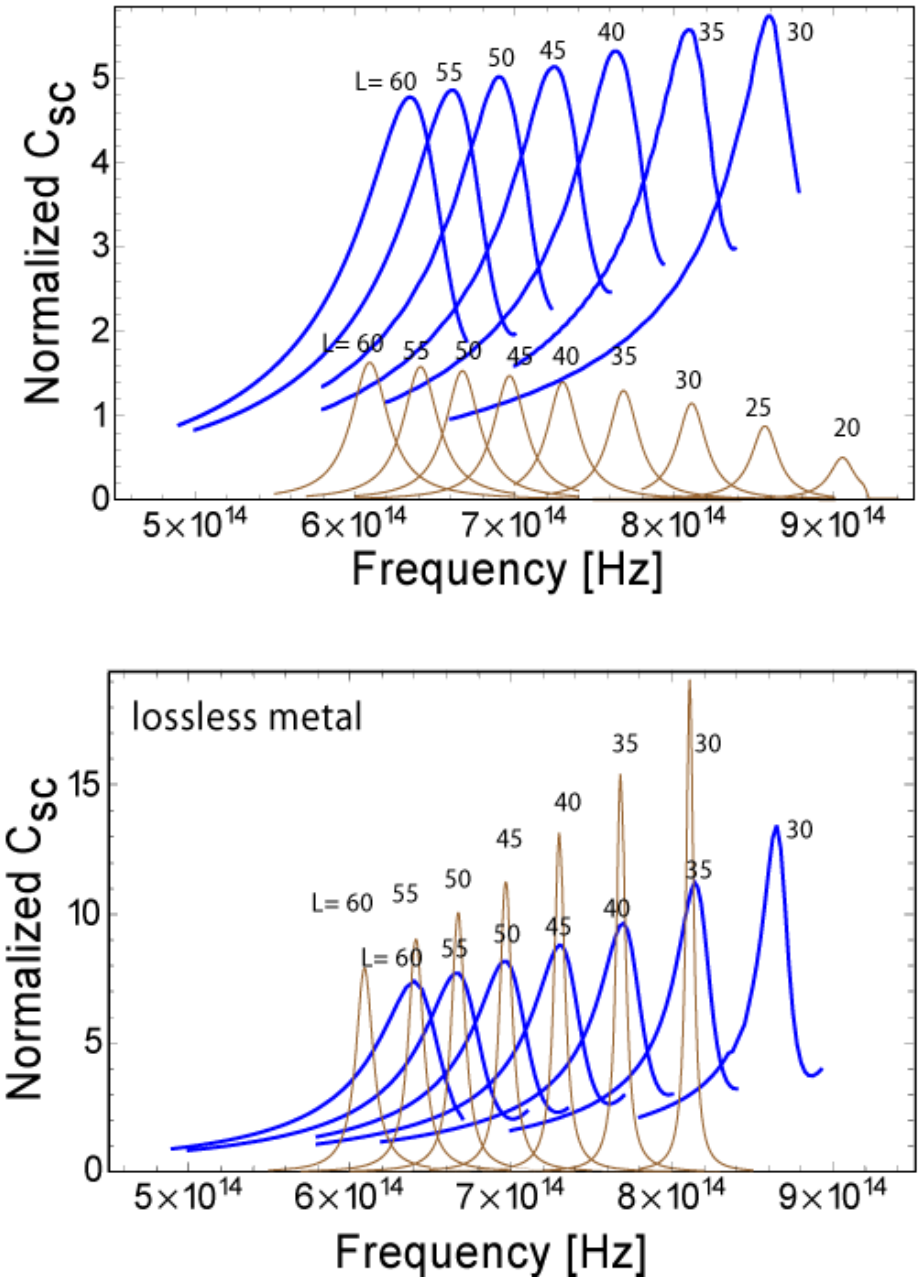

Figure 5.4. Normalized scattering spectra of HPP crossbar C_{sc}/L^2 (thick blue line) and HPP disk resonators $C_{sc}/\frac{\pi L^2}{4}$ (thin brown line) (a) including Ohmic loss in metal ($Im(\varepsilon) > 0$). and (b) neglecting loss in metal ($Im(\varepsilon) = 0$). The results are shown for geometrical parameters: $g = 5$ nm, $t = 10$ nm, and $L = 20$, 25, 30, 35, 40, 45, 50, and 55 nm. In comparison to the scattering spectra of Ag nanospheres of small radius $a = L/2$, the resonances of the HPP disks and HPP crossbars are red-shifted away from the localized surface plasmon resonance $\frac{\omega_P}{\sqrt{3}}$. This allows tuning of the resonance so that they are spaced evenly with varying lateral size L, rather than narrowly approaching the LSP resonance as in the case of Ag nanoparticle.

Longer operation wavelength albeit the same physical size also means that the deep sub-wavelength resonators are important technologically as a candidate for ultra-compact, electrically-small antenna with the promise for high packing density. Figure 5.6 plots the size parameter $kL/2$, which is a ratio of lateral size to operation wavelength, against the physical size L of Ag nanospheres (empty circles), HPP disks (solid circles) and HPP crossbar resonators (solid diamond). The resonant wavelength and hence the size parameter of the HPP crossbar remains unchanged from the corresponding disk cavity design, suggesting that extending the materials to form strips does not significantly perturb the location of resonance. However, the size parameter of the deep sub-wavelength resonators is overall much smaller than that of nanosphere of the same physical size.

5.5. Ultra-small mode volume of sub-λ resonators

Field confinement in the gap region of the deep sub-λ resonators yields an effective mode volume on the order of the volume of the gap region. Effective mode volume can be calculated directly from simulated scattered field using formula $V_{eff} = \frac{\int w_{em}(\vec{r})d^3\vec{r}}{\varepsilon_0 \varepsilon(|\vec{E}|^2{}_{max})}$ where w_{em} is the electromagnetic energy density of the mode (in this case, from the scattered field profile) and $\vec{E}$ in the denominator is evaluated at the maximal electric field, in this case taken to be at position $(x, y) = (0.95\frac{L}{2}, 0)$ or 5% from the edge of the Ag-strip where the field is optimal. The results from calculations are shown in Fig. 5.7 The mode volume of HPP disks (brown circles) is smaller than the gap volume by about a factor of 1/10. Integrating strip waveguides to form HPP crossbars (blue diamond) raises the mode volume to about as much as the physical volume, as more evanescent coupling spread the fields into the strip region. (b) When normalized to cubic wavelength, the effective mode volume of the HPP crossbars is in the range of 0.0001 to 0.0002.

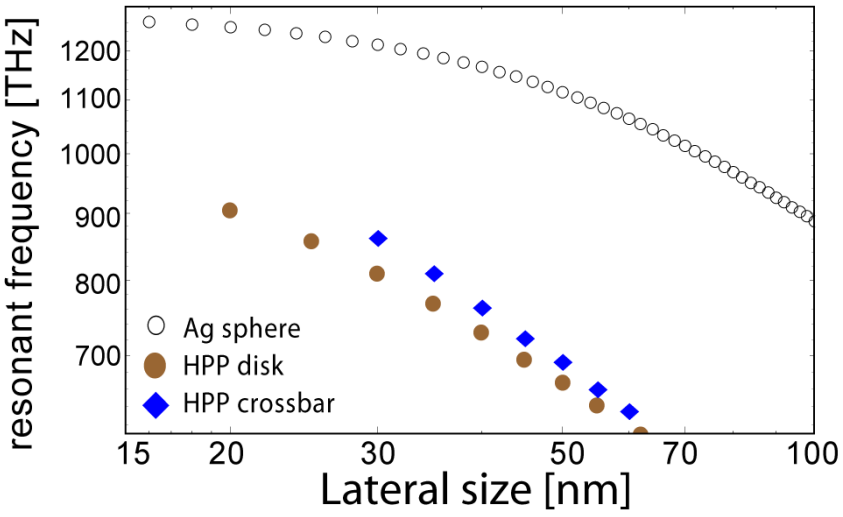

Figure 5.5: Tunability of deep sub-λ resonators. Resonant frequency with respect to lateral dimension L (in nm) of HPP disks (brown circles), HPP crossbars (blue diamond) and Ag nanoparticle.While the resonance of Ag nanosphere asymptotically approach localized surface plasmon resonance, the sub-λ resonator resonance are well separated and red-shifted away from the resonance.

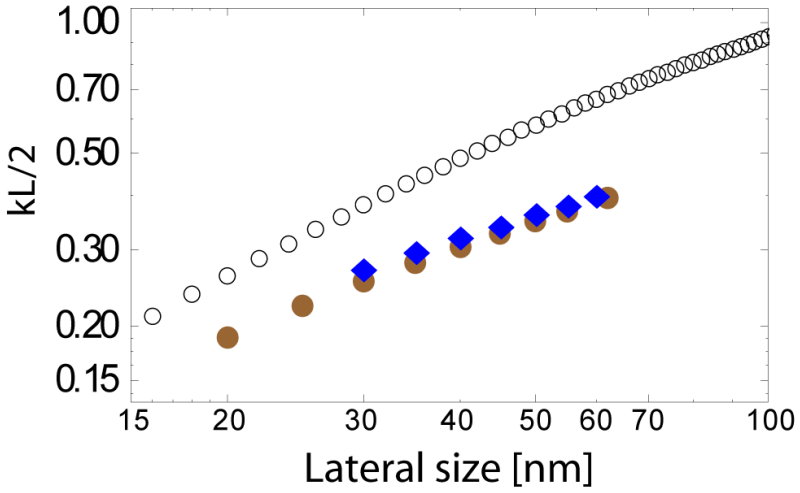

Figure 5.6. The HPP disk and HPP crossbar as electrically small resonators. Physical size L in nm vs. size parameter $kL/2$ of Ag nanospheres (empty circles), HPP disks (solid brown circles) and HPP crossbar resonators (solid blue diamond). The resonant wavelength and the size parameter of the crossbar changes a little from the corresponding disk cavity design. However, the size parameter is smaller than that of nanosphere of the same physical size. This indicates that at a given operation wavelength, the deep sub-wavelength resonators are more compact than an equivalent Ag nanoparticle. The sub-λ resonator are electrically small with size parameter in the range of 0.2-0.4.

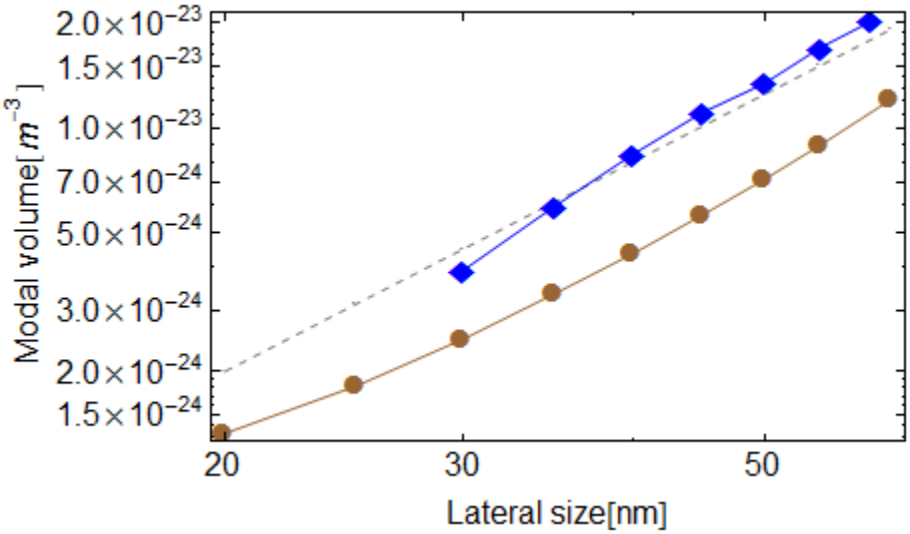

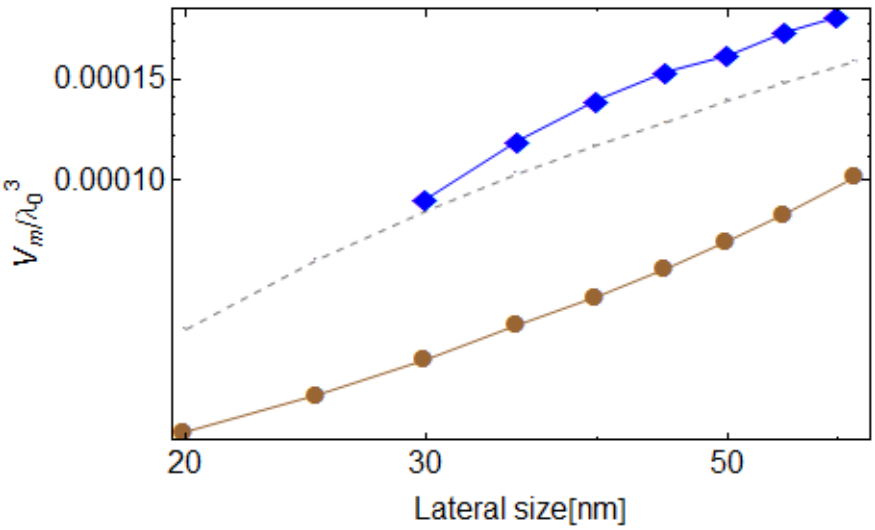

Figure 5.7. Effective mode volume of sub-λ resonators. Thin, dashed line shows the physical volume of the gap region. (a) The mode volume of HPP disks (brown circles) is smaller than the gap volume by about a factor of 1/10. Integrating strip waveguides to form HPP crossbars (blue diamond) raises the mode volume to about as much as the physical volume, as more evanescent coupling spread the fields into the strip region. (b) The effective mode volume of the HPP crossbars is in the range of 0.0001 to 0.0002 cubic wavelength

5.6. Quality factor and radiation behavior of sub-λ resonators

The quality factor Q are extracted from the simulated scattering spectra. The results for HPP disk resonators (brown circles), and HPP crossbars (blue diamond) both of thickness t = 10 nm, and gap g = 5 nm are shown in figure 5.8a, together with results from Ag nanoparticle. In addition, the quality factor of HPP crossbars with thickness t = 15 nm and gap g = 5 nm (yellow), and with thickness t = 7.5 nm and gap g = 2.5 (red) are also included here.

Radiation Q-factor Q_{rad} are likewise obtained for these structures when excluding Ohmic loss of the metal and shown in figure 5.8b. Although a closed cavity made of a deep sub-λ waveguide such as an HPP disk supports ultra-small mode volume which enhances optical interaction, its radiation is rather poor (Q_{rad} significantly higher than that of a simple Ag nanosphere), as a result of impedance mismatch of the HPP mode to free-space. On the other hand, Q is comparable to that of Ag nanoparticle. This means that there is a larger fraction of dissipation that goes into resistive heating in metal in the HPP disk.

HPP crossbars with integrated strip waveguides, however, reveals a dramatic decrease of Q_{rad} to a level comparable to Ag nanoparticles. As the scattered fields show, a significant fraction of radiated power goes into propagating wave along the Ag strip. Table 5.1. shows the ratio of radiated power flux through the cross-section of the Ag-strip waveguide to the total radiated power for HPP crossbar with geometry t = 15 nm, and g = 5 nm. As the overlapping area of the

HPP crossbar shrinks, the fraction of radiation into the waveguide grows to approach 21%. This results confirm that the crossbar design recovers poor free-space radiation that the HPP disk suffers when its lateral dimension shrinks. This benefit is enabled by the virtue of mode area scaling in Ag-strip waveguide. The guided mode along Ag does not cut off as one reduces the width of the strip and increase in propagation loss is low enough to maintain the amount of guided power.

Table 5.1. Fraction of out-coupling into the Ag-strip waveguide for HPP crossbars with geometry t = 15 nm, and g = 5 nm

Lateral size (L)	40 nm	50 nm	60 nm	70 nm	80 nm	90 nm	100 nm
$\beta_{Ag-waveguide}$	0.21	0.21	0.21	0.20	0.16	0.10	0.07

In Figure 5.9, we re-plot Q_{rad} with respect to ka_{Chu}, where a_{Chu} is the smallest radius of the sphere that can enclose the antenna, in order to map these sub-λ resonators to the Chu theoretical limit. It turns out that the Chu factor for the HPP crossbars is advantageous over the HPP disks and appears close to value 1.5 of the Ag nanophere, but still cannot beat it.

Finally, we calculate the radiative efficiency Q/Q_{rad} of these resonators and plot it in figure 5.10. For value less than 0.5, resistive heating dominates dissipation of the mode. The quality factor of HPP crossbars with gap g = 5 nm is still radiation-limited whereas for HPP disks, they are absorption-limited.

5.7. Large Purcell effect in the deep sub-λ resonators.

Purcell factor inside the HPP disk(brown circles) and HPP crossbar (blue diamonds) resonators, estimated from $F_P = \frac{3}{4\pi^2}\left(\frac{\lambda}{n}\right)^3 \frac{Q}{V_{eff}}$ using obtained value of the quality-factor Q and mode volume V_{eff} are shown in Fig 5.10. Even if efficient out-coupling to waveguide in the HPP crossbars lowers the Q, their mode volume V_{eff} remains deep sub-λ on the order of the gap volume. The resulting Purcell enhancement factor is in the range of 1000-5000 for simulated geometries (thickness t = 10 nm and gap = 5 nm).

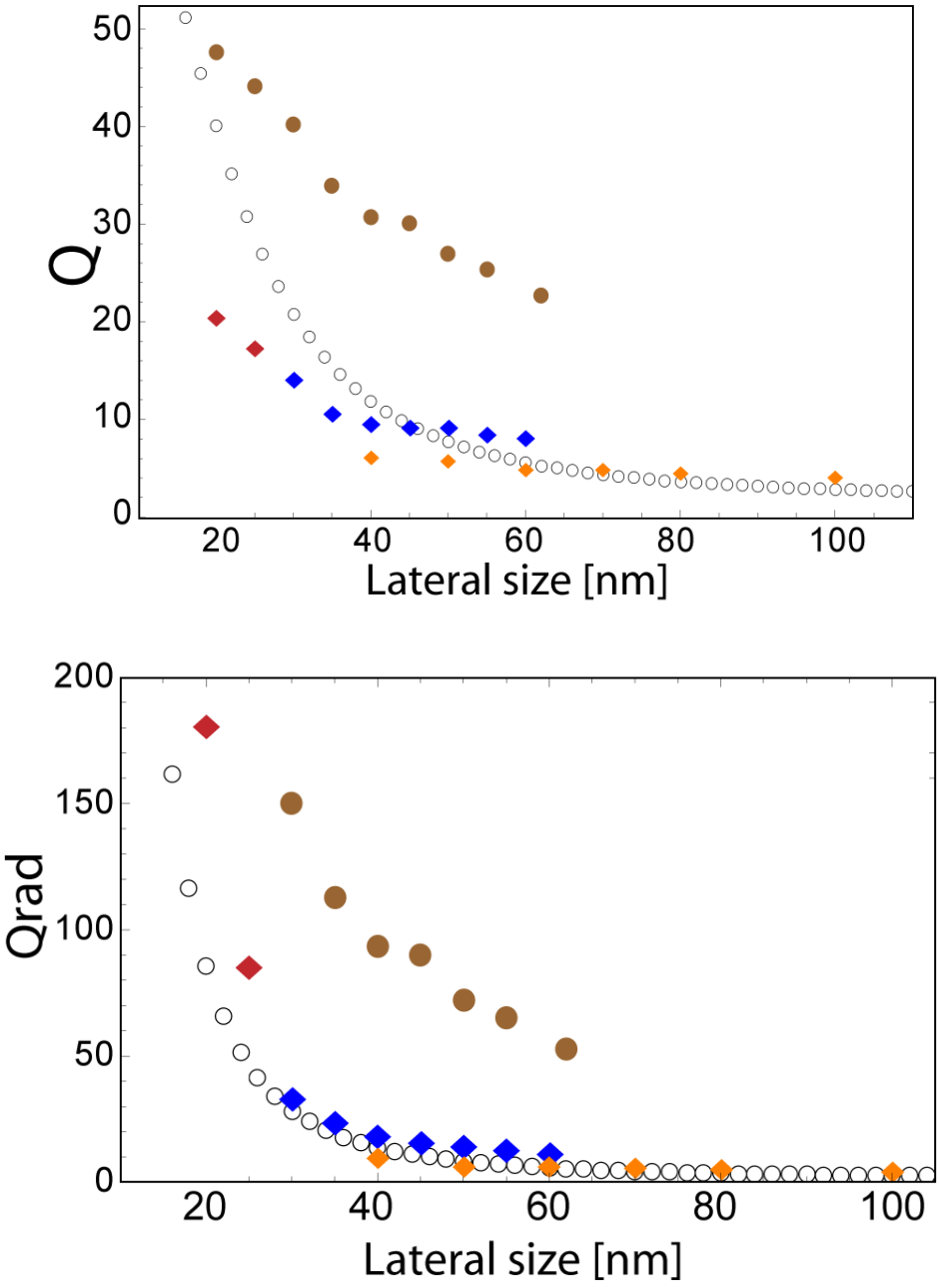

Figure 5.8. Quality factor and Radiation efficiency (a) Total Q-factor Q is obtained from scattering spectra of the fundamental dipole mode, where realistic Ohmic loss of metal is included, are calculated for different structures (Ag nanosphere = empty circles, HPP disk = solid circles, HPP crossbar = solid diamonds). (b). Radiative Q-factor Q_{rad} as obtained from scattering spectra where the metal is assumed lossless. While achieving tiny mode volume, the deep sub-wavelength HPP disk radiates poorly compared to the benchmark Ag nanosphere. However, when extending the materials to strip waveguides as in the HPP crossbar, Q_{rad} drops significantly, showing that radiation is recovered, mainly through out-coupling into the Ag strip waveguide as detailed analysis of the radiation pattern reveals.

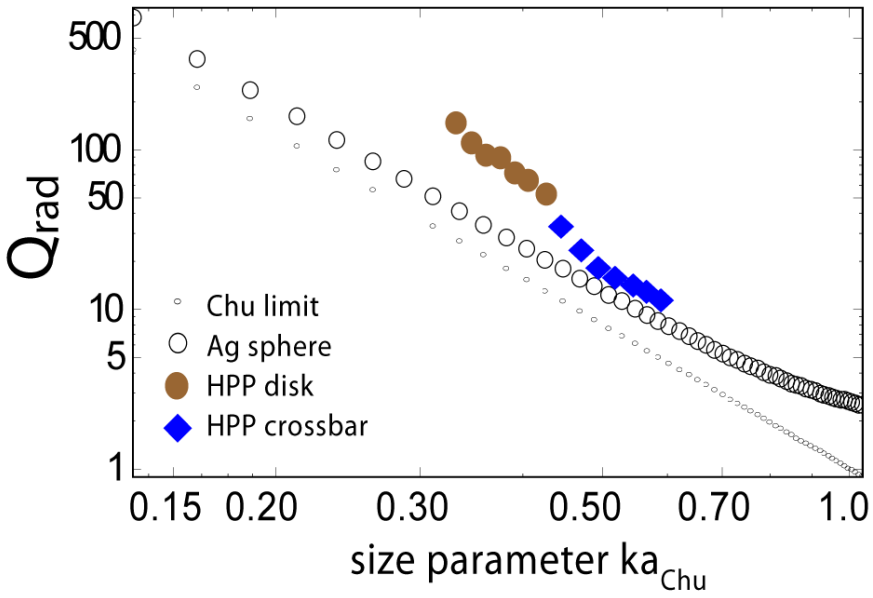

Figure 5.9. Q_{rad} with respect to ka_{Chu}, where a_{Chu} is the smallest radius of the sphere that can enclose the antenna. It turns out that the Chu factor for the HPP crossbars is advantageous over the HPP disks and appears close to value 1.5 of the Ag nanophere, but still cannot beat it. The reason could be that the HPP dipole mode is less spherical in shape and therefore the value of the antenna inductance is sub-optimal unless it were to distribute itself uniformly throughout a sphere of radius a_{Chu} [92–94].

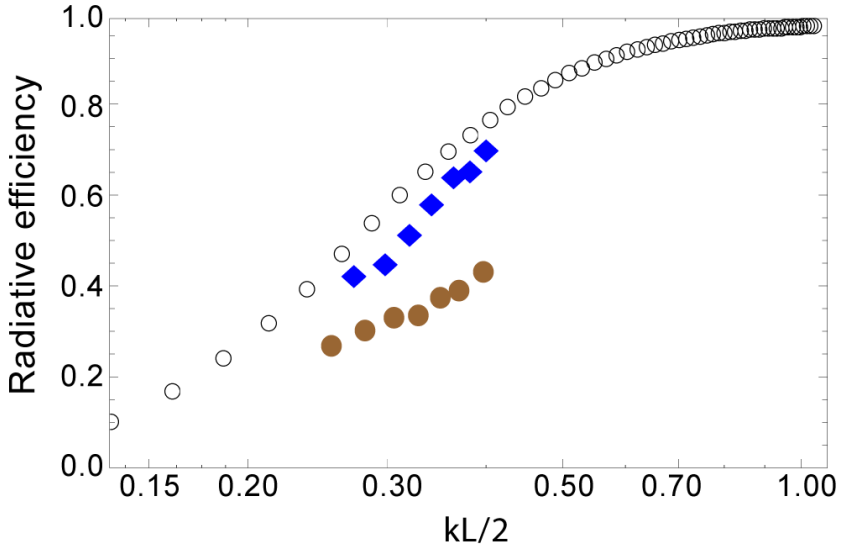

Figure 5.10. Radiative efficiency Q/Q_{rad} of sub-λ resonators. (Ag nanosphere = empty circles, HPP disk = solid circles, HPP crossbar = solid diamonds). For value less than 0.5, resistive heating dominates dissipation of the mode. The quality factor of HPP crossbars with gap g = 5 nm is still radiation-limited whereas for HPP disks, they are absorption-limited.

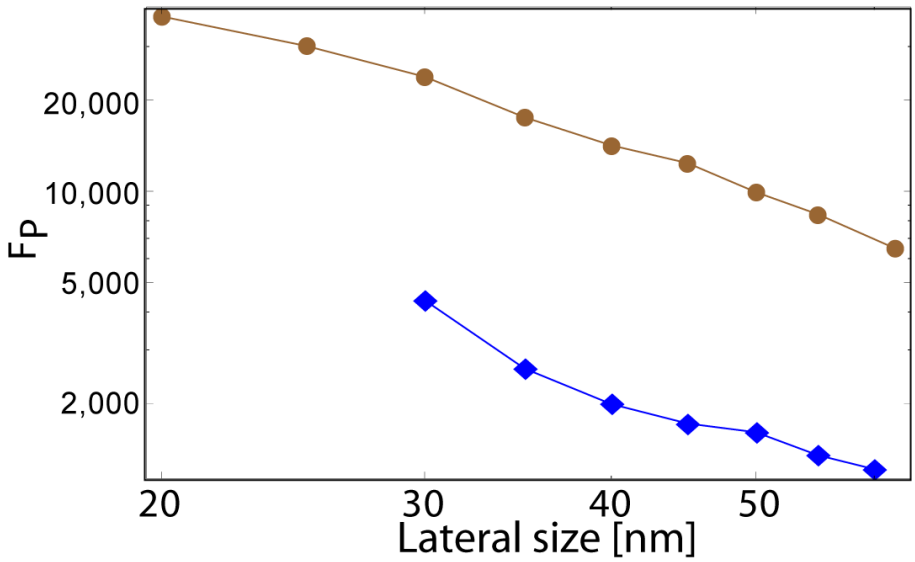

Figure 5.12. Purcell factor inside the HPP disk (brown circles) and HPP crossbar (blue diamonds) resonators, estimated from $F_P = \frac{3}{4\pi^2}\left(\frac{\lambda}{n}\right)^3 \frac{Q}{V_{eff}}$ using simulated value of the quality-factor Q and mode volume V_{eff}, where $n = 1.38$. Efficient out-coupling to waveguide in the HPP crossbars lowers Q but their mode volume V_{eff} remains deep sub-λ even in the presence of evanescent coupling to the Ag-strip and subsequent propagation. The resulting Purcell factor is in the range of 1000-5000 for simulated geometries (thickness t = 10 nm and gap = 5 nm).

5.8. Summary and Outlook

In this chapter, we studied a family of deep sub-λ dipole resonators based on the hybrid plasmon (HPP) mode. Their scattering spectra shows that they are electrically small resonators with resonance that are red-shifted from particle plasmon of comparable size and can be tuned over a much wider range of frequencies. However, for the HPP disks which are closed resonators, coupling to free-space radiation is less efficient than a particle plasmon and hence radiative efficiency drops, as a result of impedance mismatch of the HPP mode to free-space. Improved bandwidth is, nevertheless, recovered in HPP crossbars which are extended resonators by virtue of out-coupling to guided mode in the Ag strip. All these deep sub-λ resonators have ultrasmall mode volume on the order of $1 \times 10^{-4} - 2 \times 10^{-4}$ cubic wavelength and hold promise for three-port devices that can be used to address optical emitters inside the ultra-small cavity region via free-space coupling and via transmission through the cavity along the strip waveguide. Efficiency and speed of the device is aided by Purcell enhancement in the weak-coupling regime and the fact that its scattering cross-section is still considerably larger than its physical size.

Chapter 6
Conclusions and Future Prospects

We started this dissertation by deriving the conditions for an optical 1D and 2D continuum to enhance dipole radiation, namely slow guided wave and sub-wavelength field confinement. We analyzed the way in which an electric dipole emitter near a metal surface can emit rapidly into a surface guided mode (surface plasmon polariton) on a metal surface but this effect occurs strongly only at frequency near the surface plasmon resonance. We focused on the hybrid plasmon (HPP) geometry which non-resonantly enhances dipole radiation by virtue of geometrically tunable confinement in its low permittivity gap region. Hybridization of the dielectric slab mode in the high permittivity slab with the surface plasmon allows such degree of tunable confinement with little compromise in propagation loss. The multimodal nature of dissipation of the dipole emitter in HPP geometry is discussed, including the role of non-radiative quenching due to Ohmic loss of the metal. A related design using high permittivity contrast dielectric (dielectric slot waveguide) are also presented as an alternative.

We extended our theoretical study of Purcell enhancement to numerical simulation of 1D waveguides and more general structures. Using spontaneous emission of dye molecule ensemble as probe of confinement, an experiment on HPP waveguide made of a high index ZnO nanowire on Ag surface shows that almost 75% of molecular emission can be coupled to the deep sub-wavelength guided mode. In addition, the contribution of metal quenching are verified quantitatively using a control measurement which compares consistently with the developed theory and additional fluorescence intensity data. Furthermore, brightness enhancement up to 6-fold implies that good photon extraction efficiency can be achieved due to low propagation loss over at least 5 μm along the length of the waveguide.

To study optical interaction at the single emitter-single photon level, the technical difficulty of overlapping a single emitter to the confined mode poses a tremendous challenge. In addition, the limitation in quenching loss and out-coupling of emitted photons in the hybrid plasmon (HPP) waveguide led us to instead implement an all-dielectric waveguide integrated with mechanical manipulation. Strongly enhanced interaction between a single quantum dot and the squeezed photonic waveguide and its effect on the emission dynamics is observed experimentally with a record high Purcell enhancement factor of 31. Unambiguous measurements on the same quantum dot before and after coupling to the waveguide reveal that enhanced emission dynamics of the quantum dot in the coupled system reduces its fluorescence intermittence and improves its saturation behavior while preserving the purity of its single photon state emission.

In the final part of the dissertation, we switched gears to explore downscaling of dipole resonators based on termination of a two-dimensional HPP guided mode. Simulated scattering spectra shows that they are electrically small resonators with resonance red-shifted from particle

plasmon of comparable size and tunable over a wider range of frequencies. Efficiency and speed of the device is aided by the Purcell enhancement due to their ultrasmall mode volume on the order of $1 \times 10^{-4} - 2 \times 10^{-4}$ cubic wavelength. While dissipation in a HPP disk resonator is absorption-limited and couples poorly to propagating waves due to the large impedance mismatch between the HPP mode and free-space radiation; HPP crossbars, however, can recover the radiative bandwidth by virtue of out-coupling to guided mode in the Ag strip. The HPP crossbar holds promise as a three-port device that can be used to address optical emitters inside its ultra-small cavity region via free-space coupling and via transmission through the cavity along the integrated strip waveguide. Moreover, the ultra-compact footprint of the design holds the prospects of integrating several devices to create a high-density platform on a chip which simultaneously circumvents the propagation loss limitation of plasmonics. The next step in this research direction is to fabricate resonators based on this concept and characterize them experimentally. It is also of our interest to integrate individual emitters inside these resonators to study their optical interaction with the waveguided field and the radiation field.

The strong optical interaction between a single emitter and its single photon emission observed in Chapter 4 has several implications including few-photon nonlinearity[39] and multiple photon scattering[18], [19], [95] which have recently been proposed in the literature and pave the way for quantum information processing applications[20]. One possible research in this direction is to couple a coherent or a single photon source into one end of the waveguide that is loaded with an emitter and study resonance fluorescence and single-photon scattering (or transmission) behavior as a result of interference between the incident field and the emitted field, at the opposite terminal. Another future direction is to incorporate a three-level system emitter which can serves as a qubit driven by a control beam. Photon statistics of an incident beam interacting with multiple emitters along the same waveguide should also exhibit interesting correlations. During the course of our experiment, we coupled two quantum dots to the same waveguide and observed a drastic increase in blinking correlations between the two quantum dots.

It is my hope that this dissertation will contribute to the efforts to further research on emitter interaction with sub-wavelength optical systems. I am looking forward to learning new knowledge about the subject and would be more than thrilled to see the concept being put forth into useful technology in the future.

Berkeley, CA

July 2012

Bibliography

[1] J. A. Schuller, E. S. Barnard, W. Cai, Y. C. Jun, J. S. White, and M. L. Brongersma, "Plasmonics for extreme light concentration and manipulation," *Nature Materials*, vol. 9, no. 3, pp. 193–204, 2010.

[2] H. A. Atwater, "The promise of plasmonics," *Sci. Am.*, vol. 296, no. 4, pp. 56–63, Apr. 2007.

[3] C. A. Balanis, *Antenna Theory: Analysis and Design, 3rd Edition*, 3rd ed. Wiley-Interscience, 2005.

[4] H. A. Haus, *Waves and Fields in Optoelectronics*. Prentice Hall, 1983.

[5] Y. Yamamoto, S. Machida, and G. Björk, "Microcavity semiconductor laser with enhanced spontaneous emission," *Phys. Rev. A*, vol. 44, no. 1, pp. 657–668, Jul. 1991.

[6] Björk, Karlsson, and Yamamoto, "Definition of a laser threshold," *Phys. Rev., A*, vol. 50, no. 2, pp. 1675–1680, Aug. 1994.

[7] M. Khajavikhan, A. Simic, M. Katz, J. H. Lee, B. Slutsky, A. Mizrahi, V. Lomakin, and Y. Fainman, "Thresholdless nanoscale coaxial lasers," *Nature*, vol. 482, no. 7384, pp. 204–207, Feb. 2012.

[8] C. Santori, D. Fattal, J. Vučković, G. S. Solomon, and Y. Yamamoto, "Indistinguishable photons from a single-photon device," *Nature*, vol. 419, no. 6907, pp. 594–597, Oct. 2002.

[9] M. Pelton, C. Santori, J. Vučković, B. Zhang, G. S. Solomon, J. Plant, and Y. Yamamoto, "Efficient Source of Single Photons: A Single Quantum Dot in a Micropost Microcavity," *Phys. Rev. Lett.*, vol. 89, no. 23, p. 233602, Nov. 2002.

[10] G. Lecamp, P. Lalanne, and J. P. Hugonin, "Very Large Spontaneous-Emission β Factors in Photonic-Crystal Waveguides," *Phys. Rev. Lett.*, vol. 99, no. 2, p. 023902, Jul. 2007.

[11] J. N. Anker, W. P. Hall, O. Lyandres, N. C. Shah, J. Zhao, and R. P. V. Duyne, "Biosensing with plasmonic nanosensors," *Nature Materials*, vol. 7, no. 6, pp. 442–453, 2008.

[12] K. Srinivasan, A. Stintz, S. Krishna, and O. Painter, "Photoluminescence measurements of quantum-dot-containing semiconductor microdisk resonators using optical fiber taper waveguides," *Phys. Rev. B*, vol. 72, no. 20, p. 205318, Nov. 2005.

[13] B. Gayral, J. M. Gérard, A. Lemaître, C. Dupuis, L. Manin, and J. L. Pelouard, "High-Q wet-etched GaAs microdisks containing InAs quantum boxes," *Applied Physics Letters*, vol. 75, no. 13, pp. 1908–1910, Sep. 1999.

[14] K. Djordjev, S.-J. Choi, S.-J. Choi, and R. D. Dapkus, "Microdisk tunable resonant filters and switches," *IEEE Photonics Technology Letters*, vol. 14, no. 6, pp. 828 –830, Jun. 2002.

[15] T. Yoshie, A. Scherer, J. Hendrickson, G. Khitrova, H. M. Gibbs, G. Rupper, C. Ell, O. B. Shchekin, and D. G. Deppe, "Vacuum Rabi splitting with a single quantum dot in a photonic crystal nanocavity," *Nature*, vol. 432, no. 7014, pp. 200–203, Nov. 2004.

[16] C. J. M. Smith, H. Benisty, D. Labilloy, U. Oesterle, R. Houdré, T. F. Krauss, R. M. De La Rue, and C. Weisbuch, "Near-infrared microcavities confined by two-dimensional photonic bandgap crystals," *Electronics Letters*, vol. 35, no. 3, p. 228, 1999.

[17] O. Painter, R. K. Lee, A. Scherer, A. Yariv, J. D. O'Brien, P. D. Dapkus, and I. Kim, "Two-Dimensional Photonic Band-Gap Defect Mode Laser," *Science*, vol. 284, no. 5421, pp. 1819–1821, Jun. 1999.

[18] J. T. Shen and S. Fan, "Coherent photon transport from spontaneous emission in one-dimensional waveguides," *Opt. Lett.*, vol. 30, no. 15, pp. 2001–2003, 2005.

[19] J.-T. Shen and S. Fan, "Strongly Correlated Two-Photon Transport in a One-Dimensional Waveguide Coupled to a Two-Level System," *Phys. Rev. Lett.*, vol. 98, no. 15, p. 153003, Apr. 2007.
[20] H. J. Kimble, "The quantum internet," *Nature*, vol. 453, no. 7198, pp. 1023–1030, Jun. 2008.
[21] V. J. Sorger, N. Pholchai, E. Cubukcu, R. F. Oulton, P. Kolchin, C. Borschel, M. Gnauck, C. Ronning, and X. Zhang, "Strongly enhanced molecular fluorescence inside a nanoscale waveguide gap," *Nano Lett.*, vol. 11, no. 11, pp. 4907–4911, Nov. 2011.
[22] Purcell, E. M., "Spontaneous emission probabilities at radio frequencies," *Physical Review*, vol. 69, p. 681, 1946.
[23] P. Michler, A. Kiraz, C. Becher, W. V. Schoenfeld, P. M. Petroff, L. Zhang, E. Hu, and A. Imamoglu, "A Quantum Dot Single-Photon Turnstile Device," *Science*, vol. 290, no. 5500, pp. 2282–2285, Dec. 2000.
[24] J. M. Gérard, B. Sermage, B. Gayral, B. Legrand, E. Costard, and V. Thierry-Mieg, "Enhanced Spontaneous Emission by Quantum Boxes in a Monolithic Optical Microcavity," *Phys. Rev. Lett.*, vol. 81, no. 5, pp. 1110–1113, 1998.
[25] B. Ohnesorge, M. Bayer, A. Forchel, J. Reithmaier, N. Gippius, and S. Tikhodeev, "Enhancement of spontaneous emission rates by three-dimensional photon confinement in Bragg microcavities," *Physical Review B*, vol. 56, no. 8, pp. R4367–R4370, Aug. 1997.
[26] G. S. Solomon, M. Pelton, and Y. Yamamoto, "Single-mode Spontaneous Emission from a Single Quantum Dot in a Three-Dimensional Microcavity," *Phys. Rev. Lett.*, vol. 86, no. 17, pp. 3903–3906, Apr. 2001.
[27] L. A. Graham, D. L. Huffaker, and D. G. Deppe, "Spontaneous lifetime control in a native-oxide-apertured microcavity," *Applied Physics Letters*, vol. 74, no. 17, pp. 2408–2410, Apr. 1999.
[28] M. Schwab, H. Kurtze, T. Auer, T. Berstermann, M. Bayer, J. Wiersig, N. Baer, C. Gies, F. Jahnke, J. P. Reithmaier, A. Forchel, M. Benyoucef, and P. Michler, "Radiative emission dynamics of quantum dots in a single cavity micropillar," *Phys. Rev. B*, vol. 74, no. 4, p. 045323, Jul. 2006.
[29] A. Faraon, D. Englund, D. Bulla, B. Luther-Davies, B. J. Eggleton, N. Stoltz, P. Petroff, and J. Vučković, "Local tuning of photonic crystal cavities using chalcogenide glasses," *Applied Physics Letters*, vol. 92, no. 4, pp. 043123–043123–3, Jan. 2008.
[30] Y. C. Jun, R. D. Kekatpure, J. S. White, and M. L. Brongersma, "Nonresonant enhancement of spontaneous emission in metal-dielectric-metal plasmon waveguide structures," *Phys. Rev. B*, vol. 78, no. 15, p. 153111, Oct. 2008.
[31] I. Gontijo, M. Boroditsky, E. Yablonovitch, S. Keller, U. K. Mishra, and S. P. DenBaars, "Coupling of InGaN quantum-well photoluminescence to silver surface plasmons," *Phys. Rev. B*, vol. 60, no. 16, pp. 11564–11567, Oct. 1999.
[32] Q. Quan, I. Bulu, and M. Lončar, "Broadband waveguide QED system on a chip," *Phys. Rev. A*, vol. 80, no. 1, p. 011810, Jul. 2009.
[33] G. W. Ford and W. H. Weber, "Electromagnetic interactions of molecules with metal surfaces," *Physics Reports*, vol. 113, no. 4, pp. 195–287, Nov. 1984.
[34] R. R. Chance, A. Prock, and R. Silbey, "Molecular Fluorescence and Energy Transfer Near Interfaces," in *Advances in Chemical Physics*, I. Prigogine and S. A. Rice, Eds. John Wiley & Sons, Inc., 2007, pp. 1–65.

[35] D. E. Chang, A. S. Sørensen, P. R. Hemmer, and M. D. Lukin, "Strong coupling of single emitters to surface plasmons," *Phys. Rev. B*, vol. 76, no. 3, p. 035420, Jul. 2007.
[36] T. Lund-Hansen, S. Stobbe, B. Julsgaard, H. Thyrrestrup, T. Sünner, M. Kamp, A. Forchel, and P. Lodahl, "Experimental Realization of Highly Efficient Broadband Coupling of Single Quantum Dots to a Photonic Crystal Waveguide," *Phys. Rev. Lett.*, vol. 101, no. 11, p. 113903, 2008.
[37] T. Baba, "Slow light in photonic crystals," *Nature Photonics*, vol. 2, no. 8, pp. 465–473, 2008.
[38] D. E. Chang, A. S. Sørensen, E. A. Demler, and M. D. Lukin, "A single-photon transistor using nanoscale surface plasmons," *Nature Physics*, vol. 3, no. 11, pp. 807–812, 2007.
[39] P. Kolchin, R. F. Oulton, and X. Zhang, "Nonlinear Quantum Optics in a Waveguide: Distinct Single Photons Strongly Interacting at the Single Atom Level," *Phys. Rev. Lett.*, vol. 106, no. 11, p. 113601, Mar. 2011.
[40] H. Zheng, D. J. Gauthier, and H. U. Baranger, "Cavity-Free Photon Blockade Induced by Many-Body Bound States," *Phys. Rev. Lett.*, vol. 107, no. 22, p. 223601, Nov. 2011.
[41] K. Kojima, H. F. Hofmann, S. Takeuchi, and K. Sasaki, "Nonlinear interaction of two photons with a one-dimensional atom: Spatiotemporal quantum coherence in the emitted field," *Phys. Rev. A*, vol. 68, no. 1, p. 013803, Jul. 2003.
[42] D. Martín-Cano, A. González-Tudela, L. Martín-Moreno, F. J. García-Vidal, C. Tejedor, and E. Moreno, "Dissipation-driven generation of two-qubit entanglement mediated by plasmonic waveguides," *Phys. Rev. B*, vol. 84, no. 23, p. 235306, Dec. 2011.
[43] J. D. Jackson, *Classical Electrodynamics Third Edition*, 3rd ed. Wiley, 1998.
[44] R. Loudon, L. Allen, and D. F. Nelson, "Propagation of electromagnetic energy and momentum through an absorbing dielectric," *Phys. Rev. E*, vol. 55, no. 1, pp. 1071–1085, Jan. 1997.
[45] P. B. Johnson and R. W. Christy, "Optical Constants of the Noble Metals," *Phys. Rev. B*, vol. 6, no. 12, pp. 4370–4379, Dec. 1972.
[46] R. F. Oulton, V. J. Sorger, D. A. Genov, D. F. P. Pile, and X. Zhang, "A hybrid plasmonic waveguide for subwavelength confinement and long-range propagation," *Nature Photonics*, vol. 2, no. 8, pp. 496–500, 2008.
[47] R. F. Oulton, V. J. Sorger, T. Zentgraf, R.-M. Ma, C. Gladden, L. Dai, G. Bartal, and X. Zhang, "Plasmon lasers at deep subwavelength scale," *Nature*, vol. 461, no. 7264, pp. 629–632, Aug. 2009.
[48] V. J. Sorger, Z. Ye, R. F. Oulton, Y. Wang, G. Bartal, X. Yin, and X. Zhang, "Experimental demonstration of low-loss optical waveguiding at deep sub-wavelength scales," *Nature Communications*, vol. 2, p. 331, May 2011.
[49] Y. C. Jun, R. M. Briggs, H. A. Atwater, and M. L. Brongersma, "Broadband enhancement of light emission insilicon slot waveguides," *Opt. Express*, vol. 17, no. 9, pp. 7479–7490, Apr. 2009.
[50] K. J. Vahala, "Optical microcavities," *Nature*, vol. 424, no. 6950, pp. 839–846, Aug. 2003.
[51] A. Kinkhabwala, Z. Yu, S. Fan, Y. Avlasevich, K. Müllen, and W. E. Moerner, "Large single-molecule fluorescence enhancements produced by a bowtie nanoantenna," *Nature Photonics*, vol. 3, no. 11, pp. 654–657, 2009.
[52] P. Anger, P. Bharadwaj, and L. Novotny, "Enhancement and Quenching of Single-Molecule Fluorescence," *Phys. Rev. Lett.*, vol. 96, no. 11, p. 113002, Mar. 2006.

[53] P. Bharadwaj, B. Deutsch, and L. Novotny, "Optical Antennas," *Adv. Opt. Photon.*, vol. 1, no. 3, pp. 438–483, Nov. 2009.
[54] R. F. Oulton, G. Bartal, D. F. P. Pile, and X. Zhang, "Confinement and propagation characteristics of subwavelength plasmonic modes," *New Journal of Physics*, vol. 10, no. 10, p. 105018, Oct. 2008.
[55] C. Borchers, S. Müller, D. Stichtenoth, D. Schwen, and C. Ronning, "Catalyst-nanostructure interaction in the growth of 1-D ZnO nanostructures," *J Phys Chem B*, vol. 110, no. 4, pp. 1656–1660, Feb. 2006.
[56] G. Zoriniants and W. L. Barnes, "Fluorescence enhancement through modified dye molecule absorption associated with the localized surface plasmon resonances of metallic dimers," *New Journal of Physics*, vol. 10, no. 10, p. 105002, Oct. 2008.
[57] Y. Fedutik, V. V. Temnov, O. Schöps, U. Woggon, and M. V. Artemyev, "Exciton-Plasmon-Photon Conversion in Plasmonic Nanostructures," *Phys. Rev. Lett.*, vol. 99, no. 13, p. 136802, 2007.
[58] T. J. Kippenberg, A. L. Tchebotareva, J. Kalkman, A. Polman, and K. J. Vahala, "Purcell-Factor-Enhanced Scattering from Si Nanocrystals in an Optical Microcavity," *Phys. Rev. Lett.*, vol. 103, no. 2, p. 027406, Jul. 2009.
[59] J. T. Robinson, C. Manolatou, L. Chen, and M. Lipson, "Ultrasmall mode volumes in dielectric optical microcavities," *Phys. Rev. Lett.*, vol. 95, no. 14, p. 143901, Sep. 2005.
[60] V. R. Almeida, Q. Xu, C. A. Barrios, and M. Lipson, "Guiding and confining light in void nanostructure," *Opt. Lett.*, vol. 29, no. 11, pp. 1209–1211, Jun. 2004.
[61] C. Creatore, L. C. Andreani, M. Miritello, R. Lo Savio, and F. Priolo, "Modification of erbium radiative lifetime in planar silicon slot waveguides," *Applied Physics Letters*, vol. 94, no. 10, pp. 103112–103112–3, Mar. 2009.
[62] A. H. J. Yang, S. D. Moore, B. S. Schmidt, M. Klug, M. Lipson, and D. Erickson, "Optical manipulation of nanoparticles and biomolecules in sub-wavelength slot waveguides," *Nature*, vol. 457, no. 7225, pp. 71–75, Jan. 2009.
[63] C. Koos, P. Vorreau, T. Vallaitis, P. Dumon, W. Bogaerts, R. Baets, B. Esembeson, I. Biaggio, T. Michinobu, F. Diederich, W. Freude, and J. Leuthold, "All-optical high-speed signal processing with silicon-organic hybrid slot waveguides," *Nature Photonics*, vol. 3, pp. 216–219, Apr. 2009.
[64] A. J. Shields, "Semiconductor quantum light sources," *Nature Photonics*, vol. 1, no. 4, pp. 215–223, 2007.
[65] A. V. Akimov, A. Mukherjee, C. L. Yu, D. E. Chang, A. S. Zibrov, P. R. Hemmer, H. Park, and M. D. Lukin, "Generation of single optical plasmons in metallic nanowires coupled to quantum dots," *Nature*, vol. 450, no. 7168, pp. 402–406, Nov. 2007.
[66] R. Kolesov, B. Grotz, G. Balasubramanian, R. J. Stöhr, A. A. L. Nicolet, P. R. Hemmer, F. Jelezko, and J. Wrachtrup, "Wave–particle duality of single surface plasmon polaritons," *Nature Physics*, vol. 5, no. 7, pp. 470–474, 2009.
[67] A. Huck, S. Kumar, A. Shakoor, and U. L. Andersen, "Controlled Coupling of a Single Nitrogen-Vacancy Center to a Silver Nanowire," *Phys. Rev. Lett.*, vol. 106, no. 9, p. 096801, Feb. 2011.
[68] J. Claudon, J. Bleuse, N. S. Malik, M. Bazin, P. Jaffrennou, N. Gregersen, C. Sauvan, P. Lalanne, and J.-M. Gérard, "A highly efficient single-photon source based on a quantum dot in a photonic nanowire," *Nature Photonics*, vol. 4, no. 3, pp. 174–177, 2010.

[69] K. G. Lee, X. W. Chen, H. Eghlidi, P. Kukura, R. Lettow, A. Renn, V. Sandoghdar, and S. Götzinger, "A planar dielectric antenna for directional single-photon emission and near-unity collection efficiency," *Nature Photonics*, vol. 5, no. 3, pp. 166–169, 2011.

[70] V. S. C. M. Rao and S. Hughes, "Single Quantum Dot Spontaneous Emission in a Finite-Size Photonic Crystal Waveguide: Proposal for an Efficient 'On Chip' Single Photon Gun," *Phys. Rev. Lett.*, vol. 99, no. 19, p. 193901, Nov. 2007.

[71] T. M. Babinec, B. J. M. Hausmann, M. Khan, Y. Zhang, J. R. Maze, P. R. Hemmer, and M. Lončar, "A diamond nanowire single-photon source," *Nature Nanotechnology*, vol. 5, no. 3, pp. 195–199, 2010.

[72] J. Bleuse, J. Claudon, M. Creasey, N. S. Malik, J.-M. Gérard, I. Maksymov, J.-P. Hugonin, and P. Lalanne, "Inhibition, Enhancement, and Control of Spontaneous Emission in Photonic Nanowires," *Phys. Rev. Lett.*, vol. 106, no. 10, p. 103601, Mar. 2011.

[73] S. A. Empedocles, R. Neuhauser, and M. G. Bawendi, "Three-dimensional orientation measurements of symmetric single chromophores using polarization microscopy," *Nature*, vol. 399, pp. 126–130, May 1999.

[74] B. Lounis, H. A. Bechtel, D. Gerion, P. Alivisatos, and W. E. Moerner, "Photon antibunching in single CdSe/ZnS quantum dot fluorescence," *Chemical Physics Letters*, vol. 329, no. 5–6, pp. 399–404, Oct. 2000.

[75] X. Wu, Y. Sun, and M. Pelton, "Recombination rates for single colloidal quantum dots near a smooth metal film," *Physical Chemistry Chemical Physics*, vol. 11, no. 28, p. 5867, 2009.

[76] K. T. Shimizu, W. K. Woo, B. R. Fisher, H. J. Eisler, and M. G. Bawendi, "Surface-Enhanced Emission from Single Semiconductor Nanocrystals," *Phys. Rev. Lett.*, vol. 89, no. 11, p. 117401, 2002.

[77] S. Schietinger, M. Barth, T. Aichele, and O. Benson, "Plasmon-Enhanced Single Photon Emission from a Nanoassembled Metal−Diamond Hybrid Structure at Room Temperature," *Nano Lett.*, vol. 9, no. 4, pp. 1694–1698, 2009.

[78] S. Kühn, U. Håkanson, L. Rogobete, and V. Sandoghdar, "Enhancement of Single-Molecule Fluorescence Using a Gold Nanoparticle as an Optical Nanoantenna," *Phys. Rev. Lett.*, vol. 97, no. 1, p. 017402, Jul. 2006.

[79] P. Frantsuzov, M. Kuno, B. Jankó, and R. A. Marcus, "Universal emission intermittency in quantum dots, nanorods and nanowires," *Nature Physics*, vol. 4, no. 7, pp. 519–522, 2008.

[80] X. Ma, H. Tan, T. Kipp, and A. Mews, "Fluorescence Enhancement, Blinking Suppression, and Gray States of Individual Semiconductor Nanocrystals Close to Gold Nanoparticles," *Nano Lett.*, vol. 10, no. 10, pp. 4166–4174, 2010.

[81] R.-M. Ma, R. F. Oulton, V. J. Sorger, G. Bartal, and X. Zhang, "Room-temperature sub-diffraction-limited plasmon laser by total internal reflection," *Nature Materials*, vol. 10, no. 2, pp. 110–113, 2011.

[82] M. Meier and A. Wokaun, "Enhanced fields on large metal particles: dynamic depolarization," *Opt. Lett.*, vol. 8, no. 11, pp. 581–583, Nov. 1983.

[83] H. Kuwata, H. Tamaru, K. Esumi, and K. Miyano, "Resonant light scattering from metal nanoparticles: Practical analysis beyond Rayleigh approximation," *Applied Physics Letters*, vol. 83, no. 22, pp. 4625–4627, Dec. 2003.

[84] L. J. Chu, "Physical Limitations of Omni-Directional Antennas," *Journal of Applied Physics*, vol. 19, no. 12, pp. 1163–1175, Dec. 1948.

[85] J. S. McLean, “A re-examination of the fundamental limits on the radiation Q of electrically small antennas,” *IEEE Transactions on Antennas and Propagation*, vol. 44, no. 5, p. 672, May 1996.
[86] G. Sun and J. B. Khurgin, “Comparative study of field enhancement between isolated and coupled metal nanoparticles: An analytical approach,” *Applied Physics Letters*, vol. 97, no. 26, pp. 263110–263110–3, Dec. 2010.
[87] C. Manolatou and F. Rana, “Subwavelength Nanopatch Cavities for Semiconductor Plasmon Lasers,” *IEEE Journal of Quantum Electronics*, vol. 44, no. 5, pp. 435 –447, May 2008.
[88] K. Yu, A. Lakhani, and M. C. Wu, “Subwavelength metal-optic semiconductor nanopatch lasers,” *Opt. Express*, vol. 18, no. 9, pp. 8790–8799, Apr. 2010.
[89] S. A. Maier, “Plasmonic field enhancement and SERS in the effective mode volume picture,” *Opt. Express*, vol. 14, no. 5, pp. 1957–1964, Mar. 2006.
[90] A. Chandran, E. Barnard, J. White, and M. Brongersma, “Metal-dielectric-metal surface plasmon-polariton resonators,” *Physical Review B*, vol. 85, no. 8, Feb. 2012.
[91] T. H. Taminiau, F. D. Stefani, and N. F. van Hulst, “Optical Nanorod Antennas Modeled as Cavities for Dipolar Emitters: Evolution of Sub- and Super-Radiant Modes,” *Nano Letters*, vol. 11, no. 3, pp. 1020–1024, Mar. 2011.
[92] N. Engheta, A. Salandrino, and A. Alù, “Circuit Elements at Optical Frequencies: Nanoinductors, Nanocapacitors, and Nanoresistors,” *Phys. Rev. Lett.*, vol. 95, no. 9, p. 095504, 2005.
[93] H. A. Wheeler, “The Spherical Coil as an Inductor, Shield, or Antenna,” *Proceedings of the IRE*, vol. 46, no. 9, pp. 1595 –1602, Sep. 1958.
[94] H. A. Wheeler, “The Radiansphere around a Small Antenna,” *Proceedings of the IRE*, vol. 47, no. 8, pp. 1325 –1331, Aug. 1959.
[95] Ş. E. Kocabaş, E. Rephaeli, and S. Fan, “Resonance fluorescence in a waveguide geometry,” *Phys. Rev. A*, vol. 85, no. 2, p. 023817, Feb. 2012.

Appendix A

General recursive formula for the reflectivity of a stacked multilayer by transmission line method

From transmission line theory, we may consider each dielectric layer as a transmission line which is characterized by its characteristic impedance η and reflection coefficient r to obtain the overall reflection response $\Gamma_1 = \frac{E_{1-}}{E_{1+}}$ and overall impedance response Z_1 recursively.

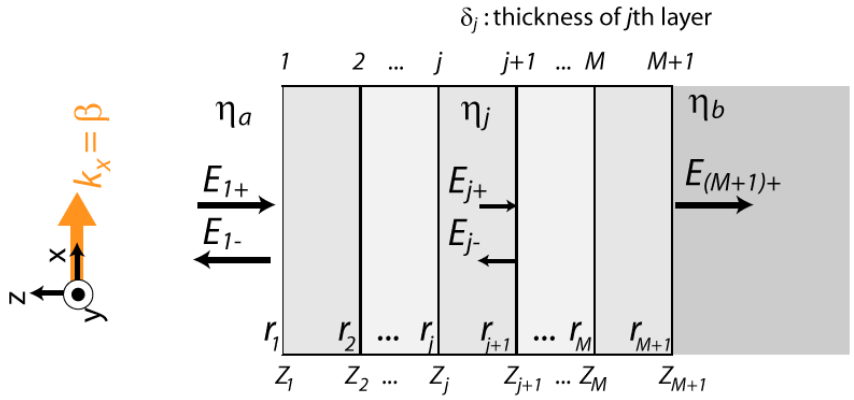

Propagation in each medium and the matching condition interface gives rise to a recursion formula for Z and Γ

a) Propagation condition in jth layer

$$Z_j = \eta_j \left(\frac{Z_{j+1} - i\,\eta_j \tan\delta_j}{\eta_j - i\,Z_{j+1} \tan\delta_j} \right)$$

$$\Gamma_j = \Gamma_{j+1} e^{2i\delta_j}$$

The phase-shift $\delta_j = \beta_j l_j$ is due to propagation across layer j of thickness l_j where η is characteristic impedance and $\beta_j = k_{z,j} = q_j k$ is propagation constant of each transmission line (or across dielectric layer j).

b) The matching conditions at an interface. Primed denotes the right domain whereas unprimed, left domain.

$$Z = Z'$$

$$\Gamma = \frac{r + \Gamma'}{1 + r\,\Gamma'}$$

The elementary reflection coefficients r_j from the left of each interface are defined in terms of characteristic impedances across this interface according to the Fresnel formula

$$r_j = \frac{\eta_j - \eta_{j-1}}{\eta_j + \eta_{j-1}}$$

where $\eta_j = \frac{q_j}{\varepsilon_j}$ for TM-wave and $\eta_j = \frac{1}{q_j} = \frac{k}{k_{z,j}}$ for TE wave are impedance of each layer depending on polarization and angle from normal.

Combining these matching conditions, we obtain the recursion formula for the reflection response

$$\Gamma_{\mathrm{j}} = \frac{r_j + \Gamma_{\mathrm{j+1}} e^{2i\delta_j}}{1 + r_j \Gamma_{\mathrm{j+1}} e^{2i\delta_j}}, \text{ initialized by } \Gamma_{\mathrm{M+1}} = r_{M+1}$$

The final reflection response of a stacked multilayer Γ_1 can then be evaluated and plugged in r_t and r_b in the expression for Purcell effect calculation in section 2.2.

Appendix B

Preparation of Silicon nanowires

The Si nanowires used in the experiment were grown following the procedure in Ref [38], by the vapor-liquid-solid method on a (111) oriented silicon wafer with a resistivity of 0.010-0.02 ohm-cm. The wafer was cleaned using the conventional RCA process (a recipe developed by the RCA company), followed by native oxide removal with a 6:1 buffered oxide etchant (from J.T. Baker) for 15 seconds and rinsing in deionized water. Within 3 minutes, the wafer was loaded into an electron beam evaporator chamber. The chamber was pumped down to 1×10^{-6} Torr. First, a 30 Å gold film was deposited by electron beam evaporation, followed by synthesis of silicon nanowires in a cold wall infrared lamp-heated chemical vapor deposition chamber (Easy tube 3000^{TM}) at a temperature of 680°C. 15 sccm (standard cubic centimeter) of SiH_4 and 400 sccm of H_2 were provided as a silicon gas source and a carrier gas, respectively.Pure HCl gas of 10 sccm was also incorporated, which improves the uniformity of nanowire diameter and prevents diffusion of gold tips from the top of the nanowires. The chamber pressure was maintained at 7 Torr using a mechanical rotary pump. The growth rate of the nanowire under these conditions was about 5 μm/hr and average diameter of NWs was about 270 nm. In order to remove gold tips and gold particles, silicon nanowires were soaked in a commercial gold etchant (TFA) for 5 minutes, and then rinsed with deionized water.